Self-assembly of anisotropic DNA-based patchy particles

Inaugural dissertation

for the attainment of the title of the doctor
in the Faculty of Mathematics and Natural Sciences
at the Heinrich Heine University Düsseldorf

presented by

Sanja Novak
from Ljubljana, Slovenia

Düsseldorf, 2019

from the Institute of Complex Systems, Soft condensed matter (ICS-3)
Forschungszentrum Jülich

Published by permission of the
Faculty of Mathematics and Natural Sciences at
at Heinrich Heine University Düsseldorf

Supervisor: Prof. Dr. Jan K. G. Dhont

Date of the oral examination: 17.07.2019

Declaration of Authorship

I, Sanja Novak , declare under oath that I have produced my thesis independently and without any undue assistance by third parties under consideration of the "Principles for the Safeguarding of Good Scientific Practice at Heinrich Heine University Düsseldorf".

I confirm that:

- This work was done wholly or mainly while in candidature for a research degree at this University.
- Where I have consulted the published work of others, this is always clearly attributed.
- Where I have quoted from the work of others, the source is always given. With the exception of such quotations, this thesis is entirely my own work.
- I have acknowledged all main sources of help.
- Where the thesis is based on work done by myself jointly with others, I have made clear exactly what was done by others and what I have contributed myself.

Signed:

_____

"Regrets, I've had a few
But then again, too few to mention
I did what I had to do
And saw it through without exemption
...
Yes, there were times, I'm sure you knew
When I bit off more than I could chew
But through it all, when there was doubt
I ate it up and spit it out
I faced it all and I stood tall
And did it my way
...
For what is man, what has he got?
If not himself, then he has naught
To say the things he truly feels
And not the words of one who kneels
The record shows I took the blows
And did it my way"

Frank Sinatra, My way

Abstract

Self-assembly of anisotropic DNA-based patchy particles

Patchy colloids constitute a new class of materials in the area of soft matter. They contain discrete interaction sites called patches at specific locations on the particle surface which ensure directionality in the interactions of the particle with its surrounding. Therefore, these new materials hold great promise to provide novel programmed approaches of self-assembly for colloidal particles. This is possible by controlling the position, number and physicochemical properties of the patches. Adding shape anisotropy to patchy particles can substantially enrich the phase behavior of these colloidal systems. Due to synthetic challenges, the self-assembly of anisotropic patchy particles is less explored in comparison to spherical ones.

The work presented in this thesis focuses on systematic investigation of the phase behavior of anisotropic DNA-based patchy particles. Using DNA as a molecular tool, different DNA-based patchy constructs with engineered shape and interaction potentials are fabricated. Gapped all-DNA duplexes, all-DNA rod-like patchy particles and DNA-polymer hybrid soft-patchy particles are presented. Their self-assembly behavior is the core of the thesis. Experimental methods, small-angle X-ray scattering and polarizing optical microscopy, are complemented by computer simulation results in order to obtain a comprehensive understanding of the self-assembly pathways of the mentioned systems. All of the above systems exhibit rich self-assembly behavior resulting with the formation of complex phases, including novel lyotropic liquid crystal and cubic network phases. Moreover, the experimental realization of a new self-assembly concept is introduced based on programmable decoration of DNA backbone with temperature-responsive polymeric patches. The results presented reveal that DNA-based patchy constructs can serve as model systems to explore a wide range of physical phenomena in soft matter.

Zusammenfassung

Selbstorganization von anisotropen DNS-basierten patchy Teilchen

Patchy kolloidale Teilchen bilden eine neue Klasse von Materialien auf dem Gebiet der Weichen Materie. Die Teilchen haben diskrete Wechselwirkungsstellen an spezifischen Oberflächenpunkten (sog. Patches), welche eine orientierungsabhängige Wechselwirkung mit ihrer Umgebung ermöglichen. Diese neuen Materialien sind daher vielversprechend für neue programmierte Methoden zur Selbstorganisation kolloidaler Teilchen. Dies ist ermöglicht durch die kontrollierte Auswahl der Zahl, Positionen und physikochemischen Eigenschaften von Wechselwirkungsstellen. Zusätzliche Formanisotropie der patchy Teilchen kann zu einer signifikanten Anreicherung an möglichen Phasen dieser kolloidalen Systeme führen. Die Selbstorganisation von anisotropen patchy Kolloiden ist aufgrund erhöhter Herausforderungen in der Synthese weniger erforscht als die Selbstorganisation isotroper Teilchen.

Die in der Promotionsarbeit dargestellte Forschungsarbeit beinhaltet systematische Untersuchungen des Phasenverhaltens von anisotropen, DNS-basierten patchy Teilchen. Unter Verwendung von DNS als molekularem Werkzeug werden DNS-basierte patchy Konstrukte mit maßgeschneiderten Formen und Wechselwirkungspotentialen hergestellt. Syntheseergebnisse für Duplexe mit Lücke und stäbchenförmigen patchy Teilchen aufgebaut aus reiner DNS sowie für weiche patchy DNS-Polymer Hybridteilchen werden präsentiert. Das Verhalten dieser Konstrukte bei Selbstorganisation bildet das Herzstück dieser Arbeit. Diverse experimentelle Methoden einschließlich Kleinwinkelröntgenstreuung und optischer Polarisationsmikroskopie werden ergänzt durch Computersimulationsergebnisse um zu einem umfassenden Verständnis der Selbstorganisationswege der untersuchten Systeme zu gelangen. Die Systeme weisen alle ein vielfältiges Verhalten bei der Selbstorganisation auf, mit Ausbildung komplexer Phasen einschließlich neuartiger lyotroper Flüssigkristalle und kubischer Netzwerkphasen. Weiterhin wird die experimentelle Realisierung eines neuen Konzepts der Selbstorganisation vorgestellt, basierend auf der maßgeschneiderten Dekoration des DNS Gerüsts mit auf thermische Veränderungen reagierenden Polymer Patches. Die in der Arbeit dargestellten Ergebnisse zeigen, dass auf DNS basierende patchy Konstrukte als Modellsysteme dienen können für die Erforschung eines breiten Spektrums an physikalischen Phänomenen auf dem Gebiet der Weichen Materie.

Acknowledgements

No man is an island. And no thesis can be successfully completed without help, support and occasional long runs after working hours. Here are few words to acknowledge all the wonderful people who happen to be my coworkers, collaborators, friends and family, some of them taking several roles at once.

First things first, I thank Manolis for being my scientific advisor. Working with you was an adventure! Now coming to the end of it, I must thank you for carefully watching my steps on this journey, and helping me to understand the world around me.

I am also very grateful to prof. Jan Dhont, who made it possible for me to take on this challenge and provided support along the way, whenever needed.

To prof. Cristiano de Michele and prof. Gerhard Gompper, whose simulation results beautifully complemented my experimental findings, and allowed to expand the horizons.

There were people who offered their expertise, advice and selflessly spent their time to make all the measurements happen. Special thanks to Emmanuel Kentzinger for always giving a hand during measurements on GALAXI.

I would like to thank prof. Gerhard Naegele for his help with the German translation of abstract for this thesis.

Whole group for being a warm and supportive environment, always open for discussion and ready to help.

I must especially thank my dear office mates who were bringing sunshine to cloudy days: Oli for long conversations, Mehrnaz for all the support (and patience) in the final phase, and Katarina for being a great collaborator, excellent friend and outstanding teacher for life.

Then there were my friends, scattered all over the world but still staying close in hearts: I thank Ivany for running races with me, Monika for coffee breaks in our office, Darko for sharing *Wings for life* experience and simply being Darko, Paola who inspires me for years already with her boldness, Perina for asking how things are going and then asking again because I would simply forget to hit that reply, Sebastian for being a friend in misery and joy, and Natali for listening, understanding and exchanging experiences from our PhD lives. I am grateful also to everyone I share nice memories with. This paragraph would be several pages long to name you all, but I am sure you know who you are!

Dragana i Goga, who were both family and friends to me. Thank you for being my (almost) sisters!

To my dear parents who patiently waited on my call each day, celebrated with me each small success and still made me feel carefree on times. *Hvala mami i tati za ljubav i podršku, svakodnevne razgovore i najukusnije zajedničke ručkove!*

Finally, there is Albert who supports me through thick and thin. Words cannot describe the meaning you have in my life! Thank you for being tech and moral support, and for all memories we've created together. *Dziękuję, że jesteś!*

...

Contents

List of Figures

List of Abbreviations

A	Adenine
bp	Base pair
BD	Brownian dynamics
C	Cytosine
Col	Columnar
D-block	DNA block
DMF	N, N- Dimethylformamide
DNA	Deoxyribonucleic acid
G-DNA	Gapped DNA
G	Guanine
GALAXI	**G**allium **A**node **L**ow-**A**ngle **X**-ray **I**nstrument
H-DNA	Hairpin DNA
HPC	Hexagonally packed cylinders
I	Isotropic
L-DNA	Linear-shaped DNA-polymer
LC	Liquid crystal
MC	Monte Carlo
MWCO	Molecular weight cut-off
N*	Cholesteric
N_{cyb}	Cybotactic nematic
NMR	Nuclear magnetic resonance
OBDD	Ordered bicontinuous double diamond
OBDG	Ordered bicontinuous double gyroid
P-block	Polymeric block
Π-DNA	Π-shaped DNA-polymer
POM	Polarization optical microscopy
SAXS	Small-angle X-ray scattering
Sm	Smectic
Sm-A	Smectic A
Sm-B	Smectic B
Sm-fA	Folded smectic A
T	Thymine

To my mama, tata and Albert...

Chapter 1

Introduction

Polymers, surfactants, colloids, and liquid crystals, also known as soft materials, are ubiquitous in a wide range of everyday applications. They belong to a class of materials called soft matter and are commonly used in technological applications in various industrial branches as detergents, food additives or in cosmetics. The term "soft matter" was introduced in 1970s by Nobel laureate Pierre-Gilles de Gennes. These materials are often described as "squishy" and soft to the touch. Although this is true to some extent, the "softness" should be understood in a broader context. The behavior of these systems is governed by their mesoscopic dimensions and interactions in the range of thermal energy. Therefore, soft materials are easily deformable and have the propensity to respond to external fields.

Self-assembly is one of the key concepts in soft matter. It is the process in which simple components of a disordered system spontaneously form more complex organized structures without external intervention. The assembly is driven by non-covalent interactions among the components. Numerous self-assembly processes take place in nature, often in a hierarchical fashion. Various self-assembled structures exist in living organisms, such as proteins, viruses, blood cells, and DNA. For example, self-assembly of single DNA strands into double-stranded helical structure is a base for genes encoding, and therefore, one of the crucial processes for life on Earth.

Recently, DNA self-assembly has been employed outside of the biological context. The potential of DNA for programmable self-assembly has been used since 1980s when Nadrian Seeman set the foundation for the field of structural DNA nanotechnology. Seeman introduced a revolutionary idea to exploit a nucleic acid material as a nanoscale building material. This is possible by exploiting the chemical complementarity in DNA as a basic tool for the fabrication of complex functional nanostructures made solely from DNA. By carefully designing the sequence of oligonucleotides, a wide range of multidimensional complex DNA architectures can be achieved with a potential for various applications.

The work presented in this thesis focuses on exploring unconventional bulk phase behavior of diverse states of soft matter. Using DNA as a molecular tool, different DNA-based constructs with engineered shape and interaction potentials are fabricated. Their self-assembly behavior is the core of this thesis. The results reveal that DNA-based nanostructures can serve as model systems for exploring a wide range of physical phenomena in soft matter.

The chapters in this thesis are organized in a following way:

- In **Chapter 2**, a literature overview of few self-assembly concepts in soft matter that are related to the topic of the thesis is given. In addition, a general introduction to DNA structure and existing work on DNA liquid crystal self-assembly is presented.
- In **Chapter 3**, an overview of experimental techniques with a brief description of their basic principles, together with the details related to the synthesis of the DNA constructs is presented.
- In **Chapter 4**, so-called gapped all-DNA duplexes are presented. This system is fabricated by exploiting the difference in persistence length between single-stranded and double-stranded DNA.
- In **Chapter 5**, all-DNA rod-like patchy particles with controlled valence are introduced. This type of particles is made by selectively screening the attraction at the blunt ends of linear DNA helices.
- In **Chapter 6** DNA-based anisotropic soft patchy particles are presented. In this type of patchy particles, temperature-responsive polymeric patchy units are used.
- In **Chapter 7**, a summary of the main conclusions and future perspective are briefly presented.

Chapter 2

DNA and soft matter self-assembly

A literature overview of important concepts related to the topic of the thesis is presented briefly in this chapter. The work presented in this thesis is inspired by four well-established self-assembly concepts in the area of soft matter: DNA self-assembly, liquid crystal self-assembly, self-assembly mediated by patchy interactions and block copolymers self-assembly. General introduction to DNA structure and self-assembly behavior is given in the beginning of the chapter.

2.1 DNA

In the story of our lives, DNA (deoxyribonucleic acid) can be understood as a language the story is written in. DNA carries genes, which means that it shapes who we are and what we do; it dictates the color of our hair and eyes, our blood type, risk for specific diseases... However, the genetic function is performed by a small fraction of the DNA in our bodies. Only about 1% of human DNA carries the genetic code, while it is still unknown what is the task of the rest. Within eukaryotic cell, DNA is organized in the form of chromosomes. Most of the eukaryotic DNA is stored in nucleus, and a small part is also found in organelles such as mitochondria and chloroplasts, while prokaryotes store their DNA in cytoplasm. During a cell division, chromosomes are duplicated so that each cell gets a complete set of chromosomes.

Looking at it from a different perspective, DNA is in fact nothing else but a charged biopolymer made of nucleotides. Its double-helical structure consists of two strands, called polynucleotides, coiled around one another. One of the most basic characteristics of maromolecules is the flexibility of a polymer chain. Unlike the common synthetic polymers, DNA can behave both as stiff rod or a flexible coil, due to its charged character and helical structure. A measure for the stiffness of a polymer is persistence length, L_p. It can be extracted from the directional correlation function of two macromolecular segments which diminishes exponentially with the growth of the chain length separating them [1]. Generally speaking, below this value a polymer can be considered stiff. For a double helix $L_p \sim 50$ nm, which corresponds to 150 bp or more, depending on temperature, ionic strength, and pH [2, 3]. For a single-stranded DNA L_p was found to be in range between 1 and 3 nm [4].

One of the unique and important properties of DNA is its ability to form double-stranded structure simply by combining two complementary single strands. This principle is one of the key principles responsible for the biological function of DNA, but it is also a reason why DNA becomes more interesting even for non-biological applications. Therefore, a closer look at it will be presented in the following section.

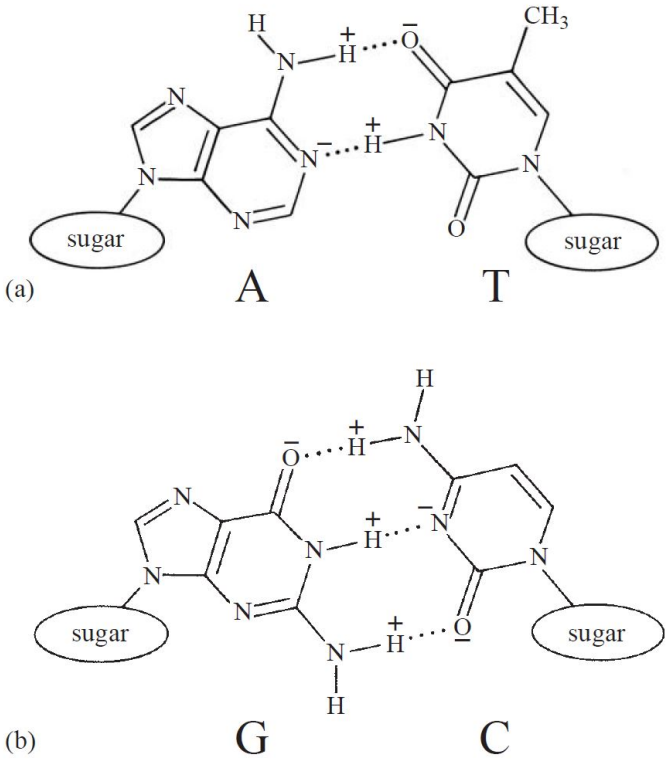

FIGURE 2.1: Watson-Crick base pairs established by hydrogen bonding; a) A-T, b) G-C, adapted from [7]

2.1.1 Watson-Crick base pairing

Two strands of double-stranded DNA (dsDNA) are held together by hydrogen bonding. The principle by which two nitrogenous bases establish hydrogen bonds and form a base pair (bp) is so-called Watson-Crick base pairing [5]. This process is highly selective and predictable [6].

Watson and Crick found already in 1953 that the most stable base pairs are adenine (A)- thymine (T) and guanine (G)- cytosine (C), shown in figure 2.1. Larger bases A and G are called *purines*, while C and T are *pyrimidines*. The physical origin of this pairing is in small surpluses of charges on certain atoms in nitrogenous bases. There is a surplus of negative charge on oxygens and nitrogens which are not connected to hydrogen, and a positive charge on those which are connected to hydrogen. Atoms that carry opposite charges connect via hydrogen bonding, as shown in figure 2.1, in a process called hybridization. This way, a base pair is formed, holding two DNA strands together in a double-helical structure [7].

2.1.2 DNA double helix

The DNA's structure is intimately related to its properties and stability. In aqueous solutions, DNA adopts a double helical structure thanks to the delicate balance between different interactions. Let's take a closer look at them [7].

A molecule of DNA is a biopolymer with repeating units called nucleotides. Each nucleotide consists of three different compounds: hydrophilic phosphates, hydrophilic sugar and hydrophobic nitrogenous bases. If such molecule is located in an aqueous environment, nitrogenous bases, being flat aromatic hydrophobic compounds, will

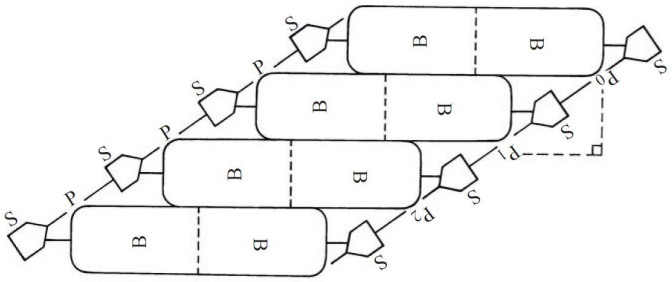

FIGURE 2.2: Skewed ladder DNA structure with no gaps between adjacent bases, adapted from [7]

try to minimize their contact with water. Luckily, phosphates and sugars will make this possible so that they will stay on the outer side of the DNA, while nitrogenous bases will "hide" on the inside. This is exactly how chemically distinct parts of the DNA are arranged in a double helix. However, hydrophobicity and hydrophilicity of DNA's components don't really explain the double helical structure. In theory, also less complex structures, such as simple ladder-like structure, could accommodate bases on the inner side of the molecule, keeping them away from the water. Why does then DNA form double helix?

To answer this question, one should start from considering geometrical constraints in the DNA. Normally, the distance between neighboring sugars or phosphate within one DNA chain is 6 Å. Taking into account that a covalent bond has a possibility to stretch to a certain degree, this distance cannot get larger that 6.5 Å or smaller than 5.5 Å. On the other side, the thickness of aromatic rings in nitrogenous bases is 3.3 Å and they are chemically rigid so this cannot change either. It is obvious that this leaves a gap of at least 2.7 Å between two flat bases in the chain. Since the bases are hydrophobic compounds that prefer to have as less contact with water as possible, there should be a way to fill in or eliminate this gap.

One possible structure with no gaps between nitrogenous bases would be skewed ladder structure shown in figure 2.2. But why is this then not a structure that DNA naturally adopts? Taking a look at individual atoms in such skewed ladder structure, one can see that there are too many unfavorably close contacts between neighboring atoms. However, it seems like nature found another way of excluding the water from the DNA's interior, simply by twisting this structure. The double helix is essentially nothing else but a twisted ladder. In double helix all unfavorable close contacts of neighboring atoms are minimized so that this structure is the most satisfying one for the DNA to adopt. It is stabilized by Watson-Crick base pairing, which was already described in the previous section 2.1.1, and by base-stacking interactions which will be discussed next.

2.1.3 The chemical origin of base-stacking in DNA

Base-stacking interactions in DNA act between neighboring bases or base pairs within the molecule. These attractive interactions are responsible for the structure of double helix and stability of the DNA. In this paragraph it will be briefly discussed what is the chemical origin of this attraction and how it influences the DNA structure [6].

The chemical theory of base-stacking in DNA explains interactions on the basis of partial electric charges in aromatic bases using the same theory that was used for describing stacking of long flat molecules- porphyrins [8].

According to the theory, there are three main contributions to the total base-stacking interactions:

1. Stacking of base pairs in order to avoid contact with water,
2. Repulsion of negative charges on upper and lower surfaces of bases,
3. Interaction of partial charges on individual atoms in bases.

Aromatic nitrogenous bases are hydrophobic molecules and tend to avoid contact with water. It is probably easy to understand that their hydrophobicity is a reason why bases tend to stack on top of each other in order to exclude water from the inner part of the DNA. Water establishes a network of hydrogen bonds, and if some water-insoluble object is immersed into the water, this network is disrupted. Hydrophobic objects, therefore, try to arrange themselves close to each other, and molecules of water are able to keep as many hydrogen bonds as possible. The optimal arrangement of bases in this case is the one where bases stack completely on top of each other. Another contribution comes from the negative charges located on upper and lower surfaces of bases, while positive charge is "sandwiched" between them. This type of interaction is strongly geometry dependent. Therefore, if two bases are in close contact along their upper and lower surfaces they repel each other to some extent. Due to this repulsive interaction, vertically stacked bases are not the most favorable molecular arrangement. To minimize this repulsion, bases can slightly slide to the left or to the right side. This way they can even take advantage of some attraction between positive and negative charges. Finally, the third electrical force arises between partial charges from individual atoms in the bases. Electronegative atoms as oxygen or nitrogen can generate partial negative charge, while hydrogens attached to carbon or nitrogen produce positive. However, these interactions are not very sensitive to small changes in the geometry of DNA. Thus, they can be understood as "fine-tuning" interactions within the double-helical structure.

The interplay of described contributions results in base-stacking interactions that are attractive in aqueous environment. Apart from acting within one molecule stabilizing its structure, attractions of the same nature can act also between terminal ends of two DNA duplexes. These so-called end-to-end stacking interactions can drive suspensions of DNA duplexes to an interesting phase behavior, but these aspects will be discussed into details in section 2.3.1.

2.1.4 Strucural DNA nanotechnology

As already mentioned earlier in this chapter, due to its unique structure and properties, DNA nowadays becomes the main focus of research directions that are not directly related to its biological function. The field of structural DNA nanotechnology uses this macromolecule as a generic (rather than genetic) molecular building material to construct complex two- and three- dimensional structures. Thanks to programmable intra- and intermolecular Watson-Crick base-pairing, it is possible to engineer predictable nanostructures with various levels of complexity.

The idea of structural DNA nanotechnology dates back to 1980s when Nadrian Seeman introduced the DNA as a material which could be used to produce all-DNA crystalline cages in order to position other biological macromolecules as guests inside of them [9, 10, 11, 12]. This can be achieved using DNA hybridization, carefully

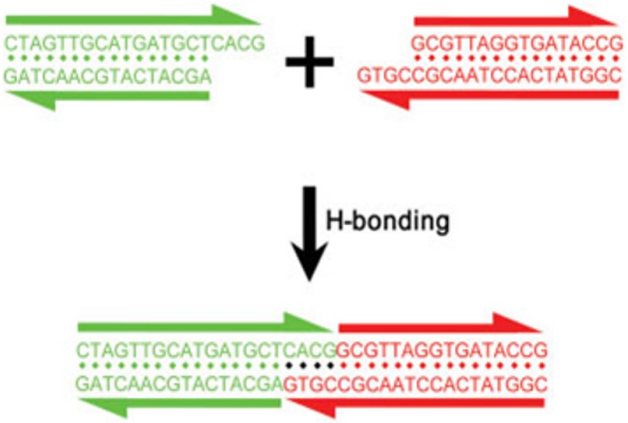

FIGURE 2.3: Sticky-end interaction between two DNA molecules resulting in one longer DNA duplex

designing nucleotide sequences to create stable branched DNA structures, and relying on convenient synthesis of designed sequences. The key interaction involved in this approach is sticky-end cohesion. Sticky ends are single stranded DNA overhangs located at terminal sites of DNA duplexes. They can act as a "glue", pairing with another complementary sticky ends of a neighboring DNA duplex to form base pairs. The product formed by such cohesion is a longer classic DNA double helix, as shown in figure 2.3. The predictability of sticky-end interactions includes control of intermolecular associations and controlled geometry at the point of cohesion. The sticky-end cohesion is a relatively new self-assembly approach in the area of soft matter and one of the best examples of programmable molecular recognition.

DNA origami

A remarkable simplification in production of DNA-based nanostructures appeared together with probably the most popular branch in this field, DNA origami, developed later in the 2000s thanks to Paul Rothemund[13]. "The problem is that we don't just want to make small stuff, we want to make complicated small stuff, cheaply and easily." These were the words that Paul Rothemund used in order to describe a revolutionary idea of DNA origami, which allowed the synthesis of quite complex DNA nanostructures in a rather simple way.

In the field of DNA nanotechnology, the yield of final structures is highly sensitive to stoichiometry, relative ratios of strands involved in the final structure. Also, in order to improve the quality of the product, final structures should be purified to remove any excess of unreacted strands. DNA origami uses large numbers of small single-stranded DNA fragments called *staples* to aid the folding of a very large single strand into target structures. The large DNA strand is typically viral DNA with a length of about 7000 bp.

First DNA origami architectures produced were squares, rectangles, stars, smiley faces, triangles with rectangular domains, and sharp triangles with trapezoidal domains and bridges between them, shown in figure 2.4. These DNA-based nanostructures were used to perform sigle molecule chemical reactions, as templates for protein assembly and to organize metal nanoparticles [14]. Nowadays, synthesis of even

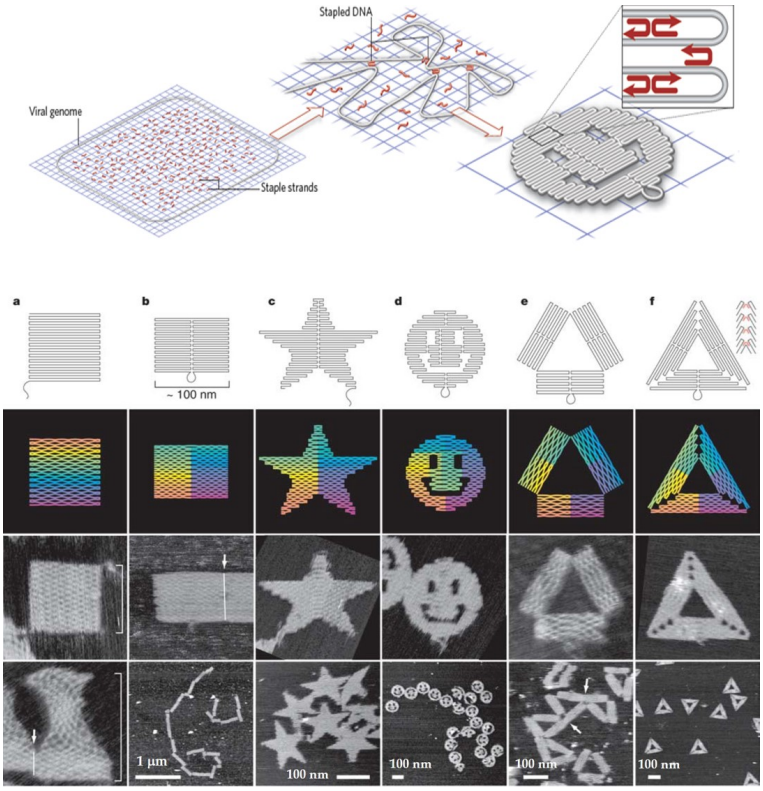

FIGURE 2.4: DNA origami in various shapes, from left to right: square, rectangle, star, disk with three holes (smiley face), triangle with rectangular domains, and sharp triangle with trapezoidal domains and bridges between them, adapted from [13]

more advanced three-dimensional DNA origami structures is possible [15, 12], opening new possibilities for promising applications molecular and cellular biophysics, energy transfer and photonics, diagnostics and therapeutics for human health [16].

2.2 Liquid crystal self-assembly

Everybody is more than familiar with the three states of matter: solid, liquid, and gas. However, there are certain materials which form phases that don't fall into any of these categories. The properties of these phases lie somewhere between those of a liquid and those of a crystal. Therefore, they are often called them *liquid crystals* (LC), while some prefer to name them *mesomorphic* phases [17] and the molecules forming them are *mesogens*. Generally, liquid crystals can be classified as thermotropic and lyotropic. Thermotropic LC consist mostly of organic molecules and exhibit LC phase transitions with changes in temperature. Lyotropic LC exhibit phase transitions as a function of temperature and concentration and consist of molecules dispersed in a solvent. Liquid crystals were discovered in 1888 by Austrian botanist Friedrich Reinitzer [18]. Reinitzer observed what he called *two melting points* in cholesteryl benzoat and cholesteryl acetate. He noticed that these compounds don't melt into clear, transparent, but always to a muddy, translucent liquid. When he further increased the temperature this muddiness would disappear. What Reinitzer observed was nothing else than the typical behavior of liquid crystals but he wasn't able to

explain the impact of his discovery. Reinitzer sent his samples then to crystallographer Otto Lehman who observed them under the polarizing microscope and called them *liquid crystals*.

In a crystal the building components are arranged in a regular periodic crystal lattice with a three-dimensional order. Liquids, on the other side, are not ordered and can flow easily. Liquid crystals, at the interface between these two, have long-range orientational order but a complete or partial absence of long-range positional order. Therefore, they exhibit anisotropic optical and mechanical properties. Depending on the degree of order, three commonly occurring forms of liquid crystals can be distinguished: nematics, smectics, and columnar phases.

Nematics and cholesterics Nematics have no *long range* positional order but there is some order in the direction of the mesogens. They tend to be parallel to a common axis called the nematic director **n**. The molecular organization in nematics is shown in figure 2.5 a).

In chiral molecules, the nematic phase formed exhibits a twist. A cholesteric (or chiral nematic) is locally very similar to nematics; molecules arrange themselves around a preferred axis **n**. However, the director is not constant in space, it undergoes a helical distortion, as shown in figure 2.5 b).

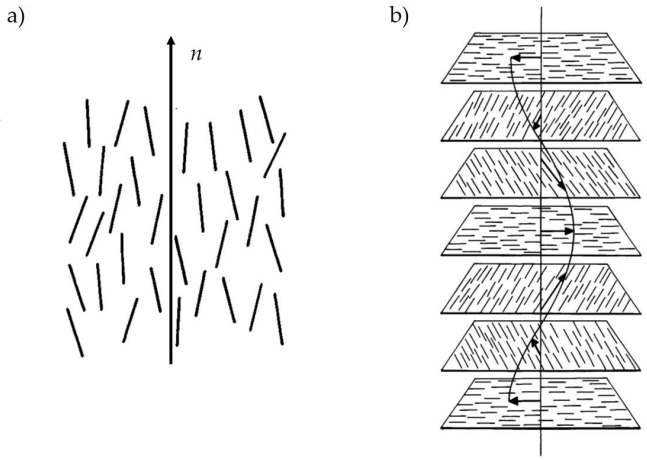

FIGURE 2.5: The arrangement of molecules a) in the nematic mesophase made up of rod-like molecules, b) in the cholesteric mesophase with helical structure, adapted from [19].

Smectics Smectic phase owes its name to the Greek word for soap, *smektikos*. Their layered structure shown in figure 2.6 with a well-defined interlayer spacing indicates that smectics are more ordered than nematics. The most common type of smectic phase, so called smectic A, has a layered structure with no long-range order within the layers, each layer is basically a two-dimensonal liquid made up of upright molecules. If molecules are arranged in a tilted way within a layer this kind of smectic phase is known as smectic C. Another subgroup of smectics are layered structures that exhibit long-range positional order within the layers, 'crystalline' smectics. The example of such 'crystalline' smectic phase is smectic B in which molecules are arranged in an upright hexagonal lattice.

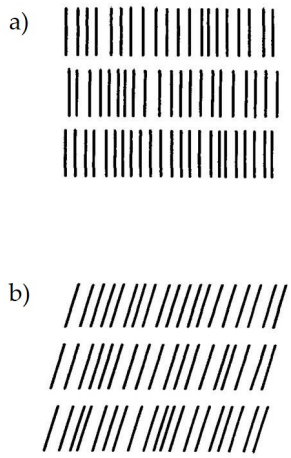

FIGURE 2.6: The schematic representation of a) smectic A and b) smectic C phase, from [19].

Columnar phases Columnar liquid crystal phase was initially named *discotic*, since the molecules making it up have a shape of a flat disc. However, the more recent findings showed that this kind of phase can be formed by molecules with different shapes as well. Therefore, it is common to refer to this phase as *columnar* liquid crystal phase. Columnar phases are often formed by disc-like or rod-like molecules stacked on top of each other to form columns which are laterally ordered in the plane perpendicular to the column axis. Depending on the lateral arrangement of the columns, *hexagonal, orthorombic, rectangular, tilted* etc. columnar phases can be distinguished.

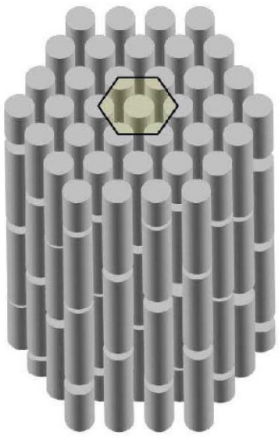

FIGURE 2.7: The schematic representation of a hexagonal columnar phase formed by rod-like particles, from [20].

2.3 Liquid crystalline phases of DNA

It has been known for more than 60 years now that DNA has the ability to form liquid crystal phases. In 1950s and 1960s it was found that naturally occurring long DNA chains form liquid crystals *in vitro* [21, 22]. Since the packaging of DNA *in vivo* is very tight, the understanding of liquid crystal phases in the highly concentrated solutions of DNA *in vitro* can be of great importance for the understanding of biological activity [23, 24, 25].

Ever since they were discovered, liquid crystalline phases of DNA have been extensively studied and investigated. Phase transitions of DNA observed so far using x-ray scattering, nuclear magnetic resonance (NMR) spectroscopy, polarized optical and freeze-fracture electron microscopy revealed a sequence of various lyotropic liquid crystalline phases. The liquid crystal phase sequence depends on the length of DNA duplexes as well as their preparation method [21, 26]. Slightly polydisperse rod-like dsDNA with a length of 146 $\pm$ 12 bp reveals a phase sequence of following phases with increasing concentration: isotropic (*I*), chiral nematic (cholesteric, *N**), columnar hexagonal (*Col*), and crystal (*K*) phase [27]. The aspect ratio *L/D* (where *L* is contour length, and *D* diameter of a rod) of these dsDNA fragments is $\sim$ 25.

In a system of hard rods with comparable *L/D* it is expected to observe a formation of smectic (*Sm*) phase. However, no *Sm* was observed in dsDNA. Livolant [28] argued that smectic phase in DNA is replaced by columnar ordering. However, at sufficiently high concentrations, layer-like ordering was found in aqueous suspensions of semiflexible fd virus particles [29] and in colloidal silica rods [30]. The absence of such ordering in DNA was therefore explained in terms of flexibility and polydispersity.

2.3.1 Liquid crystalline phases of ultra-short DNA

The work that anew sparked the interest for DNA liquid crystals was investigation of self-assembly of ultra-short DNA duplexes. According to the Onsager's theory [31] and computer simulations on phase behavior of hard spherocylinders by Bolhuis and Frenkel [32], short hard rods below aspect ratio of *L/D*= 3.7 are not able form liquid crystal phases. Surprisingly, a decade ago it was found that even ultra short fragments of dsDNA, in the range between 6 and 20 bp and with aspect ratios *L/D* between 1 and 3, are able to form liquid crystals [33]. The hypothesis for the driving force of such ordering lies in so called *end-to-end stacking interactions*. In the solution of blunt-ended dsDNA, helices stack on top of each other due to attractive end-to-end stacking interactions, as shown in figure 2.8. These interactions are essentially the same as base stacking interactions discussed in section 2.1.3 that stabilize the double helical structure of DNA. This way, short DNA duplexes form effectively linear aggregates that are long enough to undergo a phase transition from *I* to *N** and finally to *Col* phase. The absence of Sm phase was attributed to the polydispersity of formed aggregates.

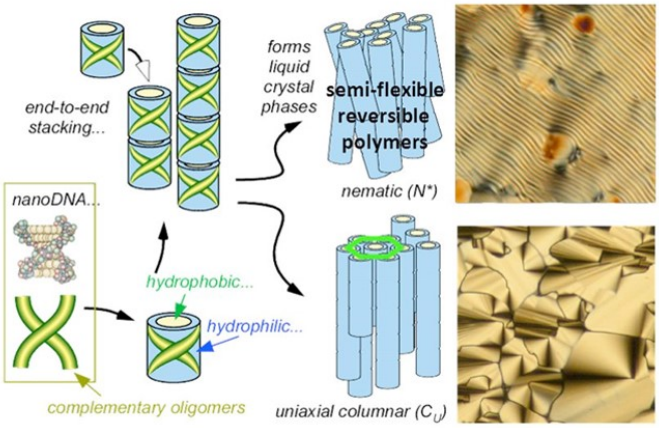

FIGURE 2.8: End-to-end stacking interactions between blunt ends of short DNA duplexes and liquid crystal ordering, adapted from [33]. The micropgraphs on the right-hand side represent the typical fingerprint texture of N* phase (top micrograph) and typical focal conical texture of *Col* phase (bottom micropgraph).

2.4 Entropy-driven transitions in soft matter

2.4.1 Crystallization of hard spheres

Certainly the simplest and most common colloidal models are *hard spheres*. They are definitely not anisotropic objects themselves but the basic concepts lying behind their crystallization can be extended to hard rods and isotropic to nematic phase transition. Therefore, it is worth to briefly address this issue as well.

Already in the 1950s and 1960s computer simulations showed that hard spheres undergo crystallization at certain volume fractions [34, 35]. Pusey and van Megen verified this transition experimentally in 1986 [36]. This behavior can be explained in terms of a competition between the loss of entropy related with the onset of positional order and the entropy gain related to the larger number of packing configurations possible in ordered state (minimization of excluded volume). Excluded volume of a spherical particle refers to the volume inaccessible to other particles due to the presence of the first one. Since the spheres are "hard", which means that they don't have any interaction unless they are in contact, in which case they experience infinite repulsions, the free energy of the system consists of entropic contributions only. The key to understanding why hard spheres crystallize lies in the fact that *random* close packing density (Φ= 0.64) is significantly smaller than the *hexagonal* close packing density value (Φ= 0.74). Therefore, system undergoes a phase transition to a crystalline state before the density becomes too large for the isotropic phase to run out of packing possibilities (figure 2.9).

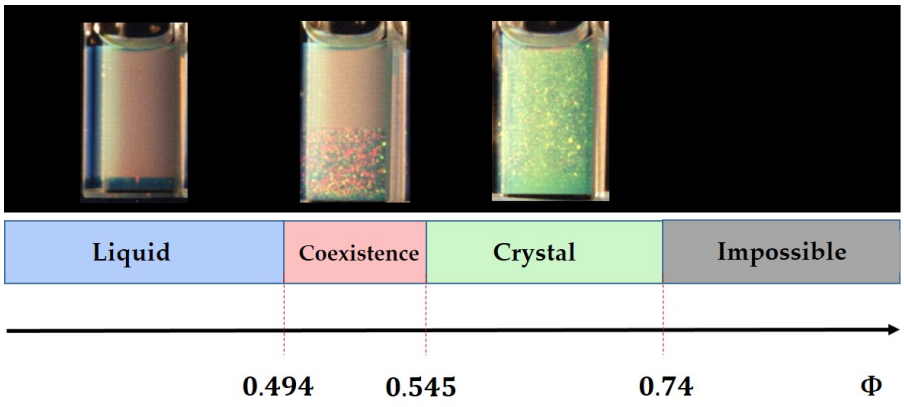

FIGURE 2.9: Phase transitions in hard spheres as a function volume fraction.

2.4.2 Isotropic to nematic transition in hard rods

Another common class of model systems is that of hard rods. The phase transition from isotropic (orientationally disordered) to nematic (orientationally ordered) liquid crystal phase for thin long, hard rods was described theoretically by Onsager already in 1949 [31]. Schematic representation of this phase transition together with phase boundaries is shown in figure 2.10. Onsager explains isotropic to nematic phase transition as entropy-driven. The loss of entropy associated with the orientational ordering of hard rods is compensated by the gain in entropy related to the minimization of the excluded volume. To understand this, one needs to recall that the excluded volume of hard rods is minimal if they are in a parallel orientation as in figure 2.11 a) and maximal when they are in a perpendicular orientation relative to each other (figure 2.11 b)).

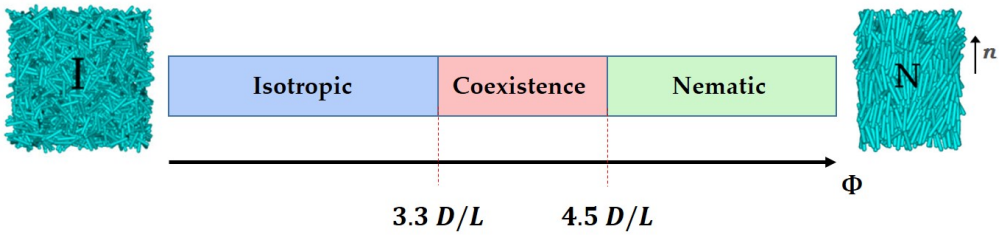

FIGURE 2.10: Isotropic to nematic phase transition in hard rods according to Onsager [31]. Isotropic phase is formed bellow volume fractions of Φ_I= 3.3D/L, while nematics appear above Φ_N= 4.5D/L. Coexistence of isotropic and nematic phase can be found in between.

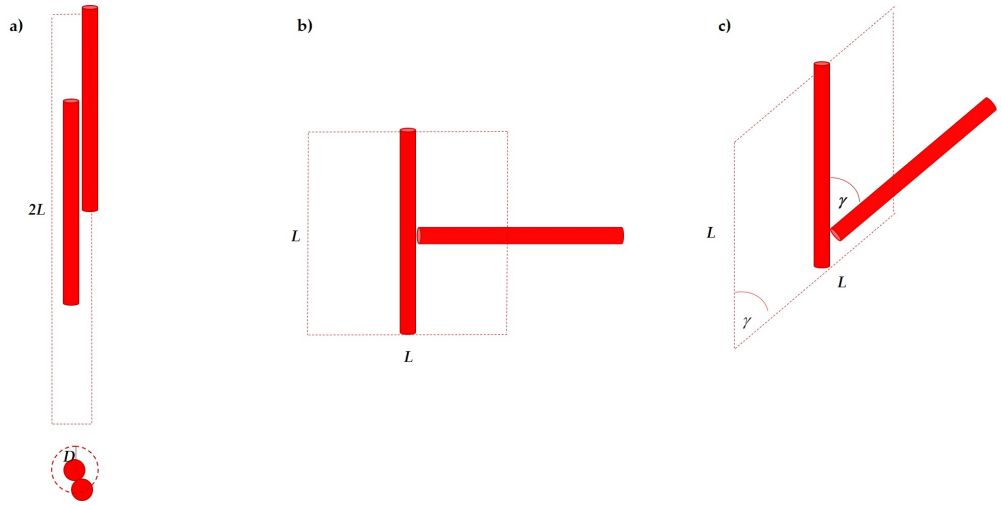

FIGURE 2.11: Excluded volume of rods (red dashed lines) a) in a parallel orientation, b) in a perpendicular orientation, and c) oriented with an angle γ between them, adapted from [37].

2.4.3 The Onsager approach to the nematic order for hard rods

As already mentioned earlier, in 1949 Onsager gave a theoretical explanation of isotropic to nematic phase transitions in hard rods. In this approach, few assumptions are included:

1. The only forces important are steric repulsion forces; the rods are not interpenetrable.
2. The volume fraction of rods is much smaller than unity.
3. The rods are very long, their length is much larger than their diameter (L$\gg$D).

If one starts from the case of a dilute gas of hard spheres, the free energy can be written in a following form:

$$F = F_0 + k_B T\{\log c + \frac{1}{2} c\beta_1 + O(c^2)\} \tag{2.1}$$

where F_0 is an additive constant, β_1 is the excluded volume, i.e. the volume inaccessible to the centre of sphere 1 if sphere 2 is fixed at the origin, and $O(c^2)$ means terms of order of c^2.

Moving on to the system of hard rods, one must specify not only the overall concentration c, but also the angular distribution of the rods. Therefore, the number of rods per unit volume ($cf_a d\Omega$) is introduced pointing in a small solid angle $d\Omega$ around a direction labeled with a unit vector $\mathbf{a}$. The sum of these solid angles must give the overall concentration c, so

$$\int f_{\mathbf{a}} d\Omega = 1. \tag{2.2}$$

The free energy of such system of hard rods is now

$$F = F_0 + k_B T\Big(\int f_{\mathbf{a}} \log(4\pi f_{\mathbf{a}} c) d\Omega + \frac{1}{2} c \iint f_{\mathbf{a}} f_{\mathbf{a}'} \beta_1 d\Omega d\Omega' \Big) + O(c^2) \tag{2.3}$$

where the second term describes the entropy loss associated with molecular alignment (i.e. a non-constant f). The third term describes the excluded volume effects. β_1(**aa'**) is the volume excluded by one rod in direction **a** as seen by one rod in direction **a'**. For spherocylinders, β_1 is

$$\beta_1 = 2L^2D|sin\gamma| + 2\pi D^2L + \frac{4}{3}\pi D^3. \tag{2.4}$$

γ is the angle between **a** and **a'**. The last two terms in the equation 2.4 are the end corrections which become negligible for long thin rods.

$$\beta_1 \sim 2L^2D|sin\gamma| \tag{2.5}$$

From the comparison of free energies for nematic and isotropic phase, the volume fraction Φ_{nem} above which nematic phase is formed is

$$\Phi_{\text{nem}} = 4.5D/L \tag{2.6}$$

while isotropic phase appears below significantly smaller Φ_{iso}

$$\Phi_{\text{iso}} = 3.3D/L. \tag{2.7}$$

2.4.4 Phase diagram of hard spherocylinders

Onsager's work on infinitely thin hard rods exhibiting purely entropic transition from isotropic to nematic phase at sufficiently high densities is an exact theory. However, theoretical study of this phase transition for experimental rod-like systems with smaller aspect ratios, such as rod-like virus particles [29], inorganic silica rods [30] and dsDNA [21], becomes challenging. In 1980s, Frenkel et al. offered an alternative way to explore a phase diagram of these systems by computer simulations. Monte Carlo simulations provide an evidence for entropy-driven transition from isotropic to nematic and smectic phase [32]. Hard spherocylinders were used as a model for rod-liek colloidal particles with short-ranged repulsive interactions. They are cylinders of length L and diameter D capped by a hemisphere at each end as shown in figure 2.12. The phase behavior of such objects is presented in terms of shape anisotropy L/D parameter (often also called aspect ratio) in figure 2.13. An extensive study in the region 3<L/D<5 was perfomed by McGrother *et al* [38].

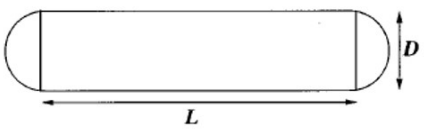

FIGURE 2.12: The hard spherocylinders model; spherocylinders consist of a cylinder with length L and diameter D capped with a hemisphere from both sides, from [38].

In the figure 2.13, reduced density $\rho^* = \rho/\rho_{cp}$ on the y-axis is the density relative to the density of regular close packing of spherocylinders which is expressed as: ρ_{cp}

$= 2/(\sqrt{2} + (L/D)\sqrt{3})$. According to the phase diagram, no liquid crystal nematic or smectic phase can be observed below L/D of 3.3.

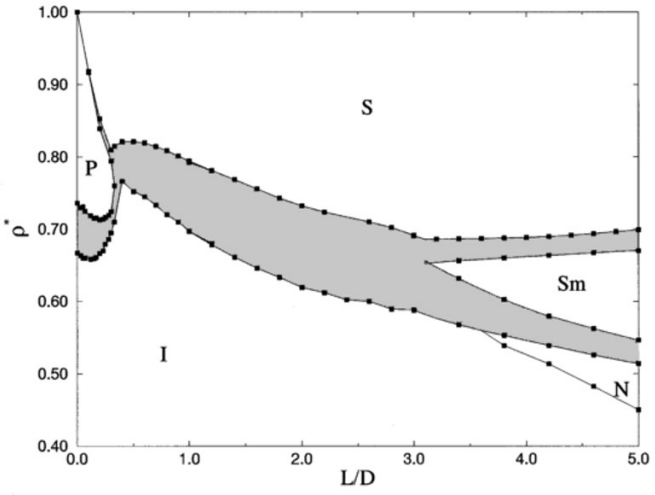

FIGURE 2.13: Phase diagram of hard spherocylinders for shape anisotropy parameters $L/D \leq 5$, from [32]. P stands for plastic solid, S for high-density orientationally ordered solid, I for low–density isotropic liquid, N for nematic and Sm for smectic A phase.

2.5 Patchy particles for programmable self-assembly

Molecular geometry and packing are determined by valence of atoms, so that for example a molecule of methane (CH_4) adopts a tetrahedral arrangement thanks to valence of the carbon atom. Similarly, colloids possessing some kind of valence would be able to adopt arrangements and architectures that are inaccessible for conventional colloidal particles [39]. One way to achieve this is by patterning the surface of colloidal particles with distinct patches [40]. An example is given in figure 2.14.

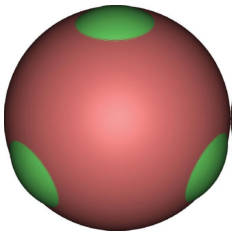

FIGURE 2.14: Colloidal particle with four identical green patches in tetrahedral geometry, from [41].

The patches can have different electrical (charge), physical and/or chemical properties. Such decoration ensures directionality in interactions of colloidal particles with their environment. Anisotropic interactions together with the possibility to control the position, number and type of patches open the path to a programmable self-assembly, which is absent in conventional colloidal particles. This approach is a powerful bottom-up materials design strategy with impressive control over the

target structures. An example is illustrated in figure 2.15. Phase diagram of patchy particles with two attractive red spots as a function of interaction strength and pressure is presented. It is evident that open crystalline configurations (Kagome lattice) made of self-assembled patchy colloids can be stabilized. This type of structures was found both in experiments [42] and simulations [43].

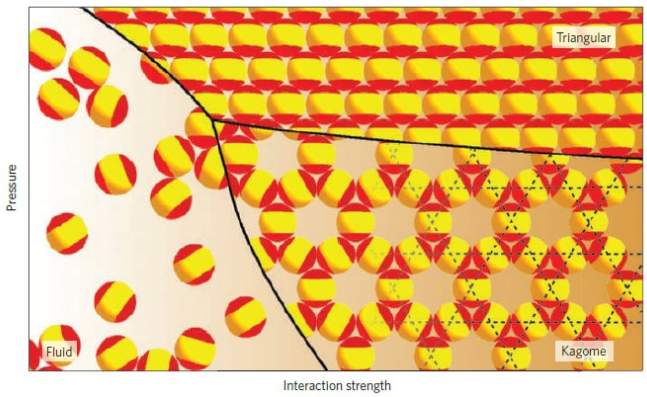

FIGURE 2.15: Phase diagram of patchy particles with two attractive red spots as a function of interaction strength and pressure. Increasing the interaction strength the particles self-assemble into Kagome lattice. For the same interaction strength, increasing the pressure the system self-assembles into closed-packed triangular lattice. From [44].

2.6 Block copolymers self-assembly

Block copolymers are large macromolecules built by combining two or more distinct polymer blocks, each of which is linear series of identical monomers [45]. Modern synthetic chemistry offers numerous possibilities for construction of different blocks configurations. Different molecular architectures can be found: linear, cyclic or branched (figure 2.16). Block copolymers can also be classified with respect to number of blocks in the structure, so one can distinguish between diblocks (made of two different blocks, A and B), triblocks (such as the simplest triblock ABA or the one made of three distinct monomer types ABC), or multiblocks (for example $(AB)_n$).

The chemical mismatch between different blocks in block copolymers drives such system towards their remarkable self-assembly behavior. Distinct blocks try to get away from each other as far as possible but since they are covalently connected no phase separation on macroscopic level is possible. Therefore, blocks tend to segregate on a molecular scale, in a process of so called *microphase separation*. In principle, thermodynamic forces that drive separation of distinct blocks are counterbalanced by entropic forces that are a result of covalent bonding. In order to keep blocks A and B apart from each other, a polymer must adopt extended configuration which leads to smaller number of possible configurations, compared to their randomly coiled state. For that reason, entropic force arises and limits the phase separation to mesoscopic dimensions. Commonly used parameter describing the non-ideal part of the mixing free energy in terms of free energy cost per monomer of contacts between A

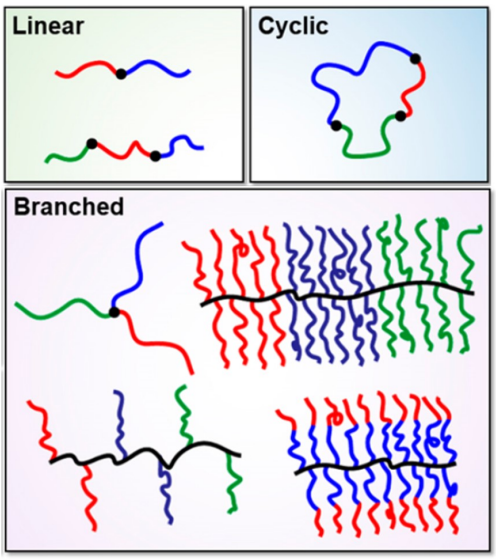

FIGURE 2.16: Molecular designs of block copolymers: linear, cyclic and branched, adapted from [46].

and B monomers divided by thermal energy k_BT is so called Flory-Huggins interaction parameter χ_{AB}

$$\chi_{AB} = (Z/k_BT)[\epsilon_{AB} - \frac{1}{2}(\epsilon_{AA} + \epsilon_{BB})]. \tag{2.8}$$

Z is number of nearest-neighbor monomers to a copolymer configuration cell, ϵ_{AB} is interaction energy between monomers A and B, and ϵ_{AA} and ϵ_{BB} interaction energy between monomers of each kind, AA and BB respectively. Positive values of χ_{AB} reflect the net repulsion between monomers A and B, while negative values indicate the attraction and drive towards mixing. Moreover, Flory-Huggins interaction parameter varies inversely with the temperature, meaning that the mixing is promoted at higher temperatures.

As a result of the balance between tendency for phase separation and the inability to achieve it, a wide array of different phases can be formed.

The phase behavior of AB diblock copolymer is well understood both theoretically and experimentally [46]. A phase diagram of AB diblock comparing theory and experiment is shown in figure 2.17. In theoretical phase diagram shown in a), lamellar (L) and gyroid (G) phase can be found, followed by hexagonally packed cylinders (C) and body-centered cubic spherical phase (S), with increased compositional assymetry. At the borderline between disordered state and S phase a narrow region with close packed spheres (CPS) is found. Experimental phase diagram shown in b) looks quite similar to the theoretical one, with a minor difference in a narrow region where a complex phase called perforated layers (PL) appears. This example of the diblock phase behavior is the simplest case. However, by introducing another block into the block copolymer structure, the number and complexity of the phases formed significantly increases.

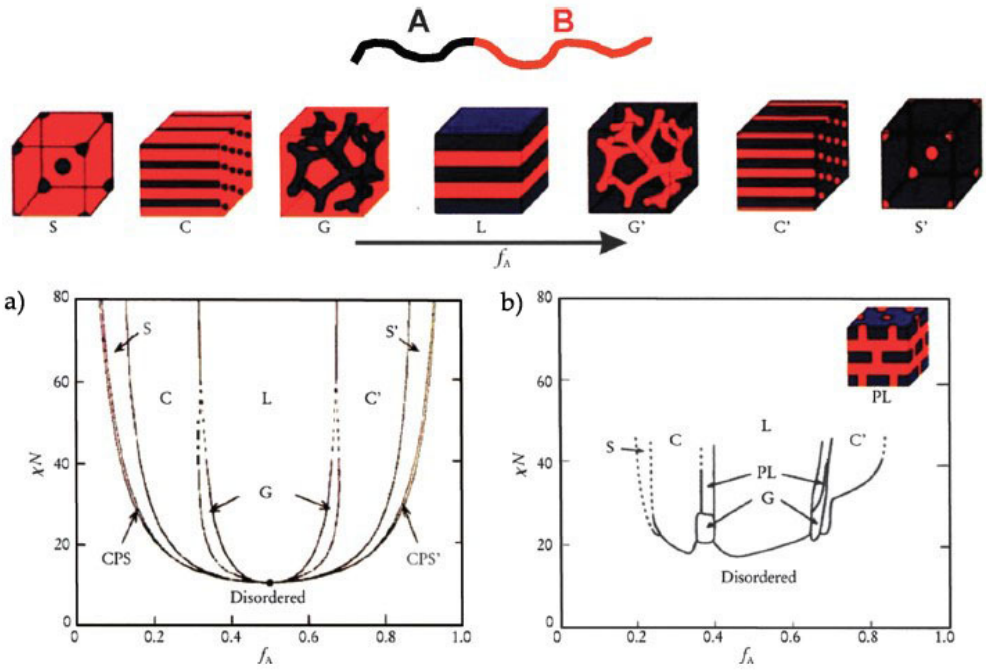

FIGURE 2.17: Phase diagram of linear AB diblock copolymer represented as segregation parameter χ_N as a function of volume fraction of A block f_A, comparing a) theory and b) experiment where f_A represents volume fraction of polyisoprene in poly(isoprene-styrene) diblock, adapted from [47].

Bibliography

[1] M. Rubinstein and R. H. Colby. *Polymer physics*. Oxford University Press, 2003.

[2] P. Hagerman. Flexibility of DNA. *Annu. Rev. Biophys. Biophys. Chem.*, 17:265–286, 1988.

[3] C. G. Baumann, S. B. Smith, V. A. Bloomfield, and C. Bustamante. Ionic effects on the elasticity of single DNA molecules. *Proceedings of the National Academy of Sciences of the United States of America*, 94:6185–6190, 1997.

[4] M. C. Murphy, I. Rasnik, W. Cheng, T. M. Lohman, and T. Ha. Probing Single-Stranded DNA Conformational Flexibility Using Fluorescence Spectroscopy. *Biophysical Journal*, 86:2530–2537, 2004.

[5] J. D. Watson and F. H. Crick. Molecular Structure of Nucleic Acids: A Structure for Deoxyribose Nucleic Acid. *Nature*, 171:737–738, 1953.

[6] E. T. Kool. Hydrogen bonding, base stacking, and steric effects in DNA replication. *Annual Review of Biochemistry and Biomolecular structure*, 30:1–22, 2001.

[7] A. A. Travers, C.R. Calladine, H. R. Drew, and B. Luisi. *Understanding DNA*. Elsevier, 2004.

[8] C. A. Hunter. Sequence-dependent DNA structure. *Journal of Molecular Biology*, 18:157–162, 1996.

[9] N. R. Kallenbach, R. Ma, and N. C. Seeman. An immobile nucleic acid junction constructed from oligonucleotides. *Nature*, 305:839–831, 1983.

[10] N. C. Seeman. DNA in a material world. *Nature*, 421:427–431, 2003.

[11] N. C. Seeman. Nanomaterials Based on DNA. *Annual Review of Biochemistry*, 79:65–87, 2010.

[12] N. C. Seeman and H. F. Sleiman. DNA nanotechnology. *Nature Reviews Materials*, 3:1–23, 2017.

[13] P. W. K. Rothemund. Folding DNA to create nanoscale shapes and patterns. *Nature*, 440:297–302, 2006.

[14] J. Nangreave, D. Han, Y. Liu, and H. Yan. DNA origami: A history and current perspective. *Current Opinion in Chemical Biology*, 14:608–615, 2010.

[15] S. M. Douglas, H. Dietz, T. Liedl, B. Högberg, F. Graf, and W. M. Shih. Self-assembly of DNA into nanoscale three-dimensional shapes. *Nature*, 459:414–418, 2009.

[16] A. V. Pinheiro, D. Han, W. M. Shih, and H. Yan. Challenges and opportunities for structural DNA nanotechnology. *Nature Nanotechnology*, 6:763–772, 2011.

[17] P. G. De Gennes and J. Prost. *The physics or liquid crystals*. Oxford University Press, 2nd edition, 1993.

[18] Ingo Dierking. *Textures of liquid crystals*. Wiley-VCH, Weinheim, 2003.

[19] S. Chandrasekhar. *Liquid crystals*. Cambridge University Press, Cambridge, 2nd edition, 1992.

[20] Eric Grelet. Hexagonal order in crystalline and columnar phases of hard rods. *Physical Review Letters*, 100:1–4, 2008.

[21] T. E. Strzelecka, M. W. Davidson, and R. L. Rill. Multiple liquid crystal phases of DNA at high concentrations. *Nature*, 331:457–460, 1988.

[22] T. Bellini, R. Cerbino, and G. Zanchetta. DNA-based soft phases. In Carsten Tschierske, editor, *Liquid Crystals*, pages 225–279. Springer, Berlin, Heidelberg, 2011.

[23] F. Livolant. Ordered phases of DNA in vivo and in vitro. *Physica A*, 176:117–137, 1991.

[24] R. L. Rill, F. Livolant, H. C. Aldrich, and M. W. Davidson. Electron microscopy of liquid crystalline DNA: direct evidence for cholesteric-like organization of DNA in dinoflagellate chromosomes. *Chromosoma*, 98:280–286, 1989.

[25] W. C. Earnshaw and S. R. Casjens. DNA packaging by the double-stranded DNA bacteriophages. *Cell*, 21:319–331, 1980.

[26] F. Livolant and A. Leforestier. Condensed phases of DNA: structures and phase transitions. *Prog. Polym. Sci.*, 21:1115–1164, 1996.

[27] K. Merchant and R. L. Rill. DNA length and concentration dependencies of anisotropic phase transitions of DNA solutions. *Biophysical Journal*, 73:3154–3163, 1997.

[28] F. Livolant, A. M. Levelut, J. Doucet, and J. P. Benoit. The highly concentrated liquid-crystalline phase of DNA is columnar hexagonal. *Nature*, 339:724–726, 1989.

[29] Z. Dogic and S. Fraden. Smectic phase in a colloidal suspension of semiflexible virus particles. *Physical Review Letters*, 78:2417–2420, 1997.

[30] A. Kuijk, D. V. Byelov, A. V. Petukhov, A. van Blaaderen, and A. Imhof. Phase behavior of colloidal silica rods. *Faraday Discussions*, 159:181, 2012.

[31] L. Onsager. The effects of shape on the interation of colloidal particles. *Annals New York Academy of Sciences*, 51:627–659, 1949.

[32] P. Bolhuis and D. Frenkel. Tracing the phase boundaries of hard spherocylinders. *The Journal of Chemical Physics*, 106:666–687, 1997.

[33] M. Nakata, G. Zanchetta, B. D. Chapman, C. D. Jones, J. O. Cross, R. Pindak, T Bellini, and N a Clark. End-To-End Stacking and Liquid Crystal Formation of 6- to 20-Base Pair DNA Duplexes. *Science*, 318:1–4, 2007.

[34] B. J. Alder and T. E. Wainwright. Phase transition for a hard sphere system. *J. Chem. Phys.*, 27:1208, 1957.

[35] W. W. Wood and J. D. Jacobson. Preliminary results from a recalculation of the Monte Carlo equation of state of hard spheres. *The Journal of Chemical Physics*, 27:1207–1208, 1957.

[36] P. N. Pusey and W. van Megen. Phase behaviour of concentrated suspensions of nearly colloidal spheres. *Nature*, 320:2–4, 1986.

[37] D. Frenkel. Order through entropy. *Nature Materials*, 14:9–12, 2015.

[38] S. C. McGrother, D. C. Williamson, and G. Jackson. A re-examination of the phase diagram of hard spherocylinders. *Journal of Chemical Physics*, 104:6755–6771, 1996.

[39] Y. Wang, Y. Wang, D. R. Breed, V. N. Manoharan, L. Feng, A. D. Hollingsworth, M. Weck, and D. J. Pine. Colloids with valence and specific directional bonding. *Nature*, 491:51–55, 2012.

[40] S. C. Glotzer and M. J. Solomon. Anisotropy of building blocks and their assembly into complex structures. *Nature Materials*, 6:557–562, 2007.

[41] E. Bianchi, R. Blaak, and C.N. Likos. Patchy colloids: State of the art and perspectives. *Physical Chemistry Chemical Physics*, 13:6397–6410, 2011.

[42] Q. Chen, S. C. Bae, and S. Granick. Directed self-assembly of a colloidal kagome lattice. *Nature*, 469:381–384, 2011.

[43] F. Romano and F. Sciortino. Two dimensional assembly of triblock Janus particles into crystal phases in the two bond per patch limit. *Soft Matter*, 7:5799–5804, 2011.

[44] F. Romano and F. Sciortino. Patchy from the bottom up. *Nature Materials*, 10: 171–173, 2011.

[45] F. S. Bates and G. H. Fredrickson. Block copolymers-designer soft materials. *Physics Today*, 52:32–38, 1999.

[46] C. M. Bates and F. S. Bates. 50th anniversary perspective: Block polymers-pure potential. *Macromolecules*, 50:3–22, 2017.

[47] Y. Mai and A. Eisenberg. Self-assembly of block copolymers. *Chemical Society Reviews*, 41:5969–5985, 2012.

Chapter 3

Experimental techniques and materials

This chapter contains an overview of all experimental techniques used for the work presented in this thesis. Basic principles of small-angle X-ray scattering and polarized optical microscopy, interaction of DNA with the magnetic field, and basics of gel electrophoresis will be discussed. Additionally, a brief description of computer simulation methods will be given. Finally, extensive list of all used oligomers and other materials is provided, as well as protocols used for the synthesis of DNA constructs.

3.1 Experimental techniques

3.1.1 Scattering techniques

Scattering techniques are widely used for probing the microscopic structure of matter. In soft matter, the commonly used non-destructive scattering techniques are X-ray, neutron, and light scattering. The choice of the appropriate technique depends on the length scales in the sample, and how radiation interacts with the matter [1]. Generally speaking, the smallest length scales which can be probed are $\lambda/2$ where λ is the wavelength. The wavelengths used in X-ray scattering are typically ~ 1 Å and the upper limit for the measured structures is around 1000 Å. For the light scattering $\lambda \sim 0.5$ µm, so the length scales up to 200 µm can be observed. In order to achieve contrast with X-rays, a difference in electron density must be present in the sample. Therefore, heavier elements scatter more strongly than the lighter ones. As an alternative, neutron scattering can be used. Neutrons interact with atomic nuclei and are sensitive to the difference of atomic species in the sample. The scattering of neutrons differs for isotopes of the same elements, which allows *contrast matching*. Finally, light is scattered by fluctuations in dielectric constant of a material.

For this work, small-angle X-ray scattering (SAXS) technique was a method of choice, considering the length scales and the chemical nature of the investigated systems, and simplicity of the sample preparation. The typical SAXS instrumentation consists of three main parts: X-ray source, sample holder and a detector. Results presented in this thesis are obtained using two types of instrumentation with distinct X-ray sources. The first one is in-house scattering setup, Gallium Anode Low Angle X-ray Instrument (GALAXI) using a laboratory source in form of a liquid gallium anode (MetalJet), while the other type relies on synchrotron source. In both SAXS

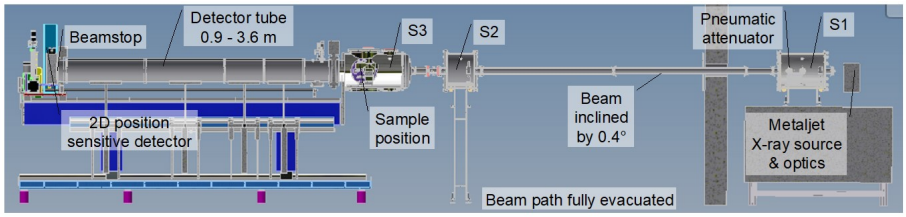

FIGURE 3.1: Schematic representation of GALAXI with its main components. The beam direction is from right to left [5].

instruments, a Dectris Pilatus 1M detector was used with resolution 981 x 1043 pixels and a pixel size of 172 x 172 μm^2. SAXS data were analyzed using Fit2D software [2].

X-rays

In the late 19th century, Wilhelm Conrad Röntgen discovered X-rays. The discovery immediately attracted extensive attention and soon X-ray imaging has become widely used for medical applications. Nowadays, the application of X-rays becomes even wider; X-ray scattering and diffraction serve as an useful and convenient tool for identification of different structures, and are often used to investigate soft matter [3].

20 years after Röntgen's discovery, crystallography was born and its father, Max von Laue, received a Nobel Price in Physics in 1914. The further progress in this area resulted in important contributions to the crystallography of biological molecules when Dorothy Hodgkin solved the structure of cholesterol in 1937, and later also the structure of penicilin and vitamin B_{12} for which she received Nobel Price in Chemistry in 1964. Finally, probably one of the most famous discoveries in the modern science, the identification of the DNA's double helical structure by Watson and Crick, relies on the X-ray crystallography [4]. In 1950s, Watson and Crick used diffraction images produced by Rosalind Franklin which allowed them to propose the famous model of DNA's structure.

Generation of X-rays

X-rays are electromagnetic radiation of wavelengths typically in the range between 0.01 and 10 nm. Those of shorter wavelengths and the highest energies are referred to as *hard X-rays* while those with longer wavelengths but lower energies are *soft X-rays*. Generation of X-rays is typically achieved by bombardment of metal anode with fast electrons. The electrons are accelerated through a high-voltage gradient on a cathode and hit the surface of a water-cooled anode (usually made from copper). As a result, two different effects ae observed: First, due to deceleration of electrons interacting with charges within the atoms of the target, a broad continuous spectrum of radiation is produced (so called *Bremsstrahlung*). Second, some of the incident electrons have sufficient energy to expel an electron from the inner shell of the target creating the vacancy. When a higher shell electron undergoes a transition to the lower energy level and fills in the vacancy, radiation K_α is emitted. Additionally, another electron transition yields K_β radiation which is often absorbed and removed by applying an X-ray filter [3].

The power load which can be applied to a solid metal anode is limited by the maximum heat dissipation. Therefore, when a higher power is needed, rotating anodes can be used. The most recent improvement was introducing a jet of liquid metal that serves as anode. A high speed jet of liquid metal (gallium) is used as anode in GALAXI, a small angle X-ray diffractometer which serves the needs of small angle X-ray scattering, designed and built at the Jülich Centre for Neutron Science (JCNS) in Forschungzentrum Jülich (figure 3.1). The Bruker Metaljet X-ray Source can accept much higher power loads than conventional solid anodes and produce much brighter X-ray beam (λ= 1.3414 Å), which is the main advantage of this laboratory setup [5].

Higher power and coherent X-ray beam with small beam sizes in the range of µm can be achieved using synchrotron sources running at big facilities. Synchrotron radiation is generated when high-energy electrons circulating in a storage ring are being deflected by magnetic fields. Electrons emitted from an electron gun are sent to a linear accelerator where they are gradually accelerated using electric fields until they reach a speed close to the speed of light. The electrons then enter the booster synchrotron to gain additional energy before they are sent to the storage ring. As they orbit around the storage ring at the speed of light and in high vacuum, they pass through series of *bending magnets*, *undulators* or *wigglers*, and *focusing magnets*. Each time they pass through these magnetic devices, the electrons are deflected from their straight path and emit X-rays tangentially to the plane of the electron beam [6]. The X-rays are then directed to the beamlines equipped with the instrumentation necessary for experiments to take place [3]. Experiments for the work presented in this thesis are performed at the Dutch-Belgian Beamline (DUBBLE) station BM26B (λ= 1.012 Å) [7] to probe the complex structures such as cubic network phases presented in chapter 6.

Custom made sample holders for GALAXI

In order to automatize the measurements to a certain degree, custom sample holder with temperature control was designed and made. The holder shown in figure 3.2 is made to accommodate capillaries during measurements in GALAXI setup. The two-axes motor in the sample chamber of GALAXI allows to automatically change the position of the holder (in two directions) and expose five different samples to the X-ray beam subsequently.

FIGURE 3.2: GALAXI sample holder for five capillaries. Inlet and outlet allow the circulation of water in the back of the holder in order to control the temperature of the samples.

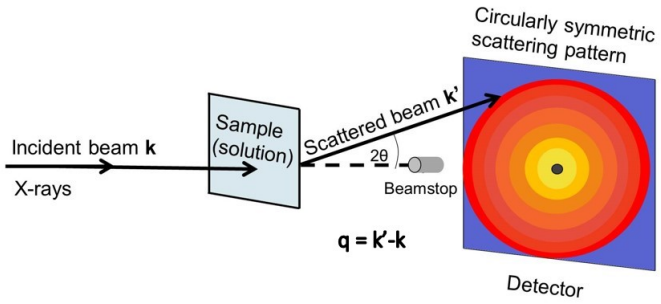

FIGURE 3.3: Schematic representation of a typical SAXS experiment.

Basic principles of X-ray scattering

Typical Small Angle X-ray Scattering experiment is schematically shown in figure 3.3. As incident beam hits the sample, a portion of X-rays passes through unaffected while the rest interacts with matter. The interacting portion of X-rays is elastically scattered by electrons in the sample: no change of wavelength or energy occurs, only transfer of momentum between an electron and the X-ray beam.

The scattering angle between an incident wave vector **k** and scattered wave vector **k'** is 2θ. The scattering vector **q** is defined as the difference between **k'** and **k**:

$$\mathbf{q} = \mathbf{k}' - \mathbf{k} \tag{3.1}$$

Since the wave vector **k** is related to the wavelength of the beam by k= $2\pi/\lambda$ and considering the scattering triangle in figure 3.3:

$$q = \mid \mathbf{q} \mid = 2ksin\theta = \frac{4\pi}{\lambda} sin\theta \tag{3.2}$$

The scattering vector **q** can be expressed also in terms of dimension d in the system as:

$$q = \frac{2\pi}{d} \tag{3.3}$$

The scattering amplitude $A(q)$ is a Fourier transformation of the electron density of the scattering molecules relative to solvent $\Delta\rho$= ρ(r)- ρ(s):

$$A(q) = \int_V \Delta\rho(r) e^{iqr} dr \tag{3.4}$$

The scattering intensity is collected by a flat two-dimensional detector positioned perpendicularly to the **k** and located at some distance behind the sample, as shown in figure 3.3. Only X-rays scattered in the forward direction can be registered at the detector, which limits the range of accessible **q** values. However, this range can be tuned by changing the sample to detector distance.

Scattering from crystalline and non-crystalline matter

In a typical SAXS experiment, a degree of order in the sample can be qualitatively reflected on the appearance of the 2D scattering pattern recorded at the detector. The scattering patterns of monocrystalline, paracrystalline and aligned paracrystalline sample are sketched in figure 3.4. Scattering from a single crystal (figure 3.4 a)) leads

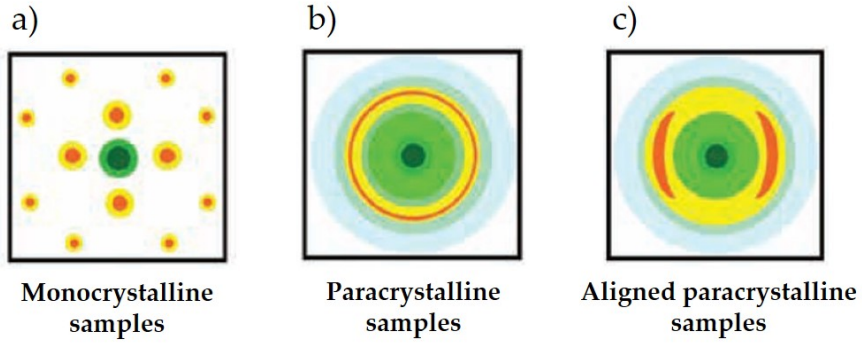

FIGURE 3.4: Sketch of two-dimensional scattering patterns for samples with different degrees of order: a) monocrystalline, b) paracrystalline, and c) aligned paracrystalline samples, adapted from [8].

to diffraction maxima appearing only at distinct positions. However, single crystals are rare in soft biological systems such as DNA-based systems used in this thesis. Generally, these materials contain numerous crystallites with random orientations. The spots in the scattering pattern are replaced with diffraction rings as in b). However, by applying external fields (for example, shear or magnetic field) the crystallites can be aligned so that the rings become more pronounced arcs as presented in figure 3.4 c).

X-ray scattering from smectic liquid crystals

A layered liquid crystalline phase formed by rod-like particles (smectic phase) will be often discussed in this thesis. Thus, a specific case of scattering from smectic liquid crystals will be described here. It will be briefly demonstrated how packing of the rod-like molecules into smectic layers affect the 2D scattering pattern. In the top row of figure 3.5 different degrees of molecular alignment, in terms of positional and orientational order, are shown. In the lower row, sketches of corresponding two-dimensional scattering pattern are given. For the exaggerated case a), in which particles are arranged into almost perfect flat layers and all point in the same direction, the scattering pattern consists of two sets of well-defined spots. Closely-spaced spots are related with the order along the layer normal, and the distance between them depends on the typical layer spacing in the sample. The sharpness of these spots implies that the layers are completely straight. Moreover, the boundaries between layers are sharp and correlation length along the layer normal is very large. The outer wide-angle spots reflect in-layer order and are connected with intermolecular distances. Due to the absence of perfect translational order along the layers there is a distribution of different intermolecular distances in the sample and the wide-angle peaks are therefore smeared out radially.

In b), there is some degree orientational disorder present within the layers and the wide-angle spot smears out azimuthally. Such disorder will not have a great influence on small-angle spots assuming that layers are perfectly flat and well-defined. However, it is expected that higher order peaks will become less visible. If particles are allowed to intertwine between layers as in c), this causes loss of higher order small-angle peaks. Finally, assuming that the layers are not flat, small-angle peaks smear out azimuthally which results in a scattering pattern with two sets of arcs, as shown in d).

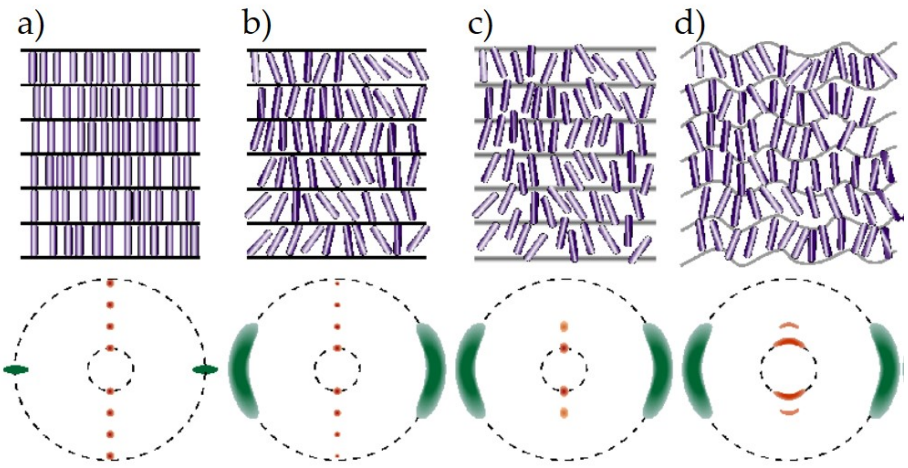

FIGURE 3.5: Sketch of two-dimensional scattering patterns for smectic A phase with different degrees of orientation: a) upright particles arranged in idealized flat layers, b) flat layers with introduced certain degree of orientational disorder among particles, c) particles having disordered orientations and intertwining between layers, and d) particles arranged into non-flat layers , adapted from [9].

3.1.2 DNA and magnetic field

Another property of DNA that allows us align DNA-based constructs using external magnetic field and gain a deeper insight into their self-assembly behavior is diamagnetism. DNA is a diamagnetic molecule with a negative diamagnetic anisotropy [10]. This means that the DNA doesn't posses permanent magnetization without external magnetic field. However, in the presence of the latter, the DNA will undergo a magnetoorientation due to the anisotropy of diamagnetic susceptibilities in the molecule. Diamagnetic anisotropy is the property of many molecules with anisotropy in shape such as rods and discs. Two kinds of diamagnetic behavior can be distinguished: molecules with positive diamagnetic anisotropy $\Delta\chi > 0$ ($\mid \chi_{\parallel} \mid < \mid \chi_{\perp} \mid$) orient their rotational symmetry axes parallel to the applied magnetic field B, while those with the negative one $\Delta\chi < 0$ ($\mid \chi_{\parallel} \mid > \mid \chi_{\perp} \mid$) orient their rotational symmetry axis in a plane perpendicular to B [11].

The rotation of these molecules in the presence of external magnetic field occurs in order to achieve a minumum energy configuration. The degree of alignment β depends on the ratio of magnetic and thermal energies and is usually very small for DNA bases. In case of DNA, β is increased by the factor of N originating from the number of nucleobases stacked on top of one another.

3.1.3 Polarized optical microscopy

While scattering methods are providing reconstruction of the object in an indirect way- the scattering pattern is recorded and reconstruction is done mathematically- microscopy allows to reconstruct an object simply by means of a lens system. These two methods are complementary and often used combined to get the complete picture of an observed system in soft matter.

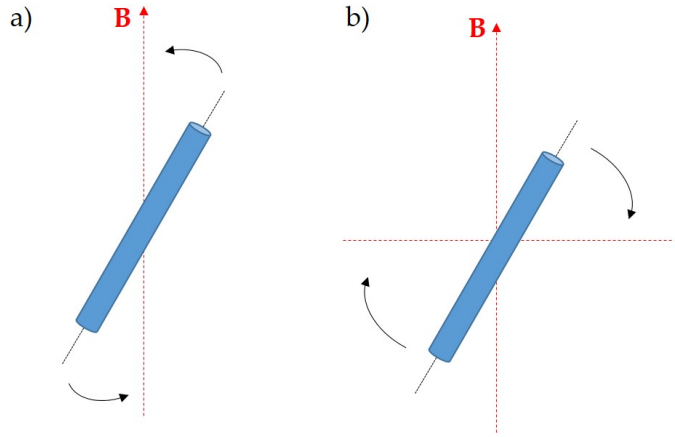

FIGURE 3.6: Orientation of diamagnetic molecules in a magnetic field. A rod-like molecule with a) positive diamagnetic anisotropy and b) negative diamagnetic anisotropy.

Polarized optical microscopy (POM) is a light microscopy technique which takes advantage of polarized light which strongly interacts with birefringent[1] samples. Typical polarized microscope is shown in figure 3.7 [12]. Usually, a light source is a halogen light bulb which emits white light. The light is then reflected upwards by a mirror, passes through a lens and is linearly polarized by a sheet polarizer. At this point it is possible to insert a wavelength filter (λ - filter) that can select a certain wavelength of a light which then enters the condensor. The condensor collects the light in order to provide a uniform illumination of the sample which is usually placed at rotatable stage. The transmitted light reaches the objective, passes through an analyzer. Finally, the image can be observed through an ocular or an eyepiece, or projected onto a camera mounted on the microscope. The contrast is generated when the plane-polarized light interacts with a birefringent sample and thereby two individual wave components are produced polarized in mutually perpendicular planes, as illustrated on the left-hand side of figure 3.7.

POM images for this thesis were obtained using colored CMOS camera (Motic) installed in a Axioplan 2 upright microscope working in a transmission mode between crossed polarizers. In order to investigate the phase behavior of fully paired and gapped duplexes, controlled drying experiments were carried out. During the experiments, concentrated DNA solutions in the isotropic phase were loaded into hollow rectangle glass tubes (VitroCom) of thickness between 20 and 50 μm and sealed from one side. Therefore, controlled evaporation occured from one side only resulting in a concentration gradient of DNA across the tube. Images analysis was performed using Image J software.

3.1.4 Gel electrophoresis

Only 10 years after the gel electrophoresis was introduced as a technique for separation of proteins in 1950s, Vin Thorne used a gel electrophoresis for the analysis of DNA. Ever since then, gel electrophoresis is used as a simple technique for separation, identification, and purification of DNA fragments. Upon the application of

[1]Birefringence is the optical property of a material having a refractive index that depends on the polarization and propagation direction of light.

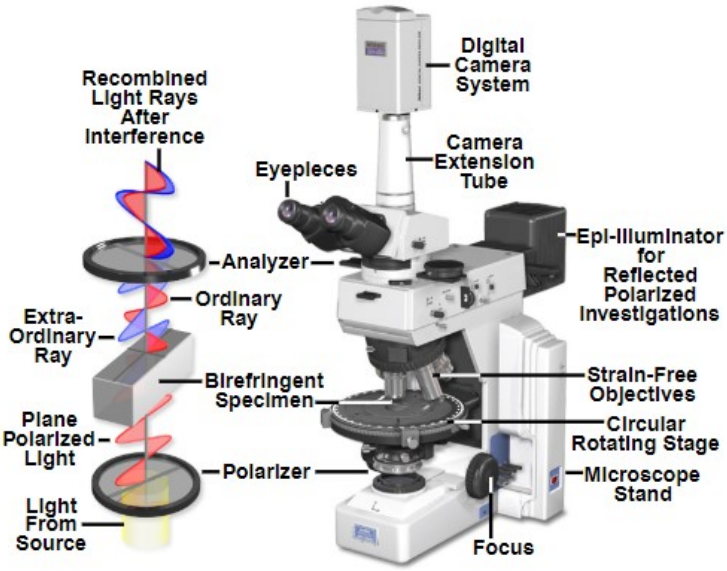

FIGURE 3.7: Schematic representation of a typical polarized microscope setup, from [13].

the electric field, negatively charged DNA molecules migrate through the gel matrix and get separated according to their size/charge ratios. After separation, the fragments can easily be visualized staining the gel with fluorescent intercalating dyes, such as Ethidium Bromide, and visualizing it under UV light [14].

Two commonly used types of electrophoresis gels are native polyacrylamide (PAGE) and agarose gels. Acrylamide, soluble in water, creates a polyacrylamide gel in the polymerization process. The pores of the gel can have various sizes, with higher concentrations of acrylamide in water yielding gels with smaller pore sizes. PAGE gels generally have a great resolving power being able to resolve even differences as small as 1 base pair and are often used for separation of DNA in the range between 5 and 500 base pairs. Agarose gels, on the other side, have lower resolving power but greater separation range. Agarose is a polysaccharide extracted from red seaweed. Once they solidify, solutions of agarose typically in the range of 0.1% to 4% form a three-dimensional mesh held together by hydrogen bonds. The pores in the mesh can be of different sizes, depending on the concentration of agarose. Such gels are usually used for gel electrophoresis of DNA from 50 to few millions base pairs [14]. Typical image of a gel after gel electrophoresis experiment is shown in figure 3.8, and it shows how different lengths of DNA fragments can be identified and even separated from each other.

In this work, gel electrophoresis was used in order to confirm the assembly of different DNA constructs and to evaluate the success of reactions between DNA-N_3 and DBCO-functionalized polymer. The native PAGE and agarose gel electrophoresis were performed on DNA constructs after thermal annealing procedure as well as on crude reactions between DNA-N_3 and DBCO-functionalized polymer in 1xTBE buffer at 10°C using Mini-PROTEAN Tetra cell unit (Biorad). PAGE gels were post-stained with GelRed nucleic acid dye (Biotium), while agarose gels were pre-stained with the same dye.

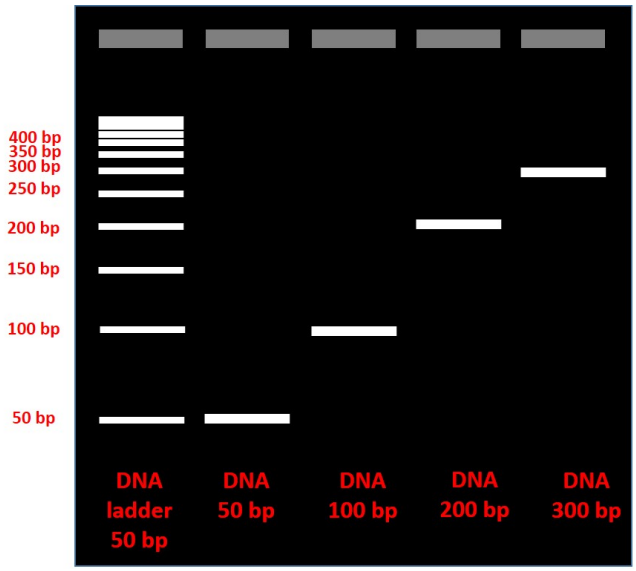

FIGURE 3.8: Schematic representation of a gel used to diferentiate between DNA fragments of different lengths in a typical gel electrophoresis experiment.

3.2 Computer simulations

The most common techniques to study thermodynamic properties of systems of particles are Monte Carlo (MC) and Brownian Dynamics (BD) Simulations [15]. These simulations used to back up the experimental work presented in this thesis. The simulations support experimental results and help to better understand the self-assembly behavior of DNA constructs and the physics behind it. MC simulations were carried out in collaboration with Prof. Christiano de Michele from the University of Rome. The simulations served to back up experimental results and give a more detailed insight into self-assembly of gapped DNA duplexes (chapter 4). BD simulations were performed in collaboration with Institute of Complex Systems (ICS-2), Forschungszentrum Jülich, and were used to obtain a deeper insight into molecular packing within DNA-based cubic network phases in chapter 6.

BD simulation solve Newton's equations of motion for a set of mesoscopic interacting particles. The explicit solvent molecules are replaced by a stochastic force. This way, time trajectories of particles in the simulated system are generated. The trajectories can be visualized and used to measure non-equilibrium properties such as transport coefficients or equilibrium thermodynamic ensemble averages. In contrast to BD simulations, MC simulations propose random moves (translation or rotation) of a particle, which are either rejected or accepted with a given probability p, set in a way that ensures correct sampling from a desired ensemble (typically NPT or NVT).

3.3 Materials and synthesis

3.3.1 Oligomers

Custom oligonucleotides purified by high performance liquid chromatography, were purchased from Biomers. Following oligomers were used:

Gapped DNA duplexes

Fully paired duplex

Strand 1: ACA GAT GCA CAT ATC GAG GTG GAC ATC ACT TAC GCT GAG TAC TTC GAA TTT TTT TTT TTT TTT TTT TTA CAG ATG CAC ATA TCG AGG TGG ACA TCA CTT ACG CTG AGT ACT TCG AA
Strand 2: TTC GAA GTA CTC AGC GTA AGT GAT GTC CAC CTC GAT ATG TGC ATC TGT AAA AAA AAA AAA AAA AAA AAT TCG AAG TAC TCA GCG TAA GTG ATG TCC ACC TCG ATA TGT GCA TCT GT

Gapped 1T duplex

Strand 1: ACA GAT GCA CAT ATC GAG GTG GAC ATC ACT TAC GCT GAG TAC TTC GAA TAC AGA TGC ACA TAT CGA GGT GGA CAT CAC TTA CGC TGA GTA CTT CGA A
Strand 2: TTC GAA GTA CTC AGC GTA AGT GAT GTC CAC CTC GAT ATG TGC ATC TGT
Strand 3: TTC GAA GTA CTC AGC GTA AGT GAT GTC CAC CTC GAT ATG TGC ATC TGT

Gapped 4T duplex

Strand 1: ACA GAT GCA CAT ATC GAG GTG GAC ATC ACT TAC GCT GAG TAC TTC GAA TTT TAC AGA TGC ACA TAT CGA GGT GGA CAT CAC TTA CGC TGA GTA CTT CGA A
Strand 2: TTC GAA GTA CTC AGC GTA AGT GAT GTC CAC CTC GAT ATG TGC ATC TGT
Strand 3: TTC GAA GTA CTC AGC GTA AGT GAT GTC CAC CTC GAT ATG TGC ATC TGT

Gapped 7T duplex

Strand 1: ACA GAT GCA CAT ATC GAG GTG GAC ATC ACT TAC GCT GAG TAC TTC GAA TTT TTT TAC AGA TGC ACA TAT CGA GGT GGA CAT CAC TTA CGC TGA GTA CTT CGA A
Strand 2: TTC GAA GTA CTC AGC GTA AGT GAT GTC CAC CTC GAT ATG TGC ATC TGT
Strand 3: TTC GAA GTA CTC AGC GTA AGT GAT GTC CAC CTC GAT ATG TGC ATC TGT

Gapped 11T duplex

Strand 1: ACA GAT GCA CAT ATC GAG GTG GAC ATC ACT TAC GCT GAG TAC TTC GAA TTT TTT TTT TTA CAG ATG CAC ATA TCG AGG TGG ACA TCA CTT ACG CTG AGT ACT TCG AA
Strand 2: TTC GAA GTA CTC AGC GTA AGT GAT GTC CAC CTC GAT ATG TGC ATC TGT
Strand 3: TTC GAA GTA CTC AGC GTA AGT GAT GTC CAC CTC GAT ATG TGC ATC TGT

Gapped 12T duplex

Strand 1: ACA GAT GCA CAT ATC GAG GTG GAC ATC ACT TAC GCT GAG TAC TTC GAA TTT TTT TTT TTT ACA GAT GCA CAT ATC GAG GTG GAC ATC ACT TAC GCT GAG TAC TTC GAA
Strand 2: TTC GAA GTA CTC AGC GTA AGT GAT GTC CAC CTC GAT ATG TGC ATC TGT
Strand 3: TTC GAA GTA CTC AGC GTA AGT GAT GTC CAC CTC GAT ATG TGC ATC TGT

Gapped 20T duplex

Strand 1: ACA GAT GCA CAT ATC GAG GTG GAC ATC ACT TAC GCT GAG TAC TTC GAA TTT TTT TTT TTT TTT TTT TTA CAG ATG CAC ATA TCG AGG TGG ACA TCA CTT ACG CTG AGT ACT TCG AA
Strand 2: TTC GAA GTA CTC AGC GTA AGT GAT GTC CAC CTC GAT ATG TGC ATC TGT
Strand 3: TTC GAA GTA CTC AGC GTA AGT GAT GTC CAC CTC GAT ATG TGC ATC TGT

Gapped 30T duplex

Strand 1: ACA GAT GCA CAT ATC GAG GTG GAC ATC ACT TAC GCT GAG TAC TTC GAA TTT TTT TTT TTT TTT TTT TTT TTT TTT TTT ACA GAT GCA CAT ATC GAG GTG GAC ATC ACT TAC GCT GAG TAC TTC GAA
Strand 2: TTC GAA GTA CTC AGC GTA AGT GAT GTC CAC CTC GAT ATG TGC ATC TGT
Strand 3: TTC GAA GTA CTC AGC GTA AGT GAT GTC CAC CTC GAT ATG TGC ATC TGT

Gapped 40T duplex

Strand 1: ACA GAT GCA CAT ATC GAG GTG GAC ATC ACT TAC GCT GAG TAC TTC GAA TTT TTT TTT TTT TTT TTT TTT TTT TTT TTT TTT TTT TTT TAC AGA TGC ACA TAT CGA GGT GGA CAT CAC TTA CGC TGA GTA CTT CGA A
Strand 2: TTC GAA GTA CTC AGC GTA AGT GAT GTC CAC CTC GAT ATG TGC ATC TGT
Strand 3: TTC GAA GTA CTC AGC GTA AGT GAT GTC CAC CTC GAT ATG TGC ATC TGT

Gapped 20T duplex with polyT overhangs

Strand 1: TTT TTT ACA GAT GCA CAT ATC GAG GTG GAC ATC ACT TAC GCT GAG TAC TTC GAA TTT TTT TTT TTT TTT TTT TTA CAG ATG CAC ATA TCG AGG TGG ACA TCA CTT ACG CTG AGT ACT TCG AAT TTT TT
Strand 2: TTC GAA GTA CTC AGC GTA AGT GAT GTC CAC CTC GAT ATG TGC ATC TGT
Strand 3: TTC GAA GTA CTC AGC GTA AGT GAT GTC CAC CTC GAT ATG TGC ATC TGT

Hairpin DNA

DNA with blunt ends

Strand 1: ACA GAT GCA CAT ATC GAG GTG GAC ATC ACT TAC GCT GAG TAC TTC GAA
Strand 2: TTC GAA GTA CTC AGC GTA AGT GAT GTC CAC CTC GAC ATG TGC ATC TGT

One hairpin DNA

Strand 1: ACA GAT GCA CAT ATC GAG GTG GAC ATC ACT TAC GCT GAG TAC TTC GAA TTT TTT TCG AAG TAC TCA GCG TAA GTG ATG TCC ACC TCG ACA TGT GCA TCT GT

Two hairpins DNA

Strand 1: GTC CAC CTC GAC ATG TGC ATC TGT TTT TTA CAG ATG CAC ATA TCG AGG TGG ACA TCA CTT ACG CTG AGT ACT TCG AAT TTT TTT TCG AAG TAC TCA GCG TAA GTG AT

One hairpin DNA with G-C termination

Strand 1: GCA GAT GCA CAT ATC GAG GTG GAC ATC ACT TAC GCT GAG TAC TTC GAA TTT TTT TCG AAG TAC TCA GCG TAA GTG ATG TCC ACC TCG ACA TGT GCA TCT GC

DNA-polymer hybrids

Linear DNA-polymer construct

Strand 1: N_3- (T6) ACA GAT GCA CAT ATC GAG GTG GAC ATC ACT TAC GCT GAG TAC TTC GAA
Strand 2: N_3- (T6) TTC GAA GTA CTC AGC GTA AGT GAT GTC CAC CTC GAT ATG TGC ATC TGT

Pi-shaped DNA-polymer construct

Strand 1: ACA GAT GCA CA T(N_3) ATC GAG GTG GAC ATC ACT TAC GCT GAG TAC TTC GAA
Strand 2: TTC GAA GTA C T(N_3) C AGC GTA AGT GAT GTC CAC CTC GAT ATG TGC ATC TGT

Y-shaped DNA-polymer construct

Strand 1: N_3- (T6) TGA CTG GAT CCG CAT GAC ATT CGC CGT AAG
Strand 2: N_3- (T6) TGA CCT TAC GGC GAA TGA CCG AAT CAG CCT
Strand 3: N_3- (T6) TGA CAG GCT GAT TCG GTT CAT GCG GAT CCA

3.3.2 Other materials

- 1xTE buffer (10 mM Tris pH 7.5, 0.1 mM EDTA, Integrated DNA technologies)
- 1xTE/NaCl buffer (10 mM Tris pH 7.5, 0.1 mM EDTA, 150 mM NaCl)
- 1xTE/1M NaCl buffer (10 mM Tris pH 7.5, 0.1 mM EDTA, 1M NaCl)
- 1xTBE buffer (90 mM Tris-Borate, 2 mM EDTA, pH= 8.3, Merck)
- 20% Ethanol
- 6X DNA gel loading buffer (OXG) (Affymetrix)
- 10000X GelRed gel stain (Biotium)
- 3300X GelRed in water post staining solution
- Amine terminated PNIPAm (Polymer Source and Specific Polymers with *nominal* molecular weights of 20 kDa and 1.7 kDa respectively)
- DBCO-PEG_4-NHS ester (Jena BioScience)
- N, N- Dimethylformamide (DMF) (Sigma Aldrich)
- Milipore Amicon filters, MWCO 3k (Sigma Aldrich)
- Columns for chromatography HiPrep DEAE Fast Flow 16/10 (GE Healthcare Life Sciences)
- SnakeSkin dialysis tubes (Thermofisher)

3.3.3 Synthesis

All oligonucleotides were dispersed in 1xTE buffer. The concentration of DNA was determined by measuring absorbance at 260 nm using micro-volume spectrometer NanoDrop 2000.

Gapped DNA constructs

Gapped DNA (G-DNA) duplexes were assembled by mixing stoichiometric amounts of three single strands involved in the formation of final G-DNA structures. For each G-DNA construct, one long single strand is used and another two shorter strands that are complementary to the parts of the long one. This way we can obtain two double-stranded regions between which a flexible *gap* is left, being a part of the long strand for which no complementary strand is present. With the described synthetic approach, it is possible to control the length of the flexible spacer, as well as its position, both with sub-nanometer precision, at level of a single base pair. Strands were assembled into a target structure through the standard thermal annealing protocol. According to the protocol, samples were dispersed in 1xTE/NaCl buffer, put into a 10 L hot water bath, in a previously heated oven at 95 °C and left in a Styrofoam box to slowly cool down and hybridize during 48 h. After thermal annealing, the success of this procedure was evaluated using native PAGE gel electrophoresis described earlier in this chapter, in the section 3.1.4.

Hairpin DNA constructs

Hairpin DNA (H-DNA) constructs were formed by self-folding of one single strand with palindromic sequence, in a standard annealing protocol already described in the previous paragraph. With this synthetic approach, H-DNA constructs which posses hairpin structure at one or both ends of the duplex are made. The hairpin serves as *self-protection* of terminal bases that would otherwise be exposed to the environment. The integrity of the formed constructs was checked using native PAGE gel electrophoresis (see section 3.1.4), after thermal annealing.

DNA-polymer hybrids

The synthesis of DNA-polymer hybrids includes multiple steps, starting with standard annealing protocol of two single strands, one of which is azide-modified, in order to obtain a double-stranded rod-like DNA which serves as a base for the further attachment of the polymeric segment.

Polymer functionalization Amine terminated polymers were functionalized with DBCO-PEG_4-NHS ester that was purchased from Jena Bioscience. All reagents were used with no further purification. To functionalize polymers with DBCO group, both PNIPAm and DBCO-PEG_4-NHS reagent were dissolved in DMF and mixed in ratio PNIPAm:DBCO- PEG_4-NHS = 1:7. The reaction was left to proceed at room temperature during 72h. Afterwards, the mixture was diluted ten times and dialyzed against water using SnakeSkin dialysis tubes (Thermo Scientific) to remove the unreacted DBCO-PEG_4-NHS molecules. Finally, the purified polymer solution was stored at -70°C overnight and freeze-dried. The success of the functionalization was confirmed by the change in UV-vis absorbance at 311 nm.

Click chemistry In order to covalently attach polymer to DNA, copper-free Strain-Promoted Azide-Alkyne Click Chemistry reaction was used [16]. Prior to reaction, both azide-functionalized DNA (DNA-N_3) and DBCO-functionalized polymer were dissolved in 1xTE/Nal buffer and homogenized. The optimal ratio of reacting components was determined in a series of test reactions in which DNA-N_3 and polymer were mixed in ratios 1:1, 1:2, 1:3, 1:5, 1:7, and 1:10. The ratio at which no evidence of unreacted DNA-N_3 was found by gel electrophoresis was chosen as the optimal ratio. In a typical reaction, DNA-N_3 and polymer were mixed in ratios 1:5. The reactions were incubated at 20°C during 48h after which the reaction solutions were purified to remove the excess polymer. The success of the reaction was checked using agarose gel electrophoresis, as described earlier in the section 3.1.4.

Purification The excess of polymer was removed and the final product of the reaction was purified using affinity chromatography columns HiPrep DEAE Fast Flow 16/10 (GE Healthcare Life Sciences). The column was operated using syringe-assisted pump (KDS 100, kdScientific) at room temperature. To remove the preservatives, the purification column was first washed out with 100 ml of start buffer (1 x TE buffer), followed by 100 ml of elution buffer (1xTE/1M NaCl) and finally equilibrated with 200 ml of start buffer. The reaction mixture was diluted with 20 ml of TE buffer, pumped onto the column at flow rate 5 ml/min, and stored in the fridge overnight. Afterwards, the excess of DBCO-functionalized polymer was washed out of the column with 200 ml of start buffer. The DNA-polymer constructs were then collected

by washing out the column using elution buffer until no material appeared in the eluent. The presence of DNA in the eluent was continuously checked by measuring the absorbance at 260 nm using NanoDrop2000.

3.3.4 Sample preparation

The samples were concentrated and the buffer was exchanged, both using Amicon (MWCO 3k) filters. Afterwards, Eppendorf SpeedVac Concentrator was used to reach the highest concentration. The final suspensions for measurements were prepared by step-wise dilution of the most concentrated sample with 1xTE/NaCl buffer solution. In every dilution step the sample was thoroughly homogenized before loading into capillaries for SAXS experiments.

Bibliography

[1] M. E. Cates and M. R. Evans. *Soft and fragile matter*. The Scottish Universities Summer School in Physics and Institute of Physics Publishing, Bristol and Philadelphia, 1999.

[2] THE FIT2D HOME PAGE, 2018. URL http://www.esrf.eu/computing/scientific/FIT2D/.

[3] W. H. de Jeu. *Basic x-ray scattering for soft matter*. Oxford University Press, 1st edition, 2016.

[4] J. D. Watson and F. H. Crick. Molecular Structure of Nucleic Acids: A Structure for Deoxyribose Nucleic Acid. *Nature*, 171:737–738, 1953.

[5] E. Kentzinger, M. Krutyeva, and U. Rücker. GALAXI: Gallium anode low-angle x-ray instrument. *Journal of large-scale research facilities*, 2:A61, 2016.

[6] How does the ESRF work, 2018. URL http://www.esrf.eu/home/education/what-is-the-esrf/how-does-the-esrf-work.html.

[7] W. Bras. Recent experiments on a small-angle/wide-angle x-ray scattering beam line at the ESRF. *Journal of Applied Crystallography*, 36:791–794, 2003.

[8] H. Schnablegger and Y. Singh. *The SAXS Guide*. Anton Paar GmbH, 2017.

[9] Jan P. F. Lagerwall. *Structures and properties of the chiral smectic C liquid crystal phases*. Chalmers University of Technology, Göteborg, 2002.

[10] G. Maret and K. Dransfeld. Biomolecules and Polymers in High Steady Magnetic Fields. In *Strong and Ultrastrong Magnetic Fields and Their Applications. Topics in Applied Physics*. Springer, Berlin, Heidelberg, 1985.

[11] V. Brabec, V. Kleinwaechter, and V. Vetterl. Structure, chemical reactivity and electromagnetic properties of nucleic acids. In G. Lenaz and G. Milazzo, editors, *Bioelectrochemistry of biomacromolecules*, pages 1–104. Birkhaeuser, 1997.

[12] Ingo Dierking. *Textures of liquid crystals*. Wiley-VCH, Weinheim, 2003.

[13] Nikon- Polarized Light Microscopy, 2019. URL https://www.microscopyu.com/techniques/polarized-light/polarized-light-microscopy.

[14] J. Sambrook and D. W. Russell. *Molecular cloning*. Cold Spring Harbor Laboratory Press, Cold Spring Harbor, New York, third edit edition, 2001.

[15] D. Frenkel and B. Smit. *Understanding Molecular Simulations: From Algorithms to Applications*. Academic Press, Inc., 2006.

[16] N. J. Agard, J. A. Prescher, and C. R. Bertozzi. A strain-promoted [3 + 2] azide-alkyne cycloaddition for covalent modification of biomolecules in living systems. *Journal of the American Chemical Society*, 126:15046–15047, 2004.

Chapter 4

Self-assembly of gapped DNA duplexes

All-DNA nanostructures called gapped DNA (G-DNA) duplexes and their self-assembly behavior will be presented in this chapter. DNA's unique physicochemical properties and the difference in persistence length between single-stranded and double-stranded DNA allow us to construct nanostructures with chain-stick architecture. Concentrated aqueous solutions of G-DNA duplexes exhibit an intriguing phase behavior. In particular, the formation of an unconventional smectic A-type of phase is found, in which G-DNA duplexes are in a folded conformation within the layer-like mesophase. Therefore, this phase is referred to as folded smectic A (Sm-fA) phase. The key interactions driving the formation of this unconventional phase will be presented together with the impact of the flexible spacer length on the phase behavior of G-DNA duplexes. Additionally, the role of end-to-end stacking interactions in the stabilization of the smectic phase in such systems will be demonstrated.

4.1 Introduction

The main characters in this chapter are gapped DNA (G-DNA) duplexes. These novel DNA nanostructures shine a light on DNA as a molecular tool with numerous possibilities for engineering of LC phases. Whilst still consisting of the DNA only, G-DNA duplexes exhibit the intra-molecular flexibility difference which is introduced to the system in the form of a single-stranded DNA (ssDNA) flexible spacer. The gap is positioned between two short stiff double-stranded DNA (dsDNA) fragments of equal lengths terminated with blunt ends, which is schematically depicted in the top panel of figure 4.1. The difference in flexibility between flexible gap and double-stranded region arises from the fact that the basic mechanical properties related to the stiffness of ssDNA and dsDNA are remarkably different. Persistence length of a dsDNA is around 50 nm, which equals to around 150 base pairs (bp) assuming 0.34 nm per bp [1, 2], while this value for ssDNA is around 2 nm or close to 2 bases (assuming 0.64 nm per base) [3]. The chosen 48 bp long ($\sim$ 16 nm) dsDNA blocks are stiff and are connected with a central ssDNA spacer. The flexible spacer is a sequence of unpaired thymine (T) bases, which are chosen due to their lack of tendency to form secondary structures. As we will demonstrate later on, the flexibility dissimilarities between blocks in the G-DNA duplexes result in a very different phase behavior in comparison to their fully paired analogs (the bottom panel in figure 4.1).

The G-DNA duplexes are synthesized by one-pot self-assembly of three synthetic ssDNA; one longer ssDNA and two shorter that are complementary to the parts

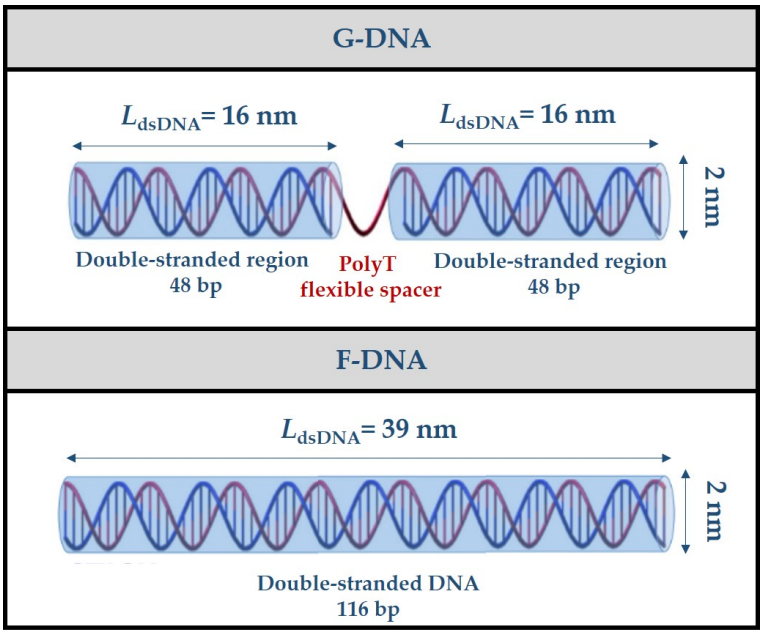

FIGURE 4.1: Schematic representation of the gapped DNA (G-DNA) duplex structure, consisting of two double-stranded regions connected with a flexible single-stranded spacer (the top panel), and its fully-paired analogue (F-DNA) (the bottom panel). The typical length scales in these structures are also depicted.

of the longer strand. Thanks to the phosphoramidite-based solid phase synthesis,[1] the flexible spacer can be positioned at desired places in the DNA duplex and have different lengths. These modifications can be introduced with sub-nanometer precision, at the level of a single base. Therefore, it is possible to synthesize a wide variety of gapped DNA duplexes and see how, for instance, different length of flexible spacer influences their self-assembly behavior. The protocol is described in more details in chapter 3, section 3.3.3. To confirm the successful assembly of G-DNA duplexes, native PAGE electrophoresis was employed. Electrophoretic mobilities of three different DNA duplexes are given in the figure 4.2: G-DNA with a flexible spacer of 1 T base (G-1T-DNA) and 20 T bases (G-20T-DNA), and the fully paired analog of G-20T-DNA duplex which is referred to as F-DNA. As shown in the figure, the assembled G-DNA duplexes migrate as sharp single bands, showing a delay in migration with the increase of the flexible spacer length. There is a minor difference in migration between the ladder band corresponding to 100 bp DNA and G-1T-DNA with length of 97 bp located in the second lane, due to the length similarity of two duplexes. The band in the third lane corresponding to the G-20T-DNA shows a significant delay in migration, comparing to its fully paired analogue in the first lane. This is observed because the G-DNA duplex is slowed down by a flexible single-stranded region in the middle of it. Using native PAGE electrophoresis it is possible to clearly separate G-DNA duplexes with flexible spacers of different lengths.

The absence of smectic (*Sm*) phase in DNA liquid crystals (LC) is still a controversial issue. So far, no *Sm* phase was found in DNA duplexes of any length [4, 5, 6, 7, 8, 9]. Here, it will be shown that by introducing a ssDNA flexible spacer

[1] Marvin Caruthers introduced the phosphoramidite-based solid phase synthesis of oligomers in 1980. He applied a newly developed method for obtaining peptides and proteins of R. Bruce Merrifield. In 1984 Merrifield was awarded a Nobel prize in Chemistry for this achievement.

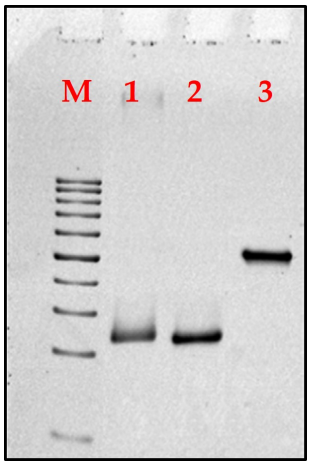

FIGURE 4.2: 10% native PAGE electrophoresis of G-DNA. Lanes contain following samples: **M)** 50 bp DNA ladder, each band represents DNA fragment starting from 50 bp at the bottom to 500 bp at the top, with 50 bp steps, **1)** Fully paired DNA duplex, L_{dsDNA} = 116 bp, **2)** Gapped DNA duplex with 1T flexible spacer, **3)** Gapped DNA duplex with 20T flexible spacer.

to the middle of a stiff double-stranded DNA duplex it is possible to form *Sm* phase. This chapter contains also previously published work[10] for which the experiments were conducted at the Institute of Complex Systems (ICS-3) in Forschungszentrum Jülich. Therefore, in order to present results obtained as part of this thesis in a more coherent way, they will be discussed in a broader context containing the results of the previous work.

4.2 Smectic phase in suspensions of G-20T-DNA duplexes

Small-angle X-ray scattering (SAXS) and polarized optical microscopy (POM) were used to systematically investigate a phase behavior of both F- and G-DNA. Scattering profiles of F-DNA duplexes at different concentrations are shown in figure 4.3. At high concentrations, well above the critical concentration at which LC phases are formed in the system, F-DNA shows one sharp intense peak q_{DNA} at high values of scattering vector q. This sharp peak indicates strong positional order between neighboring parallel DNA helices and is related with the formation of two-dimensionally ordered columnar (*Col*) phase [11]. Decreasing the concentration, q_{DNA} peak shows a slight shift towards lower q values, indicating increased distances between DNA helices in the suspension, and another broader peak arises at around the same q value. At total DNA concentration of 287.4 mg ml^{-1} an overlap between the sharp q_{DNA} and broad peak was observed indicating a liquid-like ordering and a possible phase coexistence of *Col* and chiral nematic or cholesteric (*N**) LC phase, an evidence of which will be demonstrated and discussed below.

Further decrease of the total DNA concentration to 247.2 mg ml^{-1} leads to a complete disappearance of the sharp peak. The broad peak broadens even more and shifts to lower q values. The sample under crossed polarizers appears birefringent and the POM reveals the typical fingerprint texture which confirms the formation of N* phase. The sample at even lower concentrations, observed under crossed polarizers, shows the two-phase coexistence. Although there is no difference in SAXS

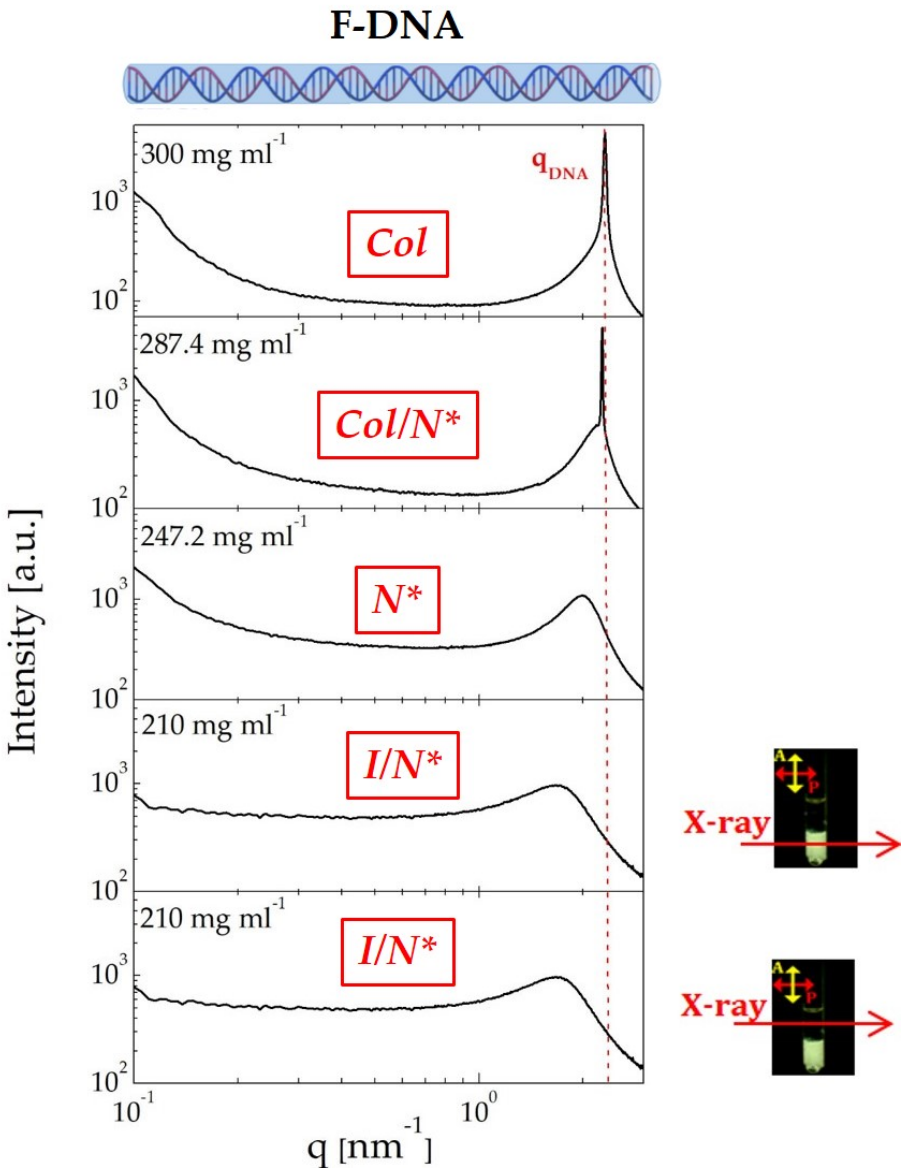

FIGURE 4.3: X-ray scattering profiles of F-DNA duplexes at concentrations (from top to the bottom) c = 300, 287.4, 247.2, and 210 (the lowest two panels) mg ml^{-1}. On the right-hand side are samples observed under crossed polarizers. The red arrow indicates part of the sample probed by the x-ray beam.

profiles between I and N^* phase, the upper part of the sample remains dark under crossed polarizers while the lower part is still birefringent, as shown in the figure 4.3. Therefore, at 210 mg ml^{-1} we observe a phase coexistence between birefringent N^* and isotropic (I) state. Finally, below 210 mg ml^{-1} F-DNA undergoes a phase transition to an orientationally disordered I state, which is evident from the lack of birefringence in the sample.

The absence of the *Sm* phase in F-DNA can be attributed to weak non-covalent attractive end-to-end stacking interactions. In 2007, self-assembly of very short blunt-ended DNA duplexes with lengths between 6 ($\sim$ 2 nm) and 20 bp ($\sim$ 6.8 nm) was investigated [9]. Despite the fact that simulations on hard spherocylinders with similar aspect ratios L/D (where L is the length of the rod, and D is its diameter) showed no LC ordering [12, 13], experiments revealed the formation of LC phases. Therefore, the hypothesis was raised stating that attractive end-to-end stacking interactions between blunt ends of dsDNA were crucial for the formation of linear flexible aggregates (discussed in detail in chapter 2.3.1). These aggregates have L/D sufficiently high for the formation LC phases. Note that end-to-end stacking interactions are inherently present in blunt-ended dsDNA, regardless of its length. In case of F-DNA, these interactions allow the DNA duplexes to stack on top of one another and form polydisperse aggregates for which smectic ordering is unfavorable. As already discussed in the section 2.3, polydispersity plays an important role in stabilization of LC phases in DNA [14]. Monodisperse rod-like systems with high L/D stabilize *Sm* phase, while for the polydisperse ones this phase is absent and replaced by *Col* phase transition. For this work, synthetic oligomers were used for the fabrication so that G-DNA duplexes formed are strictly monodisperse. The DNA duplexes presented in this work are monodisperse and stiff (their contour length L being smaller than their persistence length L_p, ($L/L_p \approx 0.77$). Therefore, it is reasonable to claim that the *Sm* phase in F-DNA is not absent neither due to the length polydispersity of individual DNA duplexes nor due to their flexibility. However, length polydispersity plays a role in case of F-DNA, but only in terms of aggregates formed by end-to-end stacking. Polydisperse linear aggregates prefer to order themselves in a columnar fashion rather than in a layer-like structure.

The scattering profiles of G-20T-DNA in figure 4.4 shows remarkably different phase behavior compared to F-DNA. At approximately the same total DNA concentration at which F-DNA forms *Col* phase, G-20T-DNA duplexes show additional sharp principal peak followed by higher order reflections at lower q values (top panel in the figure 4.4, c= 291.2 mg ml^{-1}). These equidistant peaks are signature of the *Sm* phase. From the position of the primary peak q^* we can calculate spacing between adjacent layers of a layered structure as $d = 2\pi/q^* = 34$ nm. The value of 34 nm is very close to the length of one G-DNA duplex, assuming that the flexible spacer is almost completely collapsed. Thus, the total spacing length is approximately equal to the sum of lengths of two dsDNA segments. A small shift of the principle peak towards higher q values suggests a weak concentration dependence of the q^* peak and increase of the smectic spacing from 33.4 to 35.7 nm as we increase the total DNA concentration from 231.8 to 291.2 mg ml^{-1}. Sharp q_{DNA} peak suggests that the mesophase formed possesses strong positional order within layers. At slightly lower concentration smectic peaks are still observed, while the q_{DNA} peak broadens out due to a liquid-like order in the positions of duplexes. As we reach even lower concentrations, G-20T-DNA undergoes a phase transition to N^* and finally, through the I/N^* phase coexistence (at 219.5 and 203.5 mg ml^{-1}), to I phase (below 203.5 mg ml^{-1}). The I/N^* phase coexistence can be observed under crossed polarizers. This can be seen in the two bottom sample images on the right hand side in the figure 4.4.

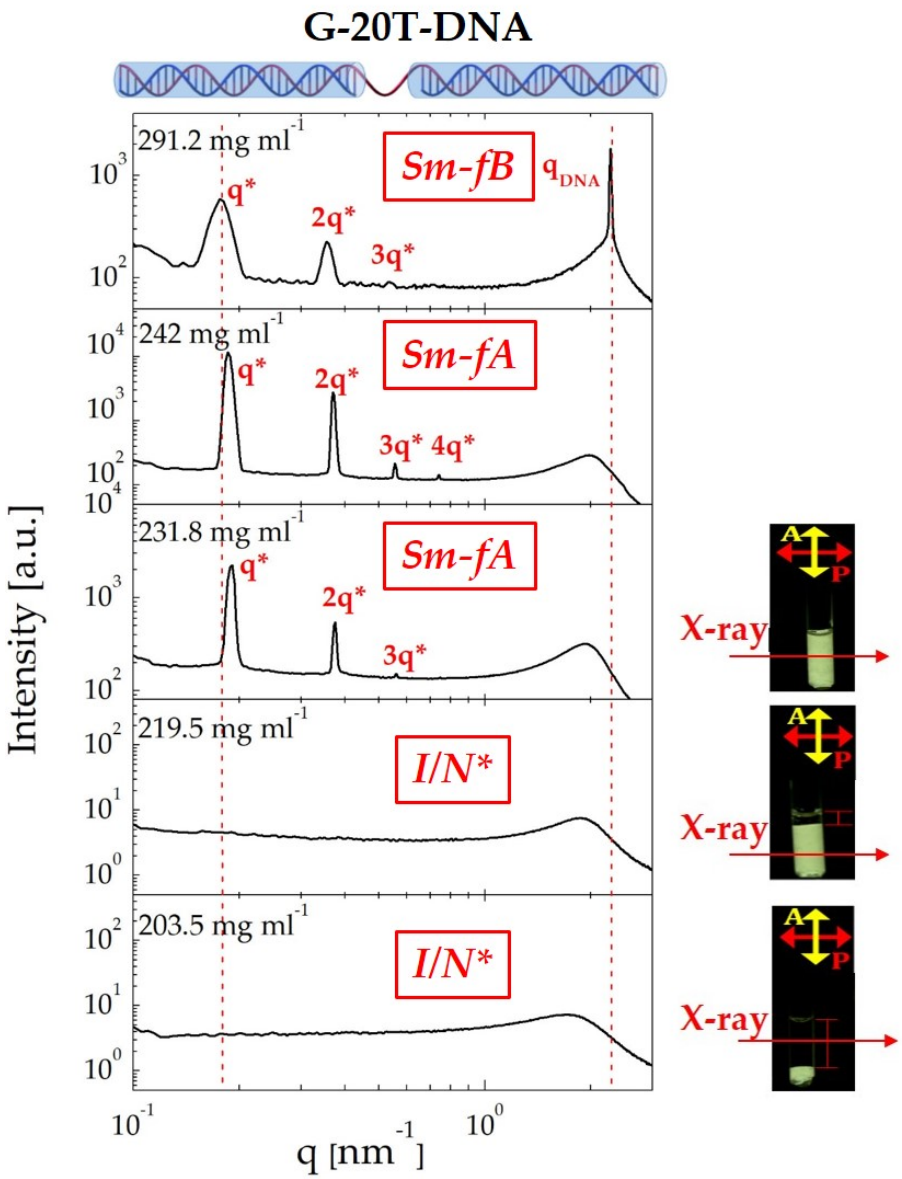

FIGURE 4.4: X-ray scattering profiles of G-20T-DNA duplexes at concentrations (from top to the bottom) c = 291.2, 242, 231.8, 219.5, and 203.5 mg ml^{-1}. On the right-hand side are samples observed under crossed polarizers. The red arrow indicates part of the sample probed by the x-ray beam.

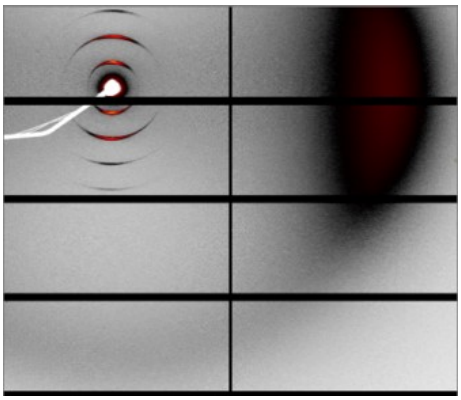

FIGURE 4.5: Two-dimensional SAXS pattern of a smectic A phase in a shear-aligned suspension of G-20T-DNA duplex at total DNA concentration of c= 242.0 mg ml^{-1}.

There are two regions in the sample; the bottom one is birefringent (N^*), while the upper one appears dark (I). At total DNA concentration of 219.5 mg ml^{-1} and 203.5 mg ml^{-1}, the SAXS beam probed the birefringent and the non-birefringent part of the sample, respectively.

The arrangement of the molecules within the smectic layers can be determined by observing 2D scattering pattern of a shear-aligned sample (figure 4.5). Shear was applied during the sample loading by centrifuging the sample along the walls of the capillary. The arcs close to the beam stop correspond to smectic peaks and originate from the layer-like morphology of the structure. The arcs found in the outer region of the pattern correspond to the q_{DNA} peak and originate from positional correlations in duplex diameter. The two sets of arcs are in a perpendicular orientation relative to one another. This suggests that G-20T-DNA duplexes are arranged in smectic A (*Sm-A*) phase in which duplexes within layers are perpendicular to the layer normal. At the highest DNA concentration (the top panel in figure 4.4) the sharp q_{DNA} peak indicates long range positional order within the smectic layers. This strongly suggests the formation of smectic-B phase (*Sm-B*), where molecules are ordered not only in a layer-like structure, but additionally posses hexagonal order within the layers. Broadening of the smectic peaks at the highest total DNA concentration shown in the top panel of figure 4.4) is due to the soft loading of the sample into capillaries[2]. This way, we avoid the exposure of the sample to high centrifugation forces and thereby exclude the possibility for the formation of shear-induced structures.

An alternative way to align the sample is by magnetic field. Due to its negative diamagnetic anisotropy, DNA tends to orient its long axis perpendicular to the direction of applied magnetic field B [15]. This property of DNA was already described in detail in section 3.1.2. One would expect that in the scattering pattern of magnetically aligned DNA forming *Sm-A* phase peaks originating from layered structure would be found exactly perpendicularly to the direction of B. This can be clearly seen in the scattering pattern for G-20T-DNA duplex at total DNA concentration of 255.0 mg ml^{-1} exposed to magnetic field of 14 Tesla for 48 hours shown in figure 4.6.

[2]For highly viscous samples, the loading procedure unavoidably causes shear-alignment. This may result in non-equilibrium shear-induces structures. Therefore, soft loading was performed for the viscous sample at the highest concentrations. This results in smaller coherent domain size, which is witnessed by a reduced number of smectic peaks and their broadening.

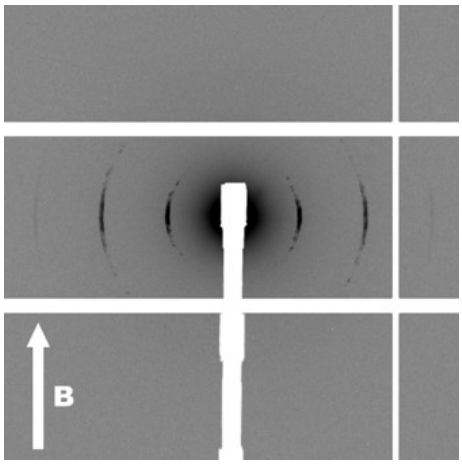

FIGURE 4.6: Two-dimensional SAXS pattern of a smectic A phase in a magnetically aligned suspension of G-20T-DNA at 255.0 mg ml^{-1}.

The finding that incorporation of a flexible spacer into DNA duplex can drive the system towards the formation of *Sm* phase is counterintuitive. The previous experimental work on fd virus [16] and theoretical [17, 18, 19, 20] studies on hard repulsive spherocylinders (L/D is similar to the DNA systems investigated here) have shown that flexibility destabilizes layer-like structure. Hence, it is hard to comprehend how introducing additional flexibility might drive the G-DNA duplexes towards layer-like ordering. Moreover, *Sm* phase is expected to appear in systems of purely repulsive rods with different aspect ratios, such as viral rod-like particles [21] and colloidal silica rods [22], as discussed earlier in the section 2.3. However, no *Sm* phase was observed in dsDNA of any length so far.

Two possible scenarios for the formation of the *Sm* phase in G-20T-DNA duplexes, based on the physical arguments and SAXS data for both F-DNA and G-DNA duplexes will be discussed. The first one is an unfolded scenario schematically shown in figure 4.7 a), in which G-DNA duplexes are in an unfolded layer-like arrangement. However, this scenario is quite unlikely to happen for several reasons. As already mentioned, regardless of the length, F-DNA duplexes do not form the *Sm* phase. Introducing a flexible spacer in the middle of dsDNA would further destabilize the *Sm* phase. Moreover, with such an arrangement, end-to-end stacking would generate polydisperse aggregates that would hinder the smectic ordering, similarly as in case of F-DNA. Finally, in order to fit into a calculated smectic layering of 34 nm, it would be necessary for unfolded G-20T-DNA duplexes to have a flexible spacer collapsed to a large extent. This would be, however, energetically unfavorable from the point of view of flexible spacer conformational entropy.

The more plausible scenario is the folded one shown in figure 4.7 b). Here, every stiff fragment forms one half of the layer, while the flexible spacers are found between layers. This kind of molecular arrangement allows the "self-protection" of the blunt ends of G-DNA duplexes so that, once they stack on top of one another, no further stacking is possible. Thereby, end-to-end attractions make strictly monodisperse pairs of G-20T-DNA and as a consequence uniform layer structure can be formed. The folded layer-like arrangement leads to the stretching of the ssDNA spacer, which consequently decreases the inter-layer spacing. This is in very good agreement with the calculated smectic layering of 34 nm. The entropic cost

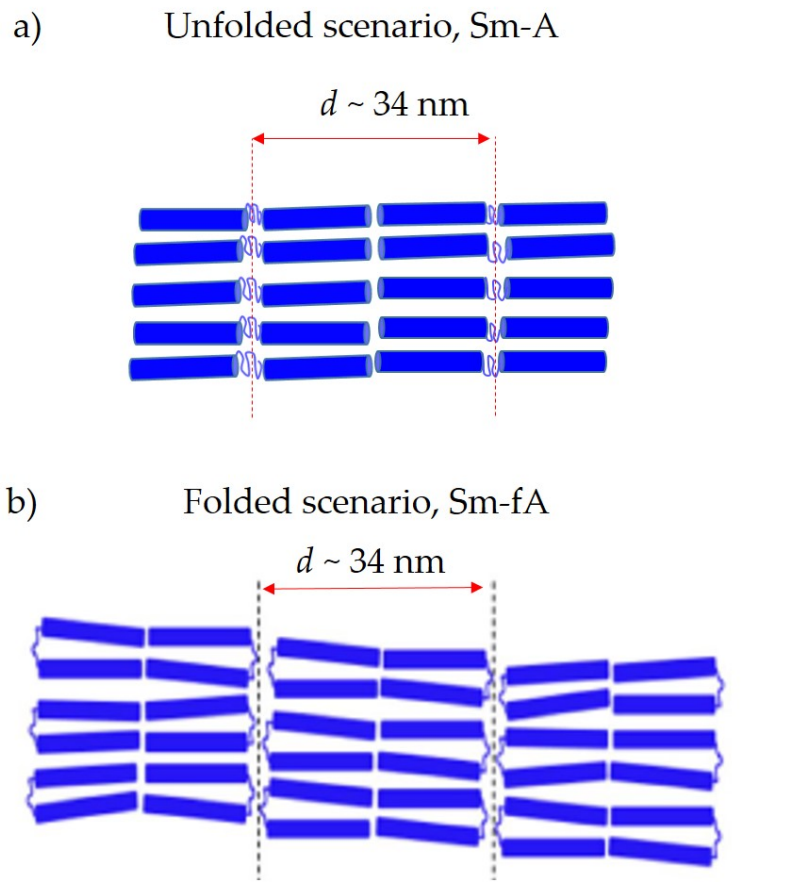

FIGURE 4.7: Schematic representation of two possible molecular arrangements within the smectic-A phase. a) Undfolded scenario in which G-DNA duplexes are in an unfolded layer-like arrangement. b) Folded scenario in which G-DNA duplexes are folded and stacked on top of one another.

related to the stretching of the 20 T flexible spacer is expected to be quite small, considering the ssDNA $L_p \sim$ 3 bases. The unconventional *Sm* phase formed is referred to as folded *Sm-A* phase (*Sm-fA*).

Additional support and demonstration of the flexible spacer importance in the folding scenario come from the G-DNA duplexes with much shorter spacer of only 4T bases (G-4T-DNA). The scattering profile for this system at total DNA concentration of 250.07 mg ml^{-1}, together with the scattering profile of G-20T-DNA at similar concentration (total DNA concentration c= 242 mg ml^{-1}) is shown in figure 4.8. In contrast to G-20T-DNA duplexes, no evidence of smectic layering is found in G-4T-DNA duplex at given concentration. It will be shown in the complete phase diagram (figure 4.17, section 4.4) that no *Sm-fA* phase occurs at any concentration for this system. The absence of smectic peaks at all measured concentrations suggests that the spacer is clearly not sufficiently long to drive this system to formation of a *Sm* phase. Therefore, the *Sm-fA* phase occurs only when there is enough flexibility between the two rod-like segments of G-DNA duplexes.

The concentration-dependent phase behavior of F-DNA and G-20T-DNA is presented in phase diagram in figure 4.9. It is constructed based on the SAXS results

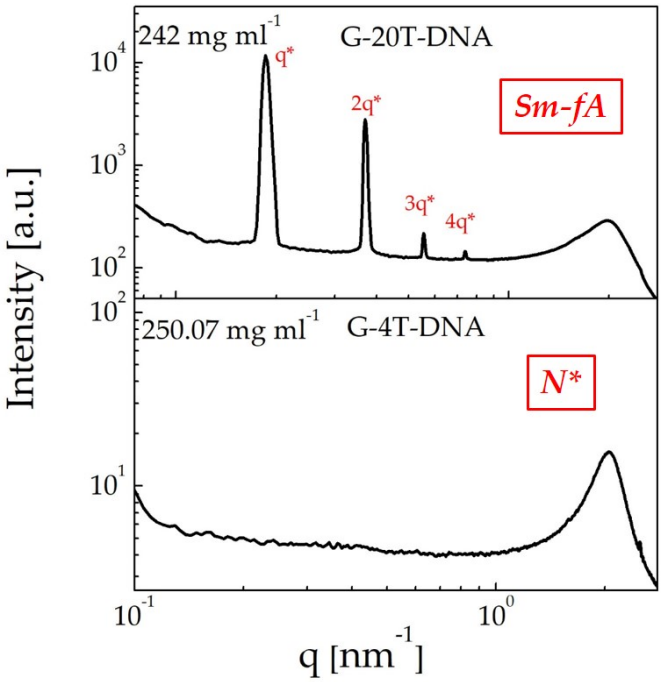

FIGURE 4.8: X-ray scattering profiles of the G-20T-DNA duplexes (c = 242 mg ml^{-1},, the top panel) and G-4T-DNA duplexes (c = 250.07 mg ml^{-1}, the bottom panel).

complemented by selected POM images. The I/LC coexistence regions were determined by visual observation of capillaries under crossed polarizers. The POM image on the left hand side in the phase diagram shows a typical fingerprint texture. This is a direct manifestation of the chirality of the nematic phase formed by F-DNA in the I/N^* coexistence region, as well as at concentration above it. The extracted value of the cholesteric pitch is around 2.15 μm, which is in good agreement with previously obtained values for dsDNA of similar length [23]. Isolated dislocations can be observed in the N^* phase of F-DNA. This is indicated in the white circles in the POM image in the figure 4.9. The two bottom micrographs for the G-20T-DNA show the typical fingerprint texture for LC sample just above the I/N^* coexistence region, suggesting that the concentration range at which N^* forms is rather narrow. The cholesteric pitch of G-20T-DNA is only 1.15 μm, which is significantly smaller than the one of F-DNA. In contrast to F-DNA, a fan-shaped fingerprint texture with dislocations can be seen in the middle micrograph. The POM image at higher concentration (the top micrograph in figure 4.9) shows the fan texture typical for smectic phases, with no fingerprint bands visible.

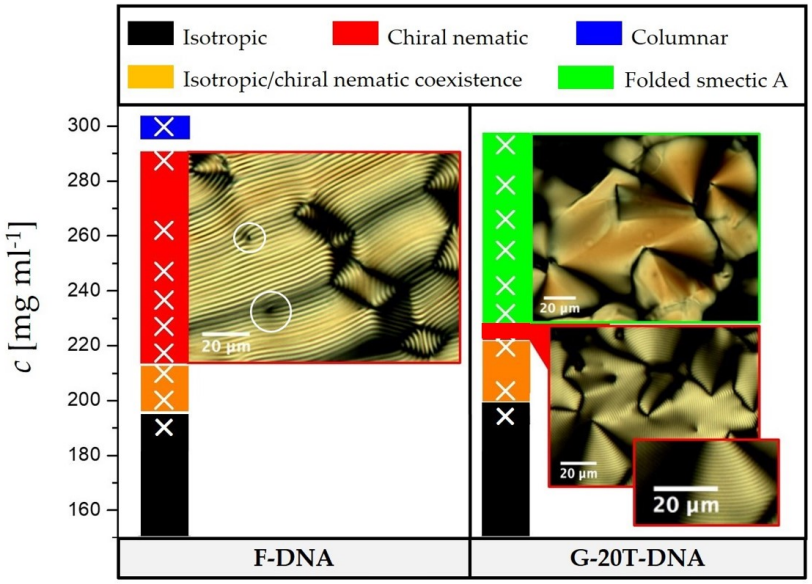

FIGURE 4.9: Phase diagram obtained by combination of SAXS measurements, visual observation of capillaries under crossed polarizers, and polarization optical microscopy on selected samples, comparing F-DNA and G-20T-DNA. White crosses mark the concentrations of samples measured by SAXS. The micrograph showing the F-DNA sample reveals the cholesteric phase just above the two-phase coexistence region. Two lower micropgraphs on the right hand side belong to the same suspension of G-20T-DNA duplexes. The bottom one is a magnification of the lower left region in the larger image, showing the typical fingerprint texture characteristic for the cholesteric phase. The top micrograph for the G-20T-DNA shows the fan texture of the smectic phase formed close to the lowest concentration at which smectic phase appears. The micrograph is taken close to the lower concentration boundary of *Sm-fA* phase.

4.2.1 Monte Carlo simulations

The suggested folding scenario was backed up by Monte Carlo (MC) simulations performed in collaboration with Prof. Christiano De Michele from the Sapienza University of Rome.

In the simulation, the G-20T-DNA duplexes are modeled as two cylinders with length L= 16 nm. Due to electrostatic repulsion, the diameters of cylinders are chosen to be larger than the steric diameter of DNA, which is around 2 nm. The value for diameter D= 3 nm is taken based on effective diameter estimation reported in the literature [24, 25]. Each model cylinder has two interaction sites: A and B, as shown in the figure 4.10, with diameters δ and σ, respectively. Interaction points B hold two cylinders together by a permanent bond and model the flexible spacer, while A points serve to model hydrophobic attraction in the terminal ends, i.e. end-to-end stacking interactions. Sites A of two distinct cylinders interact via square well potential βu_{sw}, which is βu_{sw}= βu_0 if $r < \delta$, and βu_{sw}= 0 if $r > \delta$, $\beta = k_B T$, r is the distance between interaction sites, and δ is the interaction range (the diameter of the interaction point A). The interaction range σ is taken equal to the half of the contour length of the flexible 20 T spacer (∼12.6 nm). The geometry of the attractive sites A was adopted from the previously published work by K. Nguyen *et al.* [26]. This model was already successfully applied for investigation of phase behavior of ultra short dsDNA [27, 9].

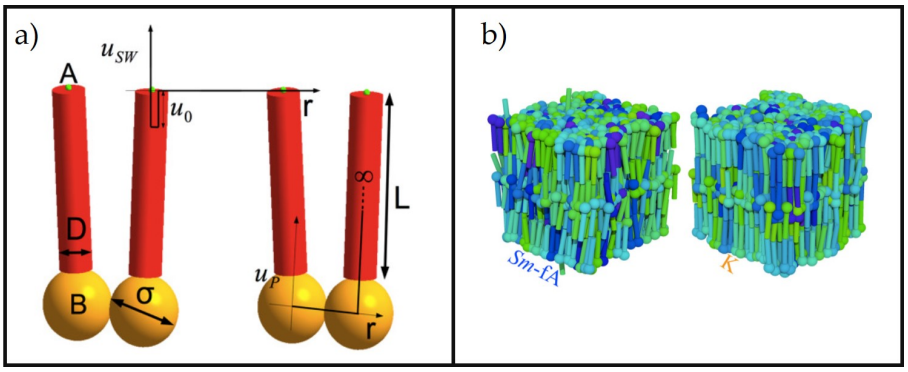

FIGURE 4.10: a) Coarse-grained model of G-DNA duplexes used in Monte Carlo simulations, and b) Snapshots of folded smectic A and crystalline phase. Cylinders belonging to the same gapped DNA duplex are shown in the same color, so that the amount of folded duplexes can be seen, adapted from [10].

The phase behavior of G-20T-DNA duplexes was studied by calculating equation of state and 3D pair distribution functions [27]. The equation of state for attraction strength between hydrophobic patches βu_0= 8.06 is shown in the figure 4.11. The inset shows the 2D pair distribution function for βv_0= 4.1 (where v_0 is volume of a single cylinder) which corresponds to correlations parallel to the nematic director (z-axis). The equation of state shows a first-order transition from I to LC state, which can be seen from the break in the βv_0 vs concentration plot. The pair distribution function reveals the formation of layered structure, which can be identified as *Sm-A* phase.

Quantified insight into packing of the model G-DNA duplexes in the *Sm* phase is achieved by studying the fraction of folded G-DNA duplexes n_f. The fraction n_f is defined as n_f= N_f^{45}/N, where N_f^{45} represents the average number of gapped

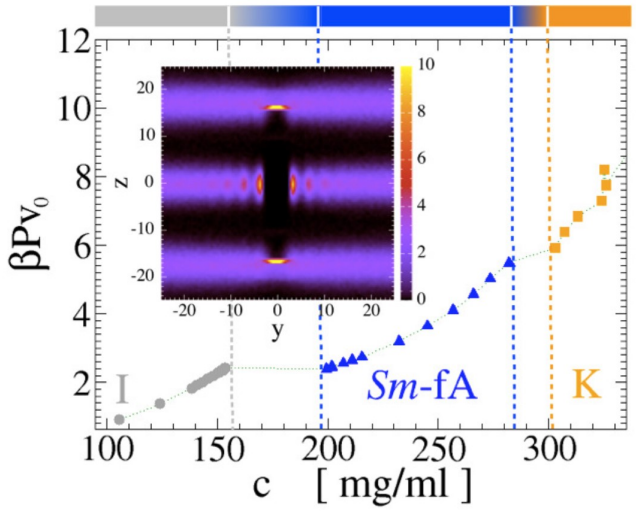

FIGURE 4.11: Equation of state for G-20T-DNA duplex obtained from simulations; inset shows pair distribution function for folded smectic A phase corresponding to $\beta P v_0 = 4.1$, on a plane parallel to the nematic director (z-axis), from [10]

duplexes with a folding angle $\theta_f < 45°$. The angle $\theta_f = 0$ corresponds to fully folded configuration. From the concentration dependence of the parameter n_f (figure 4.12) it is evident that the phase transition from *I* to *Sm-fA* phase is followed by a sharp increase of the fraction of folded duplexes from about 0.15-0.20 to 0.40-0.50. Further increase of the concentration causes the gradual increase of n_f until it reaches the value of 1. Finally, a phase transition to the crystal state occurs at concentration above 300 mg ml^{-1}, which is way above the concentrations at which experiments were performed. The concentration dependence of n_f shows that to form the *Sm-fA*, a certain fraction of G-DNA duplexes needs to attain a folded conformation, but it is definitely not necessary for all of them to be folded. This can be clearly seen from the distribution of angles between two cylinders of the same G-DNA duplex at different pressures shown in figure 4.13. It can be seen that in *I* phase the distribution of angles does not change with the pressure. However, there are three populations of different angles visible for the *Sm-fA* phase. The largest number of duplexes is in the folded conformation and this number increases with the pressure. In contrast, the other two populations decrease.

Comparing the simulations with experimental results it is fair to say that the simple model assumed in the Monte Carlo simulations captures quite well the phase behavior of G-DNA. At the highest concentrations the simulations do not show any kind of long-range order of G-DNA duplexes within the smectic layers, opposite to experiments. However, the simulations support the key observations obtained in the experiments and provide a better understanding of the physical mechanisms related to the formation of *Sm-fA* phase.

An important finding from simulations is that in order to stabilize the *Sm-fA* phase not all G-DNA duplexes need to be in a folded conformation. It is sufficient to have only a fraction of G-DNA duplexes folded to inhibit the formation of polydisperse linear aggregates by end-to-end stacking and to promote the formation of *Sm-fA* phase. Folding of G-DNA duplexes leads to a significant reduction of excluded volume, compared to their unfolded configuration. It was numerically estimated that

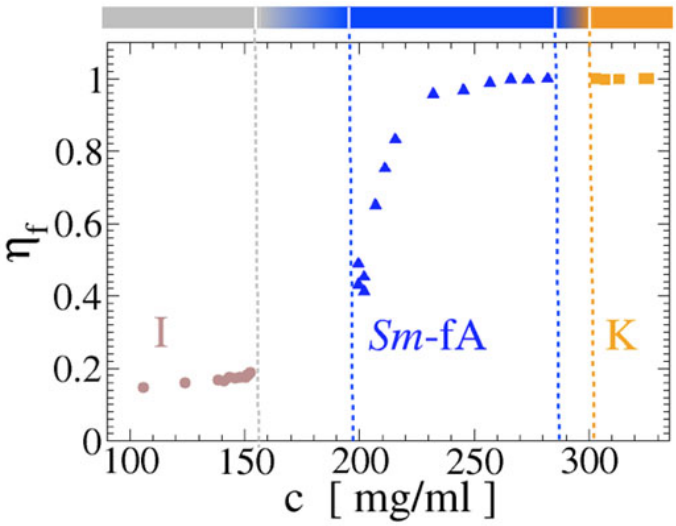

FIGURE 4.12: Concentration dependence of the fraction of folded duplexes n_f, adapted from [10]

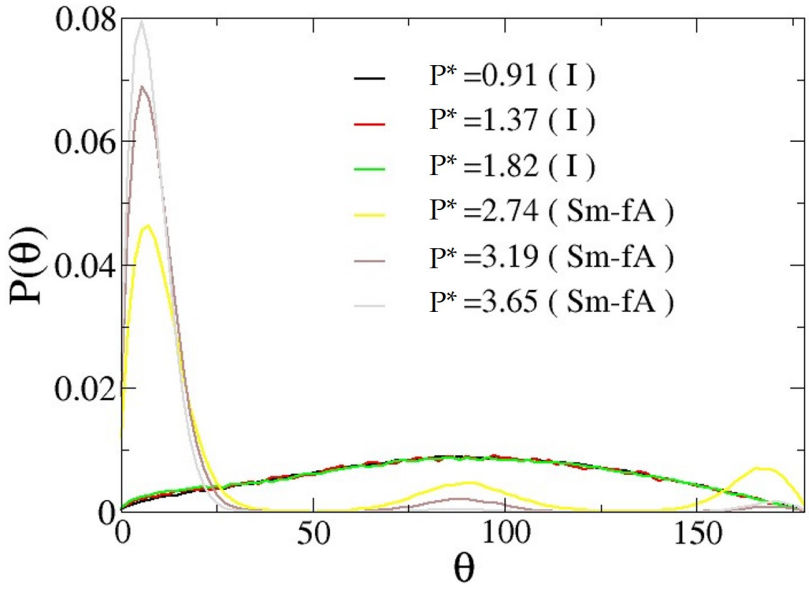

FIGURE 4.13: Distribution of angles between two cylinders of the same G-DNA duplex at different pressures for isotropic ($\beta P v_0$= 0.91, 1.37, and 1.82) and smectic phase ($\beta P v_0$= 3.19 and 3.65).

the excluded volume of folded particles is 1.4 times smaller than of the unfolded ones [10]. Therefore, folding is an efficient way to minimize the free energy of the system suggesting that the folding process itself is purely entropic. This issue is discussed into more details in section 4.5 where the experimental evidence is provided.

The simulations show the first LC phase following the *I* phase is *Sm-fA*, with no *N** phase found in between. A possible reason why the *N** phase does not appear in the MC simulations could be the flexibility overestimation for the G-20T-DNA since experiments indicate the formation of *N** phase in a narrow concentration range. This issue is addressed from the experimental point of view by changing the length of a flexible spacer.

4.3 *I*/*Sm-fA* phase coexistence in gapped DNA duplexes

In the previous section 4.2.1 the hypothesis was raised that, due to the overestimation of gap flexibility, the MC simulations do not capture the formation of *N** phase at concentrations below those at which *Sm-fA* phase appears. Here, in order to address this point, the phase behavior of G-DNA with spacers longer than 20 T will be presented (see section 4.4 and figure 4.17 for the complete phase diagram of G-DNA duplexes).

The concentration-dependent X-ray scattering profiles of G-DNA with a flexible spacer of 30T bases (G-30T-DNA) are shown in figure 4.14. At the first look, there are not many differences present in these scattering profiles comparing to those of G-20T-DNA. At the highest concentrations, presented in the two top panels, G-30T-DNA forms *Sm-B* phase, which is witnessed by a set of equidistant smectic peaks and a sharp q_{DNA} peak. Decreasing the concentration from 280.16 to 271.55 mg ml^{-1}, the q_{DNA} peak broadens out but the smectic peaks remain, so we identify this phase as *Sm-fA* phase. Probing the birefringent part of the biphasic sample at the concentration of 229.98 mg ml^{-1} reveals the *I*/*Sm-fA* phase coexistence in contrast to G-20T-DNA duplexes. Interestingly, the birefringent part of the biphasic G-30T-DNA sample between crossed polarizers shown in figure 4.15 reveals the formation of smectic monodomain. The smectic monodomain develops after few weeks of sample storage and its size stretches over the whole glass capillary diameter. Upon rotation of the capillary, the birefringent pattern almost completely disappears. Eventually, at 209.89 mg ml^{-1} the fully *I* phase is reached. The *I*/*Sm-fA* coexistence found in G-30T-DNA duplexes confirms that the overestimation of the spacer flexibility in the model G-20T-DNA duplexes is the reason for the absence of the *N** in the simulated phase sequence in figure 4.11.

The key differences between LC phases of F-DNA, G-20T-DNA, and G-30T-DNA in two-phase coexistence region are summarized in figure 4.16 in terms of SAXS profiles and POM images. The POM images show tactoids, liquid crystalline microdroplets which are spontaneously nucleated in the isotropic phase. For G-30T-DNA duplexes, the micropgraph displays a LC domain with a fan-shaped texture typical for a *Sm* phase. Similar texture was observed already in G-20T-DNA duplexes (figure 4.9, the top micropgraph on the right-hand side). Completely different are tactoid textures for G-20T-DNA and F-DNA duplexes. Spherical cholesteric droplets are formed, as evident from their bright striped appearance. However, the differences in the shape of fingerprint textures suggest that the director configuration differs for the two cases. For G-20T-DNA, the texture indicates cholesteric structure under homeotropic boundary conditions (looking perpendicularly to the cholesteric axis). In case of F-DNA, a concentric cholesteric layer structure is formed.

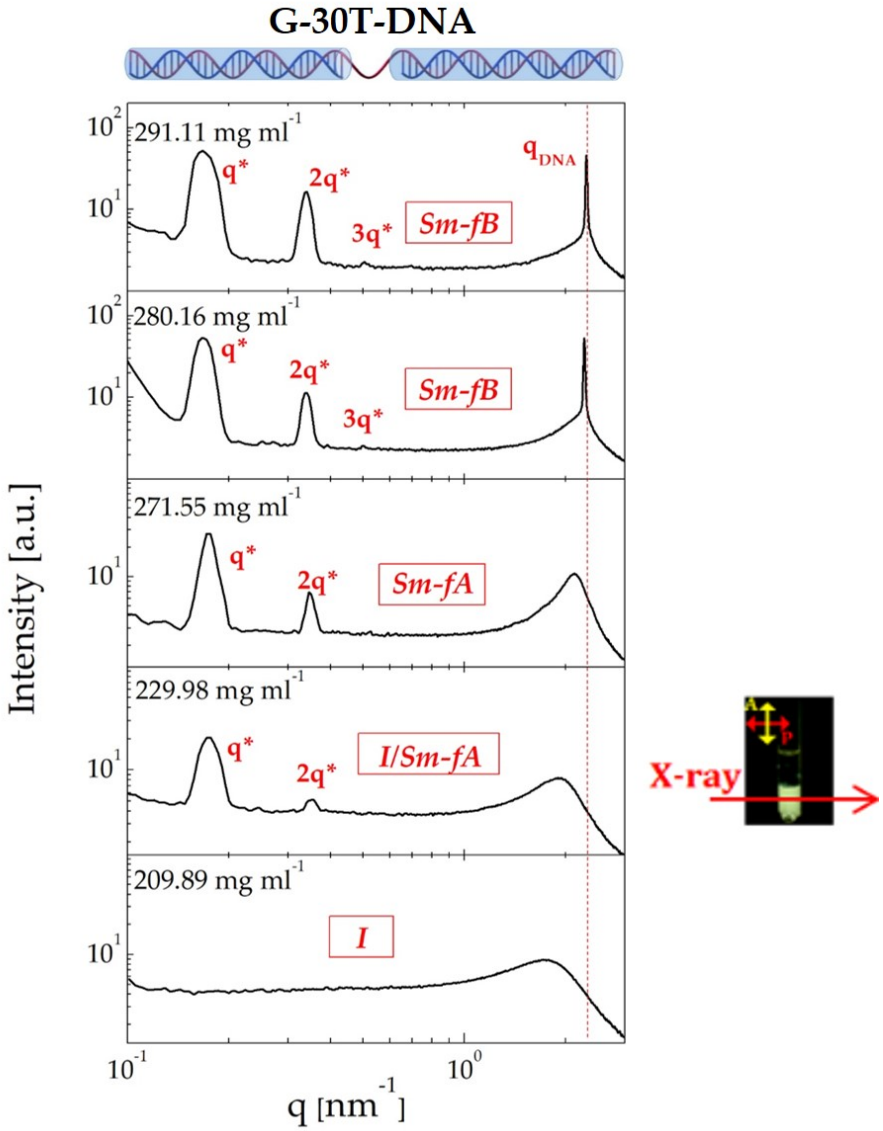

FIGURE 4.14: X-ray scattering profiles of G-30T-DNA duplexes at concentrations (from top to the bottom) c = 291.11, 280.16, 271.55, 229.98 (two-phase coexistence sample), and 209.89 mg ml^{-1}. On the right-hand side is sample observed under crossed polarizers. The red arrow indicates part of the sample probed by the x-ray beam.

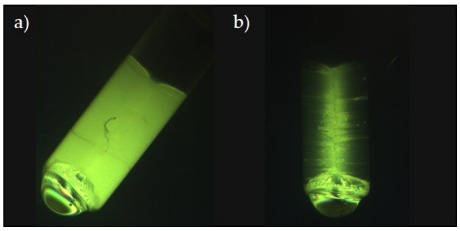

FIGURE 4.15: The spontaneous formation of smectic monodomains in birefringent part of the biphasic G-30T-DNA sample at concentration of c= 229.98 mg ml^{-1}. In a) a uniform birefrigent pattern is visible, while in b) upon the rotation of the capillary one observes almost complete disappearance of birefringence. The bright line is the connecting point of two monodomains.

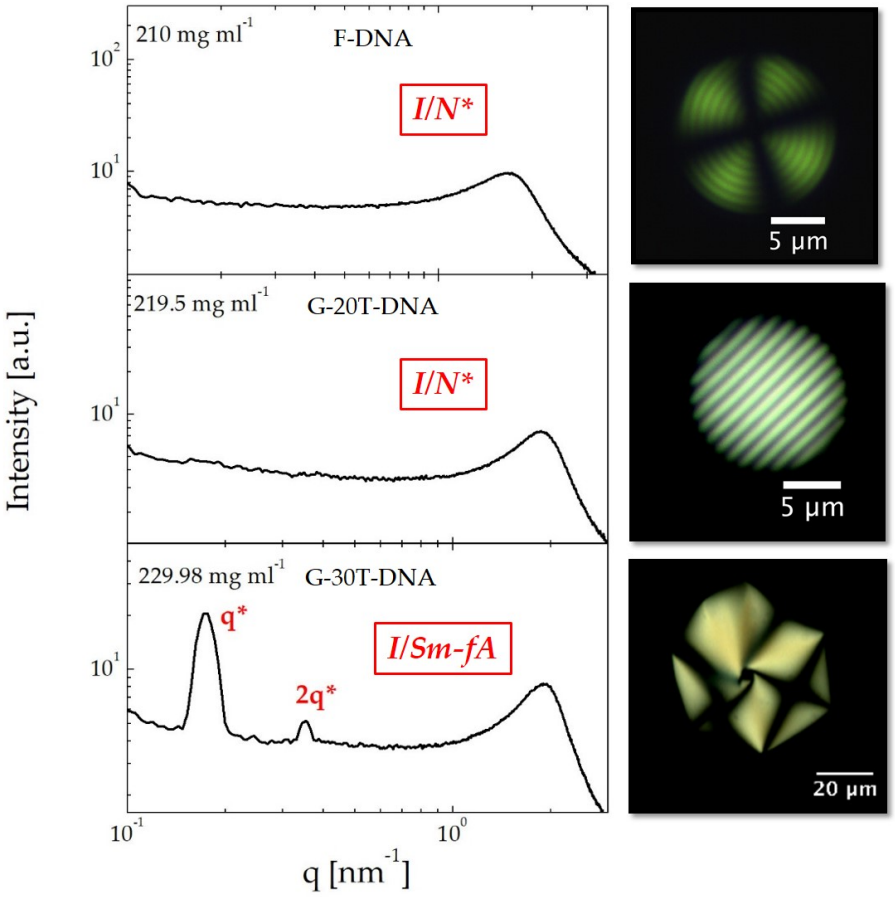

FIGURE 4.16: X-ray scattering profiles of F-DNA (c= 210 mg ml^{-1}), G-20T-DNA (c= 219.5 mg ml^{-1}), and G-30T-DNA (c= 229.98 mg ml^{-1}). For all three scattering profiles, the measurement were taken on birefringent part of the biphasic (I/LC) sample. On the right hand side are the corresponding POM images of typical LC tactoids.

It is clear that the system architecture significantly affects the tactoid structure and maybe even the nucleation pathways themselves. However, studying these effects into detail is out of the scope of this thesis.

4.4 Phase diagram of gapped DNA duplexes

Two different lengths of flexible spacers in G-DNA duplexes have been already explored. However, the flexible spacer length influence on phase behavior of G-DNA and its role in the stability of *Sm-fA* phase is still not fully addressed. To this end, a series of G-DNA duplexes with lengths of flexible spacers ranging from 4T up to 40T bases has been synthesized and their self-assembly behavior was studied using SAXS.[3] The full phase diagram of G-DNA duplexes based on SAXS data complemented by POM is shown in figure 4.17. Experimental points obtained by SAXS are represented by crosses while regions in which certain phases appear are marked with different colors. Fully paired analogue of G-20T-DNA duplex, F-DNA, is included on the left-hand side of the phase diagram.

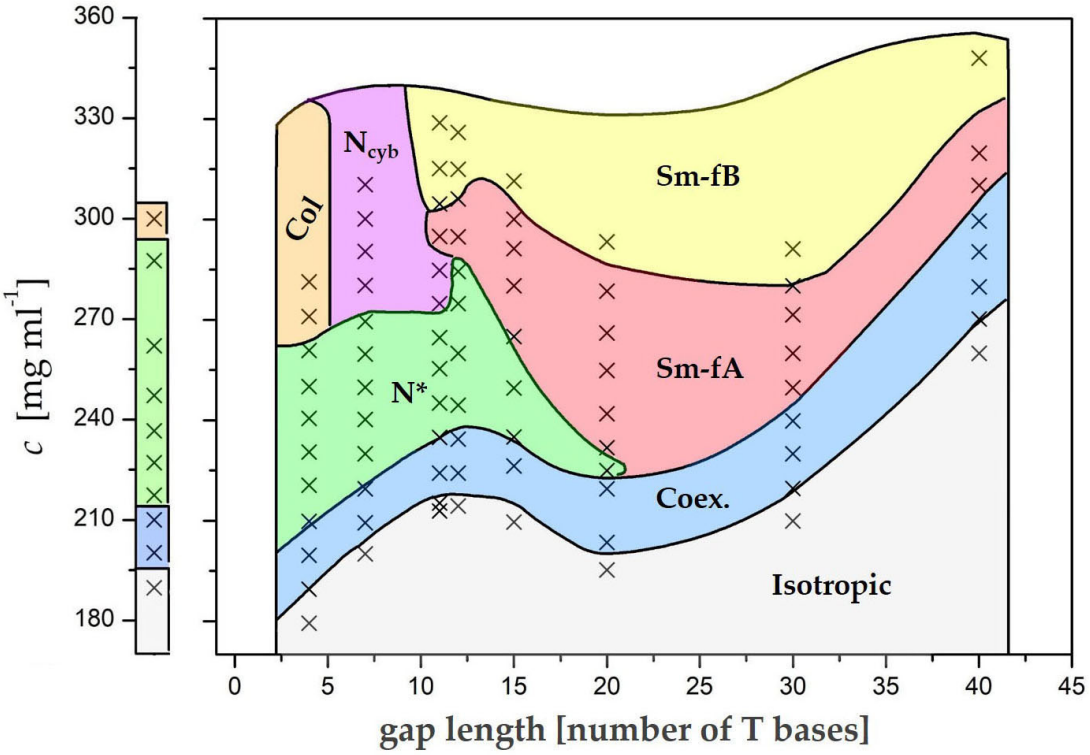

FIGURE 4.17: Complete phase diagram of G-DNA duplexes, with gaps ranging from 4T to 40T bases. Crosses mark experimental data, and regions in which different phases occur are shown in different colors. On the left hand side a phase sequence of a fully-paired analogue of G-20T-DNA duplex, dsDNA with length of 116 bp is shown.

The phase diagram will be presented using the G-20T-DNA as a starting point. Next, the phase behavior of G-DNA duplexes with longer flexible spacers will be

[3]Note that the upper limit of 40T bases is set by the length limitations of single DNA strands synthesis.

discussed, and finally phase behavior of those with shorter spacers. The G-20T-DNA duplexes form an unconventional *Sm-fA* phase at sufficiently high concentrations, as already shown earlier in this chapter. Decreasing the concentration, a very narrow concentration range where N^* phase appears is also observed, as well as I/N^* phase coexistence before the final phase transition to an orientationally disordered I phase.

The phase behavior of G-DNA duplexes with longer flexible spacers of 30T (G-30T-DNA) and 40T (G-40T-DNA) bases shows a few notable differences comparing to G-20T-DNA. Both G-30T-DNA and G-40T-DNA show the same phase sequence, in particular exhibiting *I/Sm-fA* phase coexistence before they undergo a phase transition to *Sm-fA*. As the flexible spacer length increases, the two-phase coexistence region broadens and the phase boundaries shift to higher concentrations, which is in line with expectations for flexibility introduced to rod-like systems [17]. As expected, the increase of the flexible spacer length from 20T to 40T bases leads to the increase of the smectic layering in the G-DNA duplexes. Figure 4.18 displays the shift in primary peak q^* position for different lengths of flexible spacers, which corresponds to the increase of layer spacing from ~ 35 nm to ~ 39 nm. The experimental results obtained for G-30T-DNA and G-40T-DNA are in good agreement with MC simulations presented earlier in section 4.2.1 where no N^* phase was observed in G-20T-DNA due to the overestimation of the spacer flexibility.

For flexible spacer lengths below 20 T bases, the phase sequences observed are strikingly different compared to G-DNA duplexes with longer spacers. Decreasing the spacer length down to 12 T bases, the broadening of N^* at the expense of *Sm-fA* phase appears. As a result, the transition from N^* to *Sm-fA* occurs at higher concentrations. This could be understood in terms of flexibility. The shorter spacer makes the folding harder to achieve. A clear manifestation of this reflects on the phase behavior of G-DNA duplexes with 11 T flexible spacer (G-11T-DNA). Finally, further increase of the concentration for G-DNA duplexes with flexible spacers between 20 T and 11 T bases causes an occurrence of the sharp q_{DNA} peak suggesting the transition from *Sm-fA* to *Sm-fB* phase.

Concentration-dependent X-ray scattering profiles of G-11T-DNA are shown in figure 4.19. The phase sequence presented here contains a new type of LC phase occurring between N^* and *Sm-fA* phase. At 315.18 mg ml^{-1} scattering profile shows one sharp intense q_{DNA} peak, but also a weaker principle peak at q^* value of scattering vector followed by equidistant higher order reflections. This SAXS profile suggests the formation of *Sm-fB* phase. At lower total DNA concentration of 294.94 mg ml^{-1}, the scattering profile looks fairly similar. The main difference is another slightly broader peak superimposed on the q_{DNA} peak. This phase is identified as *Sm-fA* phase. The sharp q_{DNA} completely disappears with lowering the concentration to 284.79 mg ml^{-1} without noticeable shift in the broad peak position. Interestingly, smectic peaks are partially gone (this can be also seen in the 2D scattering pattern in figure 4.20). The q^* peak disappears, but one peak remains. The absence of the q^* peak could be a combined effect of the form factor and structure factor contributing to the total scattering intensity of the anisotropic self-assembled particles. However, the overwhelming prevalence of the phase with such SAXS signature and the absence of the *Sm* phase in G-DNA duplexes with 7 T flexible spacer (G-7T-DNA) weakens this scenario.

If the remaining peak in G-11T-DNA scattering profile is considered as primary reflection, it corresponds to the short-range smectic layering of ~ 16 nm, which is close to the length of one folded G-11T-DNA duplex. This could be related to the formation of the cybotactic nematic (N_{cyb}), a structure originally proposed by de Vries [28, 29, 30]. In this structure, clusters with short-range layer-like arrangement

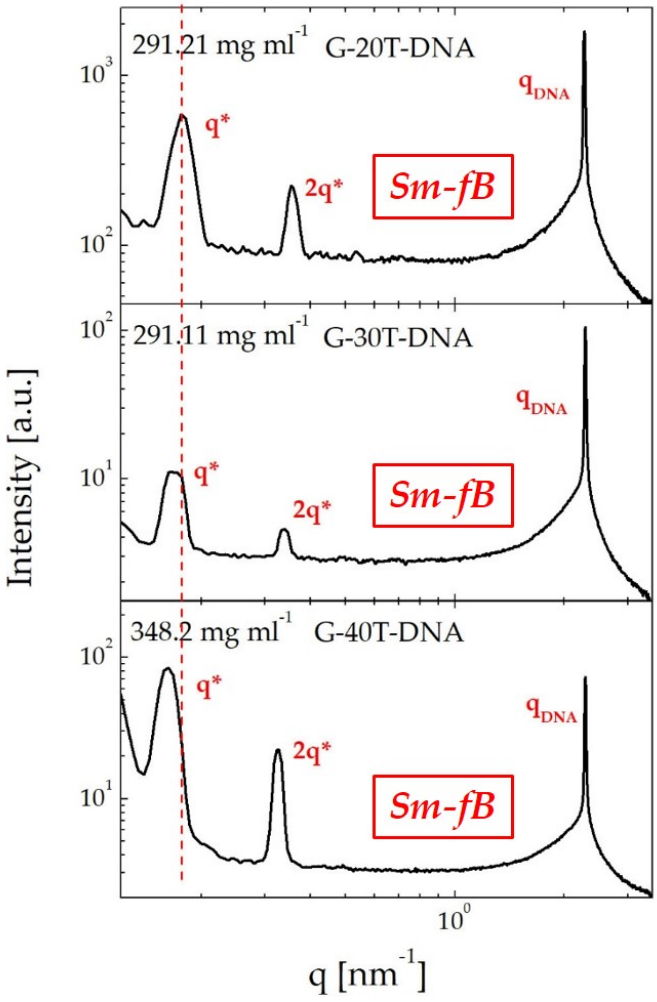

FIGURE 4.18: X-ray scattering profiles of G-20T-DNA, G-30T-DNA, and G-40T-DNA at the highest total DNA concentrations measured. All SAXS profiles reveal the formation of *Sm-fB* phase. However, the position of q^* slightly changes, which indicates that the smectic spacing increases as the flexible spacer becomes longer.

of molecules are present related to pretransitional fluctuations of smectic order near the nematic to smectic transition. Since this phase is present in relatively wide concentration range in G-11T-DNA between N^* and *Sm-fA* phase and especially in G-7T-DNA, the cybotactic clusters formed are probably not related to smectic order fluctuations.

In bent-core mesogens such as banana-, boomerang-, and V-shaped molecules cybotactic clustering was observed. The molecular arrangement within the cybotactic nanoclusters is assumed to be smectic C-like layered structure with intrinsic biaxial orientational order [31, 32, 33]. The X-ray scattering signature of this phase is a four-spot scattering pattern in the aligned nematic phase characterized by an azimuthal splitting of the low angle diffuse signals into two pairs of symmetrically located diffuse spots.

The SAXS pattern of the shear-aligned G-11T-DNA sample at concentration of 274.85 mg ml^{-1} exhibits exactly the same distinctive four-spot splitting of a diffuse

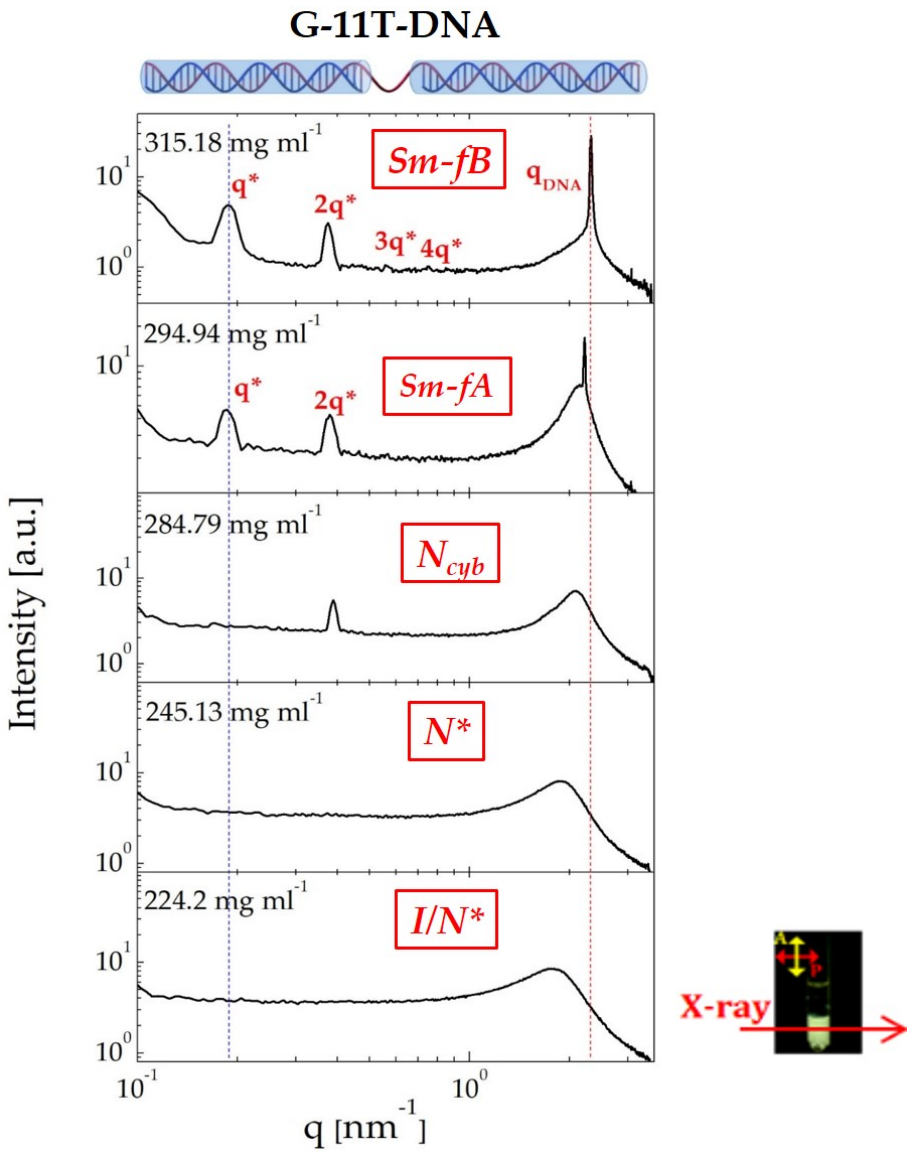

FIGURE 4.19: X-ray scattering profiles of G-11T-DNA duplexes at concentrations (from top to the bottom) c = 315.18, 294.94, 284.79, 245.13, and 224.2 mg ml^{-1}. On the right-hand side is sample observed under crossed polarizers. The red arrow indicates part of the sample probed by the x-ray beam.

q_{DNA} peak as shown in figure 4.21 a). This can be clearly seen in the azimuthal θ-scan of the diffuse ring marked as a white donut area shown in figure 4.21 b) as the red curve. The short flexible spacers in G-DNA duplexes allow their partially folded configuration which could resemble the above mentioned bent-core mesogens. Therefore, the formation of the N_{cyb}, which can be considered as strongly fragmented smectic C phase, seems reasonable.

The unconventional nematic N_{cyb} phase is present also in a wide concentration range in G-7T-DNA duplexes, which can be seen in concentration-dependent X-ray scattering profiles in figure 4.22 a). No *Sm* phase is present in G-7T-DNA duplexes, even at the highest total DNA concentration. Apart from the q_{DNA} peak, only one peak is present at lower values of scattering vector q, similar to G-11T-DNA. From

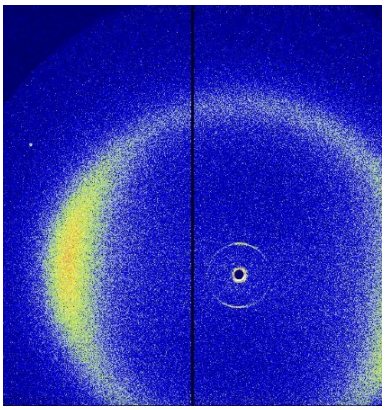

FIGURE 4.20: X-ray scattering pattern of G-11T-DNA duplexes at c = 284.79 mg ml^{-1}.

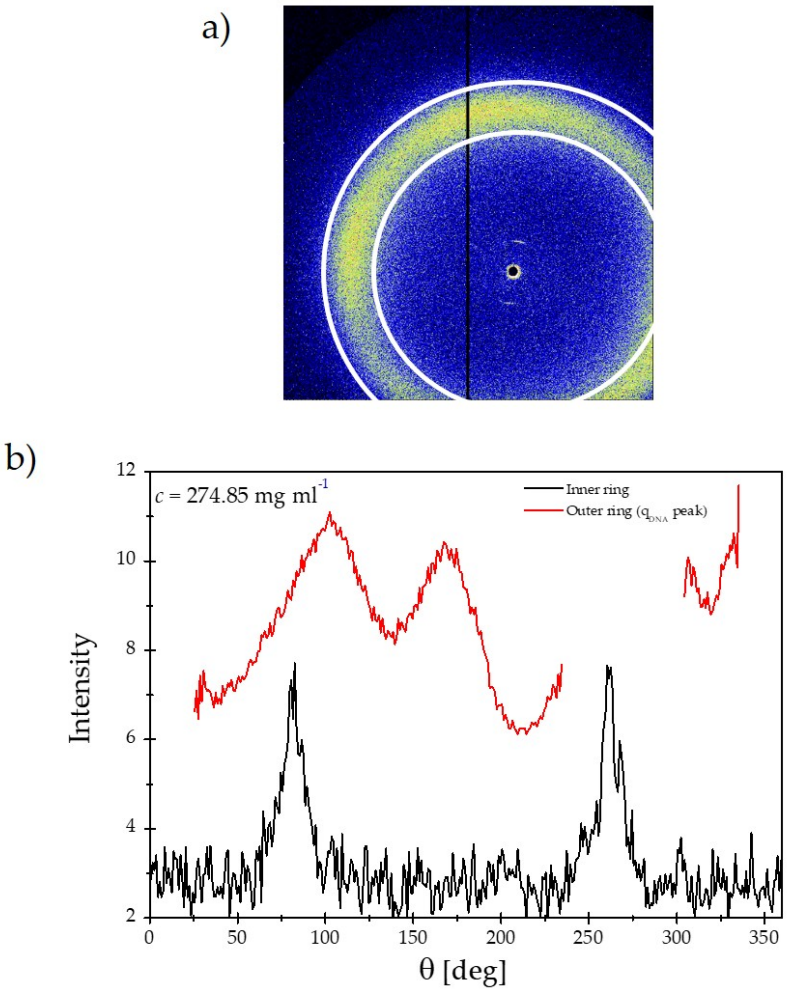

FIGURE 4.21: a) X-ray scattering pattern of G-11T-DNA duplexes at c = 274.85 mg ml^{-1}. The white donut marks the azimuthal integration area. b) Azimuthal integration of the outer ring and inner arcs from the scattering pattern in a).

the position of this peak, a correlation length is calculated as $d = 2\pi/q$ and it is around 16 nm. As the total DNA concentration decreases, the position of this peak shifts slightly to higher q values indicating a slight decrease of d. Finally, decreasing the total DNA concentration down to 269.45 mg ml^{-1} G-7T-DNA duplexes undergo a phase transition from the N_{cyb} to N^* phase. For G-DNA duplexes with even shorter spacer of 4 T bases (G-4T-DNA) the same phase sequence as in case of F-DNA duplexes is found, with no N_{cyb}: *I*, *I*/N^*, N^*, *Col*. This can be seen in figure 4.23.

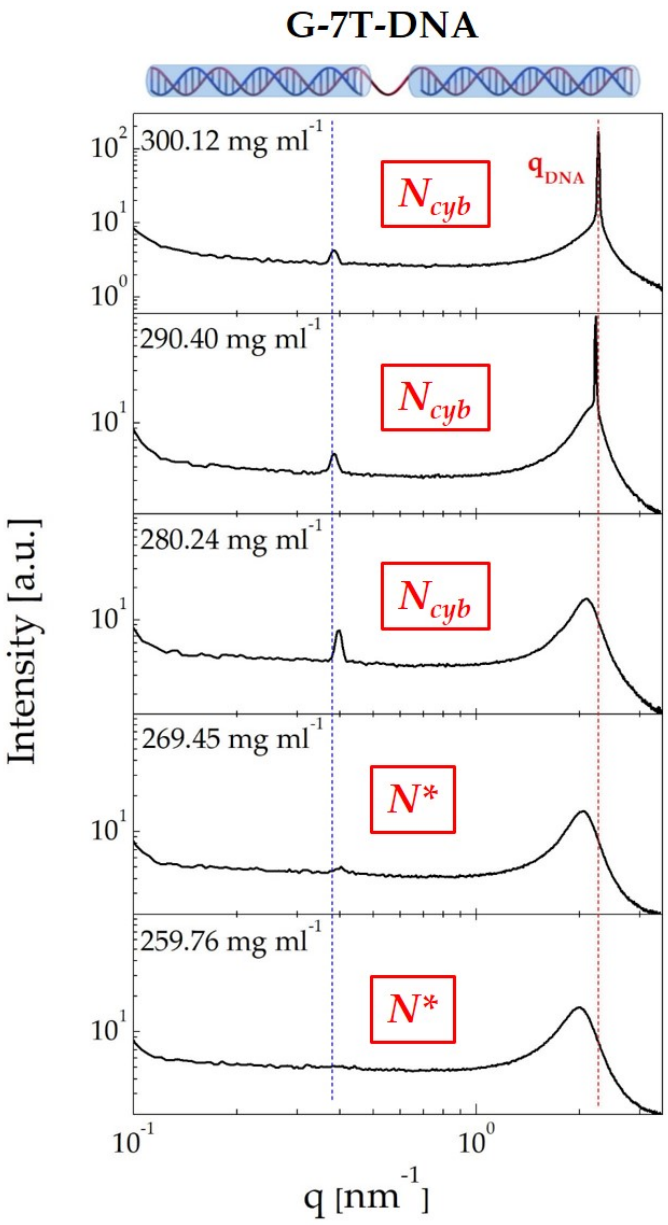

FIGURE 4.22: X-ray scattering profiles of G-7T-DNA duplexes at total DNA concentrations (from top to the bottom) c = 300.12, 290.40, 280.24, 269.45, and 259.76 mg ml^{-1}.

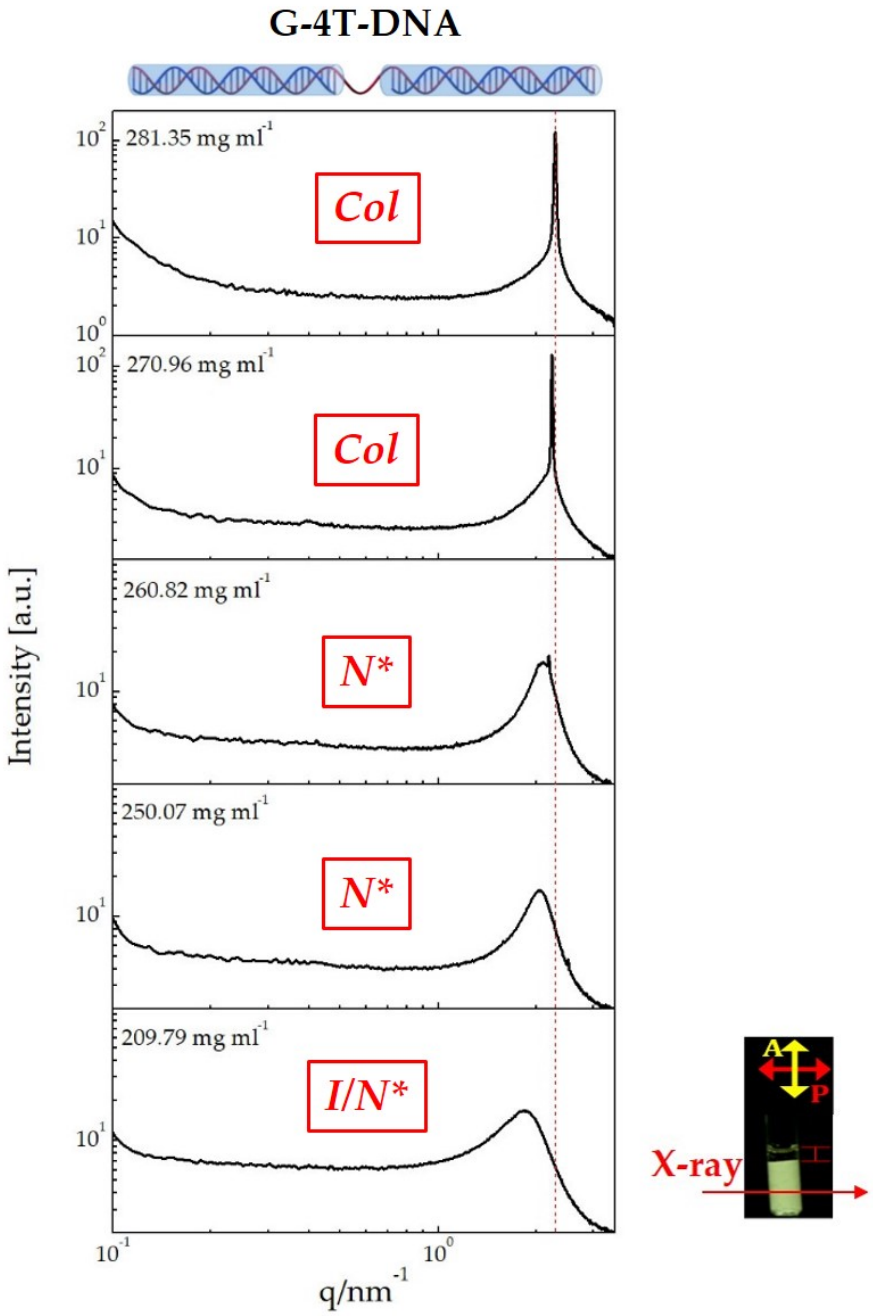

FIGURE 4.23: X-ray scattering profile of G-4T-DNA duplexes at total DNA concentrations (from top to the bottom) c = 281.35, 270.96, 260.82, 250.07, and 209.79 mg ml^{-1}. On the right-hand side is sample observed under crossed polarizers. The red arrow indicates part of the sample probed by the x-ray beam.

4.5 Entropic origin of folding in gapped DNA duplexes

It has been shown how different lengths of flexible spacer influence the phase behavior of gapped DNA duplexes. MC simulations have revealed the crucial role of end-to-end stacking interactions in the formation *Sm-fA* phase. In order to further investigate the importance of blunt-end attractions experimentally, short flexible non-sticky overhangs at each blunt end of the G-DNA duplex were introduced. Overhangs in DNA are unpaired nucleotides located at either 3′ or 5′ end of DNA duplex. In case of G-DNA duplexes described in this chapter, six unpaired T bases are expected to create a steric hindrance and prevent end-to-end adhesion of DNA duplexes. This was already demonstrated in the self-assembly of ultra-short DNA duplexes [9, 34] where polyT overhangs destabilize LC phases. Synthetically, this can be done by modification of the long ssDNA sequence involved in the fabrication of G-DNA duplexes (for more details see section 3.3.1). In this work, short polyT overhangs were introduced to blunt-ends of G-20T-DNA duplexes. Schematic representation of the resulting G-20T-polyT-DNA duplex is shown in the top part of the figure 4.24.

At the beginning of this chapter, in section 4.2, it has been shown that with increasing concentration G-20T-DNA forms a sequence of LC phases which includes phase transitions from *I* phase, through *I*/*N** phase coexistence to *N**, to *Sm-fA* phase. The phase behavior of G-20T-polyT-DNA duplexes is different compared to blunt-ended G-20T-DNA. SAXS profiles for G-20T-polyT-DNA are shown in figure 4.24. The sharp q_{DNA} peak together with smectic peaks q^* and $2q^*$ at the highest concentration measured indicate the formation of *Sm-fB* phase. Decreasing the total DNA concentration down to 300.4 mg ml^{-1} G-20T-polyT-DNA undergoes a phase transition to *Sm-fA* phase. This is witnessed by broadening of the q_{DNA} peak, while equidistant smectic peaks remain. The upright orientation of G-20T-polyT-DNA duplexes within the layers is evidenced by 2D SAXS patterns shown in figure 4.25 a). The outer arcs corresponding to the q_{DNA} peak are in a perpendicular orientation relative to the inner arcs corresponding to smectic peaks. At total DNA concentration of 270.26 mg ml^{-1} two-phase coexistence region is reached. By probing the birefringent part of the sample, as visible in the figure 4.24, the SAXS profile reveals the formation of *Sm-fA* phase. The corresponding 2D scattering pattern in figure 4.25 b) shows a series of spot-like reflections close to the beam stop (indicated by white arrows), in contrast to the one in 4.25 a). This suggests a significant degree of long-range order in the direction perpendicular to the smectic layers. It is important to mention that this scattering pattern occurs without application of external fields, i.e. no shear was applied. Further evidence for the formation of *I*/*Sm-fA* phase coexistence can be seen in the micrograph shown in figure 4.26 a). Asymmetric, spindle-like tactoids are observed with no presence of fingerprint texture, typical for *N** phase. Below the total DNA concentration of 255.27 mg ml^{-1}, the system is in orientationally disordered *I* phase.

Calculating the smectic spacing length in the *Sm-fA* phase of G-20T-polyT-DNA duplexes as $d=2\pi/q^*$ gives us a value of around 18 nm, which is almost two times smaller than the layer spacing of G-20T-DNA. The calculated value fits quite well to the length of one folded G-20T-polyT-DNA duplex. The smaller spacing suggests that G-20T-polyT-DNA duplexes in the *Sm* phase are arranged in a folded fashion as illustrated in the figure 4.26 b). Due to the polyT overhangs no end-to-end stacking is possible. Therefore, smectic layers are composed of single folded G-20T-polyT-DNA duplexes, with no preferred orientation within the layers. Observing the *Sm-fA*

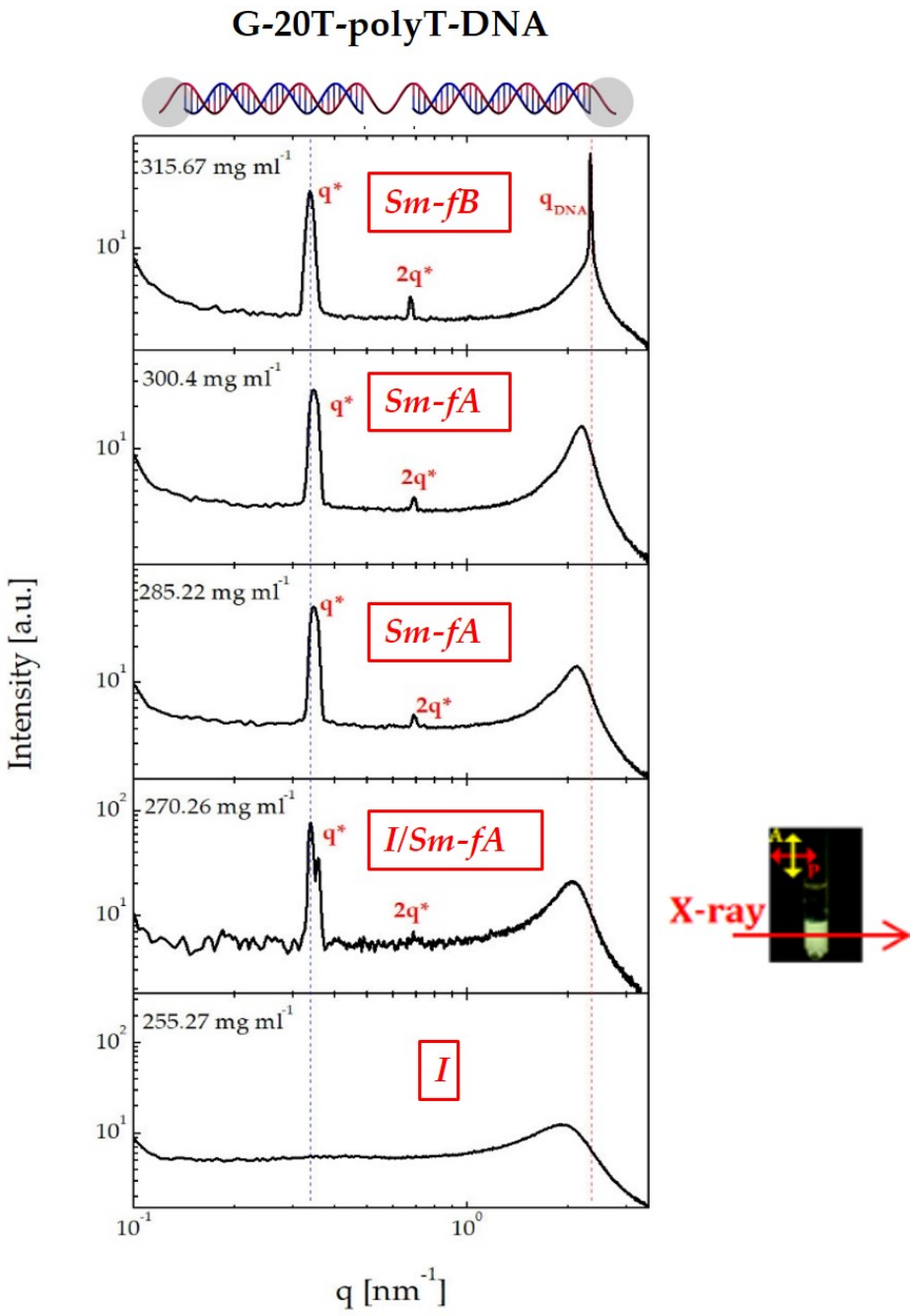

FIGURE 4.24: a) X-ray scattering profiles of G-20T-polyT-DNA at total DNA concentrations (from top to the bottom) c = 315.67, 300.4, 285.22, 270.26, and 255.27 mg ml^{-1}. On the right-hand side is sample observed under crossed polarizers. The red arrow indicates part of the sample probed by the x-ray beam.

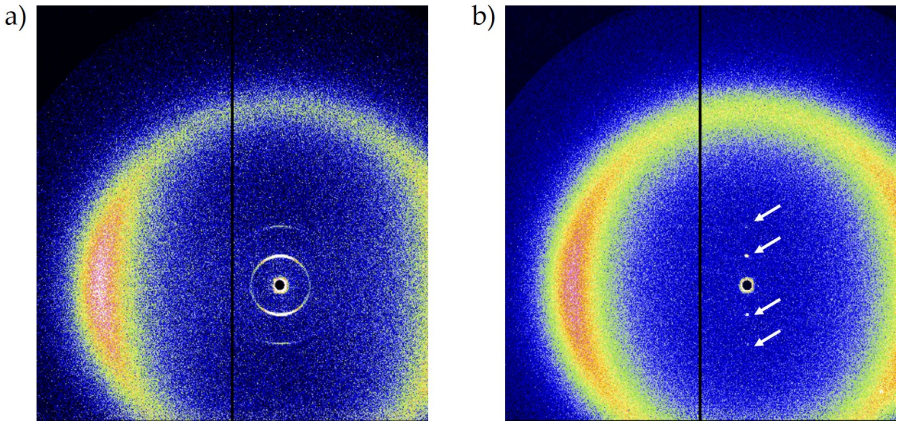

FIGURE 4.25: X-ray scattering pattern of G-20T-polyT-DNA duplexes at a) c = 285.22 mg ml^{-1}, and b) c = 270.26 mg ml^{-1} .

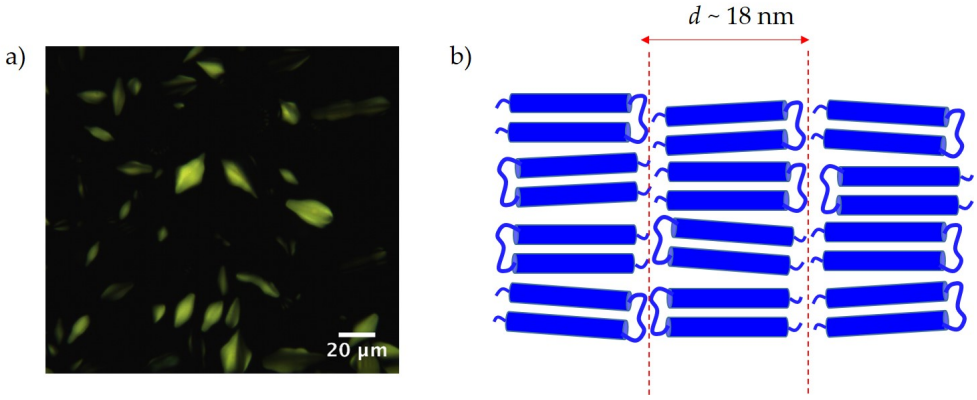

FIGURE 4.26: a) POM of the two-phase coexistence G-20T-polyT-DNA sample. b) Schematic representation of the possible packing scenario in the *Sm-fA* phase formed by G-20T-polyT-DNA duplexes.

phase in G-DNA duplexes with disturbed attractive end-to-end interactions demonstrates that the folding process itself is purely entropic. Regardless of the presence of attractive end-to-end stacking interactions, folding of G-DNA duplexes appears in order to minimize the excluded volume of the system. This is in line with the numerical estimation for the reduction of excluded volume upon folding of G-DNA duplexes, reported in the section 4.2.1.

4.6 Summary and conclusions

Incorporation of single-stranded region, in form of a flexible spacer, into dsDNA results in G-DNA duplexes which show very rich phase behavior. LC phase of special interest is an unconventional *Sm-fA* phase formed in G-DNA duplexes with sufficiently long flexible spacers. G-DNA duplexes in *Sm-fA* are packed in a folded fashion, stacked on top of one another building smectic layers composed of two duplexes. The importance of end-to-end stacking interactions for the stabilization of the *Sm-fA* was additionally supported by MC simulations. Despite the simplicity of the employed model, MC simulations support the experimental findings and provide a deeper insight into physical mechanism of the *Sm-fA* formation. It was found that only a fraction of G-DNA duplexes needs to be in a folded conformation to build a layer-like structure. Moreover, the folding process itself has entropic origin and leads to the reduction of the excluded volume of the system, as estimated numerically. The entropic nature of folding was addressed and confirmed also experimentally by studying G-20T-DNA duplexes with screened end-to-end interactions.

Thanks to the DNA used as a building block for these nanostructures, it is possible to tune the length and position of flexible spacer, as well as of the stiff blocks, with sub-nanometer precision. This significantly influences the self-assembly behavior of G-DNA duplexes. The full phase diagram was presented providing an overview over different LC phases formed by G-DNA with various lengths of flexible spacers. Particularly interesting is the formation of *I/Sm-fA* phase coexistence for spacers length larger than 20 T bases. Additionally, the formation of a new type of nematic phase N_{cyb} was observed, in which smectic-like cybotactic clusters are formed. Similarly to conventional nematic, this phase possesses correlations only between neighboring molecules, and it appears in G-DNA duplexes which don't fold easily due to the insufficient length of the flexible spacers.

It is worth to mention that the theoretical studies on purely steric model systems have predicted that the flexibility in the system stabilizes the *Sm* at the expense of *N* phase [35, 36, 37, 38, 39]. However, these systems introduce the flexibility in the form of a flexible tail attached to the ends of a stiff rod. Contrary to this, in G-DNA duplexes, flexibility is introduced within the stiff DNA rod. G-DNA duplexes can be considered a new class of lyotropic LC materials which show the formation of unconventional novel types of LC phases that are absent in other materials, such as *Sm-fA* and *Sm-fB* phase.

Bibliography

[1] P. Hagerman. Flexibility of DNA. *Annu. Rev. Biophys. Biophys. Chem.*, 17:265–286, 1988.

[2] C. G. Baumann, S. B. Smith, V. A. Bloomfield, and C. Bustamante. Ionic effects on the elasticity of single DNA molecules. *Proceedings of the National Academy of Sciences of the United States of America*, 94:6185–6190, 1997.

[3] M. C. Murphy, I. Rasnik, W. Cheng, T. M. Lohman, and T. Ha. Probing Single-Stranded DNA Conformational Flexibility Using Fluorescence Spectroscopy. *Biophysical Journal*, 86:2530–2537, 2004.

[4] F. Livolant and Y. Bouligand. Liquid crystalline phases given by helical biological polymers (DNA, PBLG and xanthan). Columnar textures. *Journal de physique*, 47:1813–1827, 1986.

[5] T. E. Strzelecka, M. W. Davidson, and R. L. Rill. Multiple liquid crystal phases of DNA at high concentrations. *Nature*, 331:457–460, 1988.

[6] F. Livolant, A. M. Levelut, J. Doucet, and J. P. Benoit. The highly concentrated liquid-crystalline phase of DNA is columnar hexagonal. *Nature*, 339:724–726, 1989.

[7] F. Livolant. Ordered phases of DNA in vivo and in vitro. *Physica A*, 176:117–137, 1991.

[8] K. Merchant and R. L. Rill. DNA length and concentration dependencies of anisotropic phase transitions of DNA solutions. *Biophysical Journal*, 73:3154–3163, 1997.

[9] M. Nakata, G. Zanchetta, B. D. Chapman, C. D. Jones, J. O. Cross, R. Pindak, T Bellini, and N a Clark. End-To-End Stacking and Liquid Crystal Formation of 6- to 20-Base Pair DNA Duplexes. *Science*, 318:1–4, 2007.

[10] M. Salamonczyk, J. Zhang, G. Portale, C. Zhu, E. Kentzinger, J. T. Gleeson, A. Jakli, C. De Michele, J. K.G. Dhont, S. Sprunt, and E. Stiakakis. Smectic phase in suspensions of gapped DNA duplexes. *Nature Communications*, 7:1–9, 2016.

[11] D. Durand, J. Doucet, and F. Livolant. A study of the structure of highly concentrated phases of DNA by X-ray diffraction. *Journal De Physique Ii*, 2:1769–1783, 1992.

[12] P. Bolhuis and D. Frenkel. Tracing the phase boundaries of hard spherocylinders. *The Journal of Chemical Physics*, 106:666–687, 1997.

[13] S. C. McGrother, D. C. Williamson, and G. Jackson. A re-examination of the phase diagram of hard spherocylinders. *Journal of Chemical Physics*, 104:6755–6771, 1996.

[14] A. M. Bohle, R. Hołyst, and T. Vilgis. Polydispersity and Ordered Phases in Solutions of Rodlike Macromolecules. *Physical Review Letters*, 76:1396–1399, 1996.

[15] G. Maret, M. v. Schickfus, A. Mayer, and K. Drasfeld. Orientation of nucleic acid in high magnetic fileds. *Phys. Rev. Lett.*, 35:397–400, 1975.

[16] E. Pouget, E. Grelet, and M. P. Lettinga. Dynamics in the smectic phase of stiff viral rods. *Physical Review E - Statistical, Nonlinear, and Soft Matter Physics*, 84: 1–6, 2011.

[17] M. Dijkstra and D. Frenkel. Simulation study of the isotropic-to-nematic transitions of semiflexible polymers. 51:5891–5898, 1995.

[18] Z. Y. Chen. Nematic Ordering in Semiflexible Polymer Chains. *Macromolecules*, 26:3419–3423, 1993.

[19] A. R. Khokhlov and A. N. Semenov. Liquid-crystalline ordering in the solution of long persistent chains. *Physica A: Statistical Mechanics and its Applications*, 108: 546–556, 1981.

[20] A. R. Khokhlov and A. N. Semenov. Liquid-crystalline ordering in the soluton of partially flexible macromolecules. *Physica A: Statistical Mechanics and its Applications*, 112A:605–614, 1982.

[21] Z. Dogic and S. Fraden. Smectic phase in a colloidal suspension of semiflexible virus particles. *Physical Review Letters*, 78:2417–2420, 1997.

[22] A. Kuijk, D. V. Byelov, A. V. Petukhov, A. van Blaaderen, and A. Imhof. Phase behavior of colloidal silica rods. *Faraday Discussions*, 159:181, 2012.

[23] D. H. V. Winkle, M. W. Davidson, W. X. Chen, and R. L. Rill. Cholesteric helical pitch of near persistence length DNA. *Macromolecules*, 23:4140–4148, 1990.

[24] V. V. Rybenkov, N. R. Cozzarelli, and A. V. Volgodskii. Probability of DNA knotting and the effective diameter of the DNA double helix. *Proceedings of the National Academy of Sciences of the United States of America*, 90:5307–5311, 1993.

[25] J. R. C. van der Maarel and K. Kassapidou. Structure of short DNA fragment solutions. *Macromolecules*, 31:5734–5739, 1998.

[26] K. T. Nguyen, F. Sciortino, and C. De Michele. Self-assembly-driven nematization. *Langmuir*, 30:4814–4819, 2014.

[27] C. De Michele, T. Bellini, and F. Sciortino. Self-assembly of bifunctional patchy particles with anisotropic shape into polymers chains: Theory, simulations, and experiments. *Macromolecules*, 45:1090–1106, 2012.

[28] A. De Vries. X-ray Photographic Studies of Liquid Crystals I. A Cybotactic Nematic Phase. *Molecular Crystals and Liquid Crystals*, 10:219–236, 1970.

[29] A. De Vries. Microscopic structure of mesomorphic phases, experimental investigations of the structure of thermotropic liquid crystals. *Journal de Physique Colloques*, 36:C1–1 – C1–11, 1975.

[30] L. V. Azároff and C. A. Schuman. X-Ray Diffraction by Cybotactic Nematics. *Molecular Crystals and Liquid Crystals*, 122:309–319, 1985.

[31] O. Francescangeli and E. T. Samulski. Insights into the cybotactic nematic phase of bent-core molecules. *Soft Matter*, 6:2413–2420, 2010.

[32] C. Keith, A. Lehmann, U. Baumeister, M. Prehm, and C. Tschierske. Nematic phases of bent-core mesogens. *Soft Matter*, 6:1704–1721, 2010.

[33] O. Francescangeli, F. Vita, and E. T. Samulski. The cybotactic nematic phase of bent-core mesogens: State of the art and future developments. *Soft Matter*, 10: 7685–7691, 2014.

[34] G. Zanchetta. Spontaneous self-assembly of nucleic acids: Liquid crystal condensation of complementary sequences in mixtures of DNA and RNA oligomers. *Liquid Crystals Today*, 18:40–49, 2009.

[35] A. Casey and P. Harrowell. Monte Carlo simulations of smectic phase transitions in flexible-rigid-flexible molecules. *Journal of Chemical Physics*, 110:12183–12192, 1999.

[36] J. S. Van Duijneveldt, A. Gil-Villegas, G. Jackson, and M. P. Allen. Simulation study of the phase behavior of a primitive model for thermotropic liquid crystals: Rodlike molecules with terminal dipoles and flexible tails. *Journal of Chemical Physics*, 112:9092–9104, 2000.

[37] C. McBride and C. Vega. A Monte Carlo study of the influence of molecular flexibility on the phase diagram of a fused hard sphere model. *Journal of Chemical Physics*, 117:10370–10379, 2002.

[38] D. Düchs and D. E. Sullivan. Entropy-induced smectic phases in rod–coil copolymers. *Journal of Physics: Condensed Matter*, 14:12189, 2002.

[39] R. C. Hidalgo, D. E. Sullivan, and J. Z. Y. Chen. Smectic phases in rod–coil diblock copolymers. *Journal of Physics: Condensed Matter*, 19:376107, 2007.

Chapter 5

Self-assembly of all-DNA patchy rods

Despite significant progress in the field of DNA liquid crystals, the absence of smectic phase in stiff, sufficiently long blunt-ended dsDNA still remains an open question. One of the possible reasons why the layer-like mesophase has not yet been observed in DNA is end-to-end stacking interactions. These weak attractive forces act between blunt ends of neighboring duplexes in a solution causing them to stack on top of one another. As a consequence, polydisperse linear aggregates composed of DNA duplexes are formed which destabilize the smectic and favor the columnar phase. In this chapter, the role of blunt-end attractions in the formation of the smectic phase has been investigated. This was achieved by engineering of end-to-end stacking interactions at a molecular level. Here, DNA duplexes have been constructed containing a hairpin loop structure at one or both ends. The self-assembly of such modified DNA structures results in the formation of monolayer and bilayer smectic phase. The possibility to tune the strength of blunt-end attractions by DNA sequence modification will be addressed. The directionality of these attractions and achieved control over their existence and strength unveil the DNA as a true anisotropic patchy particle.

5.1 Introduction

In this chapter, the role of end-to-end stacking interactions in the formation of LC phases is investigated. Base-stacking interactions are non-covalent attractive interactions typical for DNA that were already described in detail in section 2.1.3. Double-helical structure and stability of DNA duplexes are strongly influenced by these attractions that arise between faces of neighboring nitrogenous bases within the DNA [1]. However, base-stacking can occur also between terminal ends of two blunt-ended DNA duplexes, in case of which we refer to them as end-to-end stacking interactions.

Recently, the importance of end-to-end stacking interactions was highlighted by various research directions. Base-stacking was shown to be an important factor in DNA replication, having a great influence on polymerase activity [2]. In the area of DNA nanotechnology, base-stacking was used as a principle to produce multimeric objects by self-assembly of three-dimensional DNA structures, on the basis of shape complementarity, without base pairing [3, 4]. End-to-end stacking interactions have also been discussed as a hypothesis for the formation of LC phases in suspensions of ultra-short DNA duplexes. Nakata et al. investigated the DNA duplexes of lengths ranging from 6 to 20 base pairs. It was found that even such ultra-short dsDNA

with aspect ratios $L/D < 3.7$ are able to undergo I to LC phase transition, at sufficiently high concentrations [5]. This is not in line with predictions from simulations on hard spherocylinders with similar L/D [6, 7]. However, end-to-end stacking interactions between blunt ends of DNA duplexes induce the formation of longer linear aggregates which are able to undergo I to LC phase transition. The importance of these attractive interactions is additionally highlighted in chapter 4 of this thesis. Due to blunt-end attractions, the folded type of *Sm-A* phase is stabilized in the system with stick-chain-stick architecture.

The above-mentioned results imply that blunt ends can be viewed as monovalent discrete attractive sites on the DNA molecule. Therefore, we might consider dsDNA a true anisotropic divalent patchy particle with attractive patches located at its blunt ends. In this chapter will be shown that the valence of patchy DNA duplexes can be controlled by a screening of end-to-end stacking interactions at one or both ends. This can be achieved as desired by slight modifications in the structure of the DNA, which would allow to engineer the interactions and thereby control the self-assembly process.

DNA fragment with length of 48 bp ($L \sim 16$ nm, assuming 0.34 nm per bp) shown in figure 5.1 a) (F-DNA) was used as a reference system. This DNA duplex is stiff ($L < L_p$, L_p of dsDNA is close to 50 nm) and has $L/D > 8$ which is above the molecular shape anisotropy criterion for the formation of N^* and Sm phases ($L/D > 3.7$, see figure 2.13). To screen the end-to-end interactions two different approaches were employed. The first approach uses short 5 T overhangs at the blunt end (F-5T-DNA) as shown in figure 5.1 b). PolyT overhangs were already shown to create a steric hindrance and disturb the end-to-end adhesion of ultra-short DNA duplexes [5, 8], as well as gapped DNA duplexes (section 4.5). The second approach uses hairpin loop structure at one (1xH-DNA, figure 5.1 c)) or both ends (2xH-DNA, figure 5.1 d)) of DNA duplexes. Intermolecular base pairing can occur in single-stranded DNA in which two complementary parts of the strand form a double-stranded structure leaving an unpaired hairpin loop at the end. This kind of structure is known as hairpin or hairpin loop, simply because it resembles commonly used tools for hair styling. Details of the synthesis are described in section 3.3.3.

Native PAGE electrophoresis of the self-assembled structures is shown in figure 5.2. There are subtle differences in the gel migration pattern of F-DNA, 1xH-DNA, 2xH-DNA, and F-5T-DNA. The presence of hairpin loops and polyT overhangs at the ends of DNA duplexes cause a slight delay in their migration in comparison to F-DNA due to their flexibility. The existence of sharp single bands and the resolved subtle differences in electrophoretic mobilities of structures presented in figure 5.1 confirm the successful synthesis.

5.2 Self-assembly of DNA duplexes with controlled end-to-end stacking interactions

Concentration-dependent SAXS profiles for F-DNA are shown in figure 5.3. The sharp intense q_{DNA} peak at the highest concentrations is related to strong positional correlations between neighboring DNA duplexes and corresponds to the formation of *Col* phase [9]. Decreasing the concentration, a broader peak arises, superimposed on the q_{DNA} peak. This suggests a possible two-phase coexistence between *Col* and another LC phase. At the concentration of 229.99 mg ml^{-1} only the broad peak remains. POM image of this sample shown on the right hand side in figure 5.3 reveals

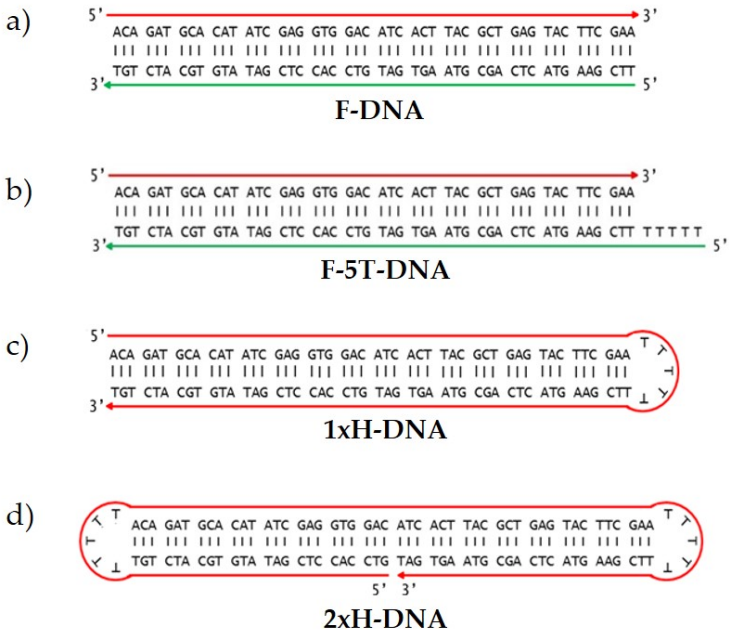

FIGURE 5.1: Schematic representation of 48 bp long DNA with a) blunt ends (F-DNA), b) 5T overhang on one end (F-5T-DNA), c) hairpin loop structure on one end (1xH-DNA), and d) hairpin loop structure on both ends (2xH-DNA). Different strands involved in the synthesis of targeted structures are represented with different colors. The sequences of the strands used for the synthesis are also shown.

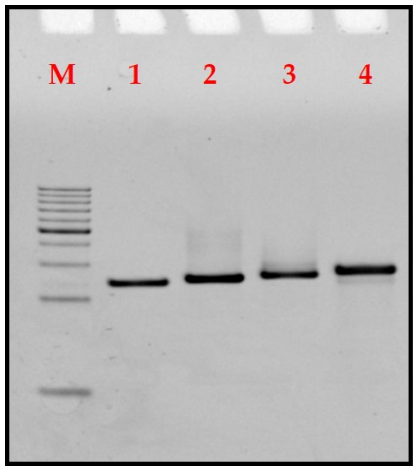

FIGURE 5.2: 10% native PAGE electrophoresis of different DNA structures. Lanes contain following samples (from left to right): **M)** 20 bp DNA ladder, each band represents DNA fragment starting from 20 bp at the bottom to 200 bp at the top, **1)** F-DNA, **2)** 1xH-DNA, **3)** 2xH-DNA, and **4)** F-5T-DNA.

the fingerprint texture typical for N^* phase. Further decrease in concentration leads to two-phase I/N^* coexistence at 184.45 mg ml^{-1}. 2D scattering pattern of the birefringent part of this sample is shown in figure 5.4 a) where a single broad ring can be seen, corresponding to the broad peak at high q values. Finally, at 177 mg ml^{-1} F-DNA undergoes a phase transition to I phase.

As expected, with increasing concentration blunt-ended dsDNA exhibits phase transitions typical for rod-like DNA: I to N^* phase transition, through I/N^* phase coexistence region, as well as phase transition to *Col* phase at higher concentrations. The phase sequence of dsDNA doesn't include *Sm* phase, which is in line with previously investigated DNA duplexes [10, 11]. Note that the fully paired analogue of G-DNA presented in the previous chapter is somewhat longer, 116 bp dsDNA, and therefore slightly more flexible than 48bp long dsDNA[1]. Therefore, the results obtained for 48 bp long F-DNA (L/L_p= 0.3) indicate that the absence of *Sm* phase is not due to the flexibility. Instead, the absence of *Sm* phase in dsDNA could be attributed to the formation of polydisperse aggregates as a result of attractive end-to-end stacking interactions, similarly to ultra-short DNA duplexes [12, 5]. Therefore, disabling the ability of dsDNA to form such molecular aggregates via end-to-end stacking interactions is expected to promote the formation of a *Sm* phase. To this end, phase behavior of F-5T-DNA, 1xH-DNA and 2xH-DNA was investigated.

The SAXS profiles of F-5T-DNA are shown in figure 5.5. The phase transitions observed in this system are the same as those in F-DNA, with a slight shift in the concentrations of phase boundaries, while the *Sm* phase is still absent. These results demonstrate that 5T overhangs are not efficient in the screening of end-to-end stacking interactions and stabilization of *Sm* phase. In contrast, DNA structures with hairpin loop were found to be efficient in suppressing of end-to-end stacking.

SAXS measurements were performed on a series of 1xH-DNA samples and are shown in figure 5.6. At the concentration of 310.55 mg ml^{-1} an intense principal peak at the q^* position, followed by another one at the position $2q^*$ can be seen. This is clear evidence for the formation of a layer-like mesophase. Sharp intense q_{DNA} peak indicates strong positional correlations between neighboring duplexes within the smectic structure. The type of *Sm* phase was determined by the observation of X-ray scattering pattern of shear-aligned 1xH-DNA shown in figure 5.7 a). The relative orientation of the inner and outer arcs together with the sharpness of the q_{DNA} suggest the formation of *Sm-B* phase. The length of smectic layers for the smectic phase formed at 310.55 mg ml^{-1} is calculated as $2\pi/q^*$= 34 nm which is approximately equal to two lengths of 1xH-DNA duplexes. This smectic layering clearly suggests that each layer consists of two molecules stacked on top of one another, due to end-to-end stacking (see the schematic representation on the right-hand side of the upper panel in figure 5.6). Since the duplexes are *protected* only at one blunt end, no further stacking is possible and molecular aggregates consisting of exclusively two molecules are formed. At slightly lower concentration of 300.21 mg ml^{-1}, another broad peak superimposed on the sharp q_{DNA} peak can be observed. The conjunction of these two peaks might appear due to the phase coexistence of *Sm-B* and another LC phase.

Decreasing the concentration to 290.34 mg ml^{-1} leads to disappearance of the smectic peaks, while only broad q_{DNA} remains. The sample is still birefringent when observed under crossed polarizers as can be seen from the inset in the third panel of figure 5.6. The effect of the further decrease in the concentration down to I/LC

[1] Both DNA duplexes are still considered as rods since their contour length is shorter than their persistence length.

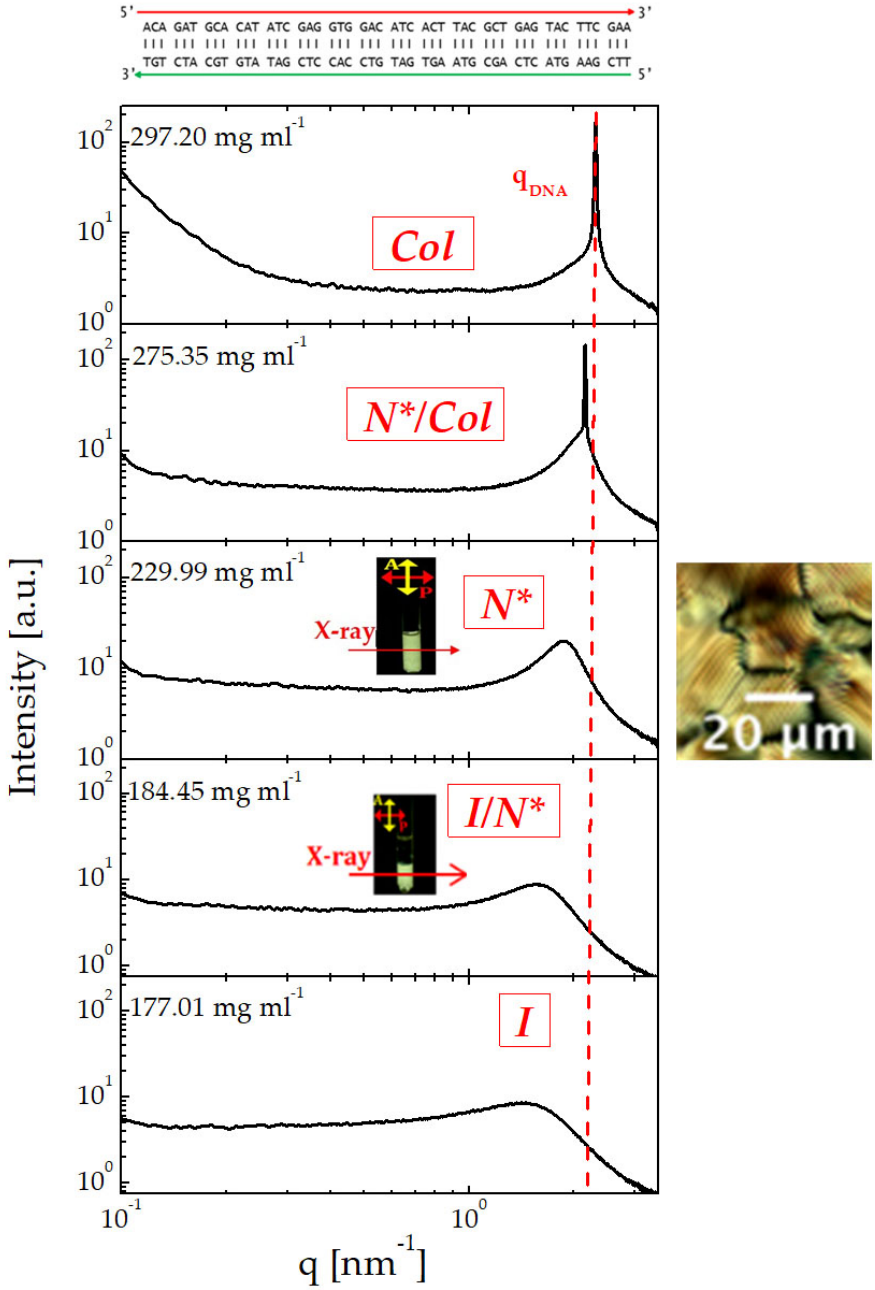

FIGURE 5.3: X-ray scattering patterns of 48 bp long F-DNA at concentrations (from top to the bottom) c = 297.2, 275.35, 229.99, 184.45, and 177.01 mg ml^{-1}. POM micrograph with typical fingerprint texture of N^* phase is shown on the right-hand side.

phase coexistence region (from 290.34 to 215.42 mg ml^{-1}) is broadening of q_{DNA} peak and slight shift of its maximum to lower q values. The POM image of the two-phase coexistence sample reveals the fingerprint texture which is typical for the N^* phase. Therefore, the N^* phase persists in the concentration range between 290.34 and 224.71 mg ml^{-1}, as well as in the birefringent part of the biphasic sample at 215.42 mg ml^{-1}. Finally, below 215.42 mg ml^{-1}, the system undergoes a transition to I phase.

Screening the attractive interactions on both blunt ends of dsDNA results in 2xH-DNA duplexes. 2xH-DNA shows rather similar SAXS signature to already described

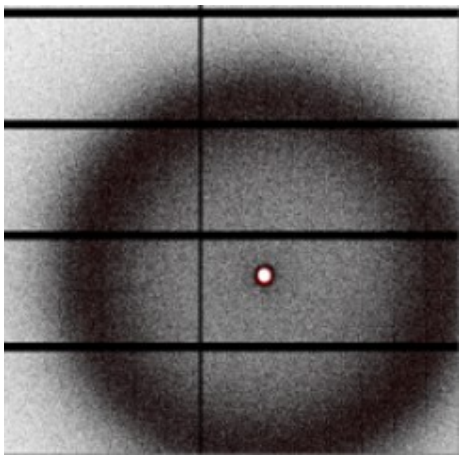

FIGURE 5.4: 2D X-ray scattering pattern of F-DNA at concentration c = 184.45 mg ml^{-1}.

1xH-DNA. Equidistant peaks at positions q^*, $2q^*$ and $3q^*$ are evidence of *Sm* phase formed at concentrations of 355.07 and 345.78 mg ml^{-1}. As in case of 1xH-DNA, the sharpness of the q_{DNA} peak and observation of 2D scattering pattern of shear-aligned sample (figure 5.7) clearly suggest the formation of *Sm-B* phase. However, equidistant smectic peaks at the highest concentration are shifted to higher q values comparing to 1xH-DNA. The smectic layering calculated from the position of the principal peak q^* is approximately 17 nm. This value is exactly half of the value for 1xH-DNA and corresponds to one molecular length of 2xH-DNA. The packing scenario for the *Sm-B* phase is schematically presented in the right-hand side of the top panel in figure 5.8. The layers are built from single 2xH-DNA duplexes. The results indicate that the hairpin loop located at both blunt ends of DNA duplex acts as a switch which turns-off the attractive end-to-end stacking interactions, and therefore no molecular aggregates can be formed.

Sm-B phase persists until the concentration is decreased to 335.03 mg ml^{-1}, when another broader peak appears around the position of q_{DNA} sharp peak. This indicates a phase coexistence region of *Sm-B* and *N** phase. The identification of the *N** was verified by SAXS profiles at concentrations of 325.38 and 309.57 mg ml^{-1} and fingerprint texture in the POM image of the sample at 309.57 mg ml^{-1}. At even lower concentrations, *I/N** phase coexistence occurs, and finally below 262.21 mg ml^{-1} the sample is in a disordered *I* phase.

The reported results on the self-assembly of F-DNA, 1xH-DNA, and 2xH-DNA duplex are summarized in a phase diagram shown in figure 5.9. F-5T-DNA was found to be inefficient in the screening of end-to-end interactions and therefore, it is omitted from this phase diagram. In general, disruption of end-to-end stacking interactions shifts all phase boundaries to higher DNA concentrations. This difference arises from disparities in the valence of attractive sites on DNA duplexes. Usually, the width of a phase coexistence region provides information about the polydispersity in the system. More polydisperse systems exhibit wider *I/N** phase coexistence regions [13]. Although the DNA systems presented in this thesis are monodisperse in length, there is still a certain degree of polydispersity due to blunt end attractions. F-DNA has both blunt ends accessible for end-to-end stacking, and therefore, long linear polydisperse aggregates are formed. In the case of 1xH-DNA duplexes end-to-end stacking is possible only on one side of the duplexes, which limits the

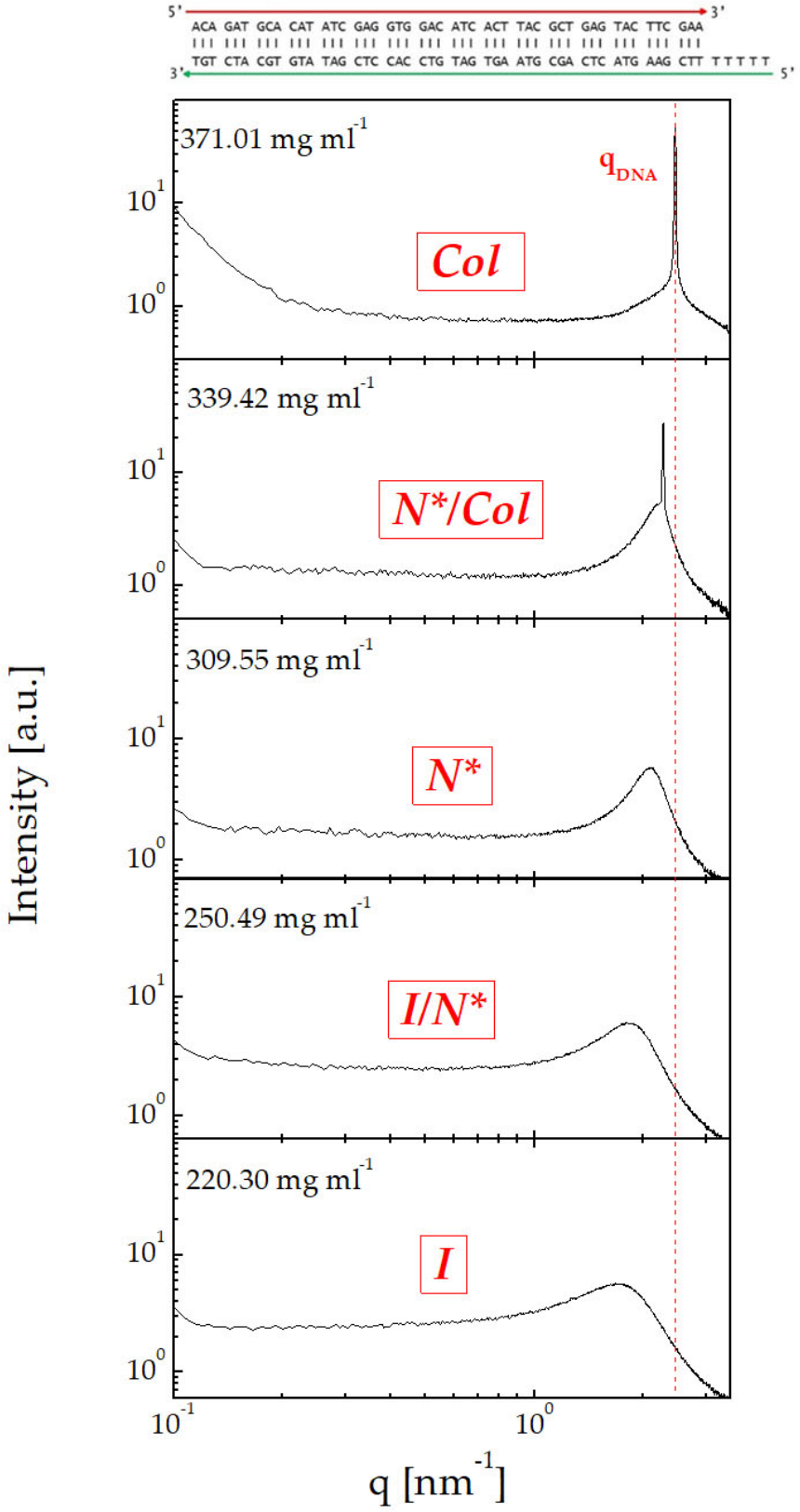

FIGURE 5.5: X-ray scattering profiles of F-5T-DNA at concentrations (from top to the bottom) c = 371.01, 339.42, 309.55, 250.49, and 220.3 mg ml^{-1}.

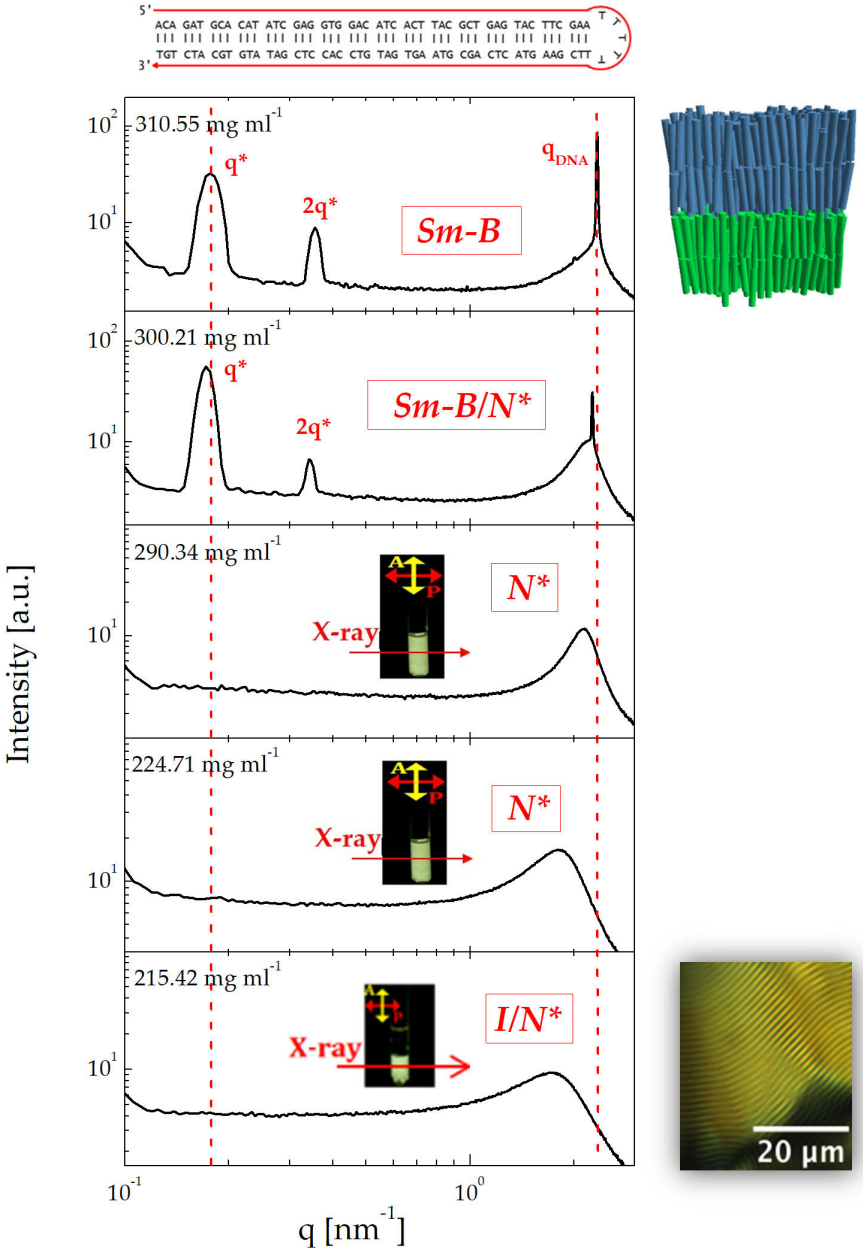

FIGURE 5.6: X-ray scattering profiles of 1xH-DNA at concentrations (from top to the bottom) c = 310.55, 300.21, 290.34, 224.71, and 215.42 mg ml^{-1}. Schematic representation of *Sm-B* is shown on the right-hand side of the top panel. Different colors mark distinct layers building the *Sm-B* phase. On the right-hand side of the bottom panel POM image of the biphasic sample with characteristic fingerprint texture is shown.

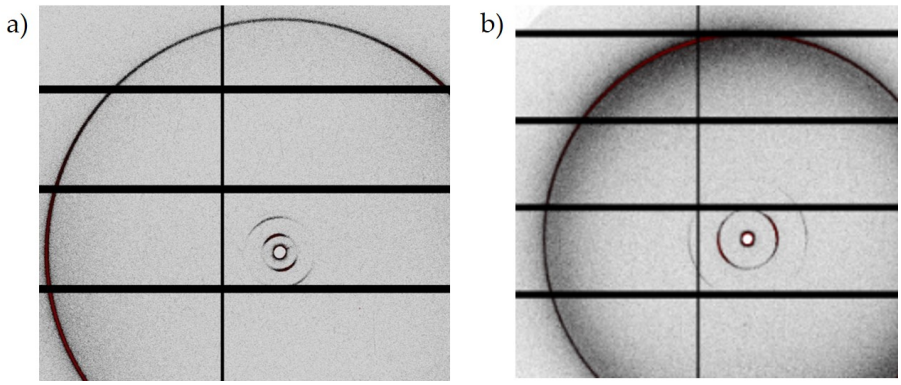

FIGURE 5.7: 2D X-ray scattering pattern of a) 1xH-DNA at concentration c = 310.55 mg ml^{-1} and b) 2xH-DNA at concentration c = 355.1 mg ml^{-1}.

formation of aggregates to dimers only. No end-to-end stacking interactions are possible in case of 2xH-DNA. This polydispersity effect can be clearly seen in the phase diagram by observing the width of the *I/N** phase coexistence region marked with green. Finally, the width of the *N** phase region appears narrower in case of 2xH-DNA duplexes, comparing to 1xH-DNA. This suggests that the *Sm* phase can be stabilized more easily in 2xH-DNA. As already described, the main differences in the *Sm* phases formed by 1xH-DNA and 2xH-DNA duplexes lie in the molecular arrangement within the layers. The smectic layers of 1xH-DNA consist of dimers. Therefore, there is a certain degree of flexibility introduced at the contact point between two 1xH-DNA duplexes building a dimer. The locally introduced flexibility can act destabilizing on the *Sm* phase. The role of flexibility in the destabilization of *Sm*, as well as its effect on widening of the *I/N* phase coexistence, was already addressed in experimental [14] and theoretical studies [15, 16, 17, 18].

5.3 Role of end-to-end stacking strength in the self-assembly of 1xH-DNA

Base stacking is a complex type of interaction and depends on many factors. Th geometry of the nitrogenous bases, electric forces arising between charges within them, and hydrophobicity of the planar aromatic bases make these interactions also sequence-dependent. It has been shown by existing experimental studies that stacking of G-C and C-G pairs is stronger than stacking between A-T T-A pairs [19, 20]. Therefore, it might be interesting to investigate whether modifying the sequence at the blunt end of the 1xH-DNA duplex can influence its self-assembly behavior. 1xH-DNA presented earlier in this chapter is terminated with A-T bp. Thus, 1xH-DNA duplex having G-C bp at the blunt end was additionally synthesized. This system will be referred to as 1x-DNA-GC.

Concentration-dependent phase diagram based on SAXS results, POM images and visual observation of samples under crossed polarizers is shown in figure 5.10 for 1xH-DNA and 1xH-DNA-GC. In both systems, the same sequence of phases is found with increasing concentration: *I*, textitI/N*, *N** and *Sm-B* phase in which layers are composed of dimers. It can be seen that the 1xH-DNA-GC forms *Sm-B* phase at the slightly lower concentration than 1xH-DNA. Another interesting difference

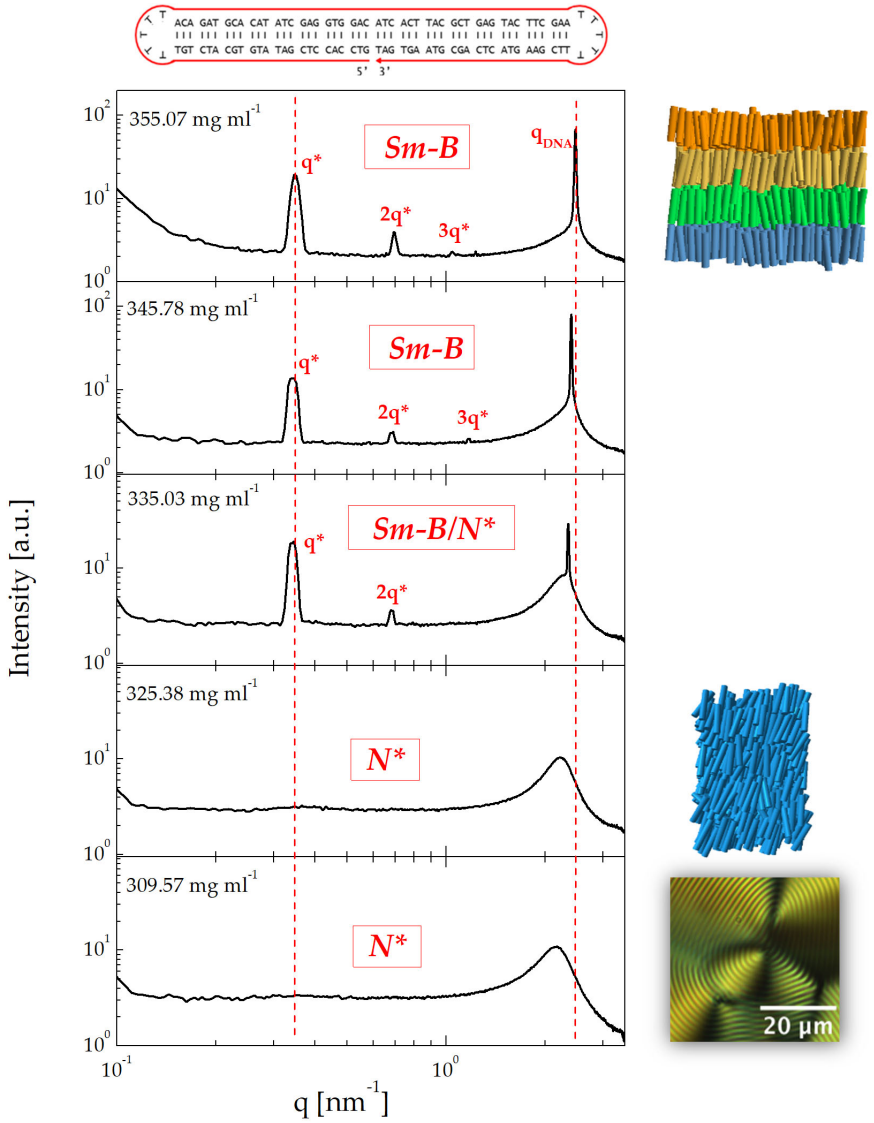

FIGURE 5.8: X-ray scattering profiles of 2xH-DNA at concentrations (from top to the bottom) c = 355.07, 345.78, 335.03, 325.38, and 309.57 mg ml^{-1}. Schematic representation of *Sm-B* is shown on the right-hand side of the top panel. Different colors mark distinct layers building the *Sm-B* phase. Schematic representation of N^* is shown on the right-hand side of the panel with SAXS profile corresponding to concentration of 325.38 mg ml^{-1}. The chiral nature of the N^* is not shown for simplicity. On the right-hand side of the bottom panel POM image of the biphasic sample with characteristic fingerprint texture is shown

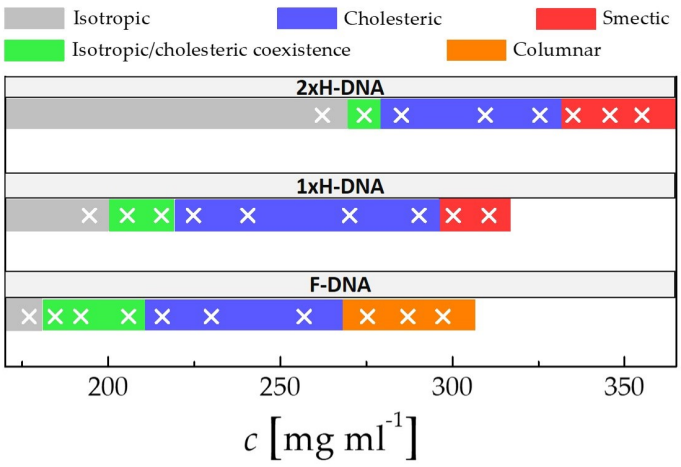

FIGURE 5.9: Phase diagram comparing dsDNA with no hairpins, 1xH-DNA and 2x-DNA.

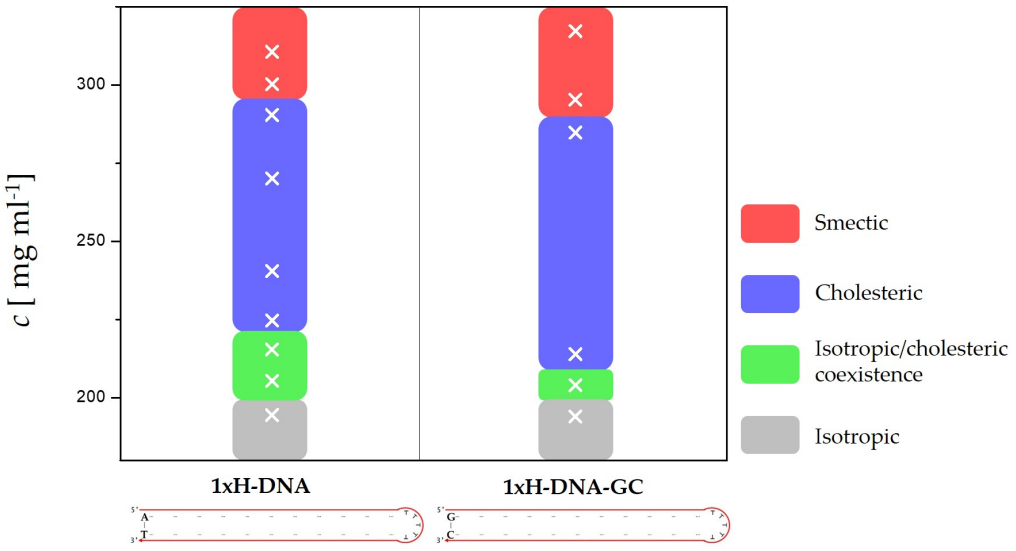

FIGURE 5.10: Concentration-dependent phase diagram comparing 1xH-DNA (A-T terminated) and 1xH-DNA-GC.

is the noticeable shrinkage of the I/N* phase coexistence region in 1xH-GC-DNA. Both effects can be understood in terms of flexibility. The stronger stacking attractions between faces of terminal bases allow less flexibility at the contact point of two rods. Nevertheless, the effects observed are rather small so it could be interesting to explore further modifications, such as artificially synthesized nitrogenous bases that don't occur naturally in DNA. This could lead to stronger or weaker attractions between blunt ends of adjacent duplexes, depending on the structure of used nitrogenous bases. The difference in stacking energies of natural and artificial aromatic compounds was already demonstrated for short DNA duplexes having G-C pair at the blunt end [21, 2]. However, in order to achieve the fine-tuning of end-to-end stacking interactions with this approach further studies are necessary.

5.4 Summary and conclusions

For decades now, the importance of base-stacking interactions was in the shadow of hydrogen bonding, which is crucial for molecular recognition and specificity of Watson-Crick base pairing in DNA. Base-stacking, however, although not ensuring specificity, plays an important role in stabilization of DNA structure and in its self-assembly processes.

In this chapter, it was shown that control over end-to-end stacking interactions between blunt ends of DNA duplexes can significantly alter their self-assembly behavior. The control was achieved by modifying the blunt ends of DNA duplexes with polyT overhangs and hairpin loop structure. Unlike polyT overhangs, the hairpin loop was found to be an efficient way to disrupt end-to-end stacking interactions. Selective screening of attractions at one or both blunt ends of DNA duplexes stabilizes the formation of bilayer and monolayer *Sm-B* phase, respectively. These findings offer an answer to a longstanding mystery related to the absence of *Sm* phase in ds-DNA. Additionally, the results presented highlight the anisotropic patchy character of stiff DNA duplexes. The interaction strength control between attractive patches of 1xH-DNA was limited due to difficulties related to DNA synthesis. However, due to the simplicity of interaction potential alterations, MC simulations could allow a systematic investigation of the role of end-to-end stacking strength in the self-assembly of 1xH-DNA. This can be achieved by employing similar coarse-grained model [22, 5] as in case of ultra-short DNA duplexes. The presented work could open a pathway to a re-examination of the phase diagram for short DNA duplexes with $L \leq L_p$.

Bibliography

[1] A. A. Travers, C.R. Calladine, H. R. Drew, and B. Luisi. *Understanding DNA*. Elsevier, 2004.

[2] E. T. Kool. Hydrogen bonding, base stacking, and steric effects in DNA replication. *Annual Review of Biochemistry and Biomolecular structure*, 30:1–22, 2001.

[3] S. Woo and P. W. K. Rothemund. Programmable molecular recognition based on the geometry of DNA nanostructures. *Nature Chemistry*, 3:620–627, 2011.

[4] T. Gerling, K. F. Wagenbauer, A. M. Neuner, and H. Dietz. Dynamic DNA devices and assemblies formed by shape-complementary, non-base pairing 3D components. *Science*, 347:1446–1452, 2015.

[5] M. Nakata, G. Zanchetta, B. D. Chapman, C. D. Jones, J. O. Cross, R. Pindak, T Bellini, and N a Clark. End-To-End Stacking and Liquid Crystal Formation of 6- to 20-Base Pair DNA Duplexes. *Science*, 318:1–4, 2007.

[6] S. C. McGrother, D. C. Williamson, and G. Jackson. A re-examination of the phase diagram of hard spherocylinders. *Journal of Chemical Physics*, 104:6755–6771, 1996.

[7] P. Bolhuis and D. Frenkel. Tracing the phase boundaries of hard spherocylinders. *The Journal of Chemical Physics*, 106:666–687, 1997.

[8] G. Zanchetta. Spontaneous self-assembly of nucleic acids: Liquid crystal condensation of complementary sequences in mixtures of DNA and RNA oligomers. *Liquid Crystals Today*, 18:40–49, 2009.

[9] D. Durand, J. Doucet, and F. Livolant. A study of the structure of highly concentrated phases of DNA by X-ray diffraction. *Journal De Physique Ii*, 2:1769–1783, 1992.

[10] F. Livolant and A. Leforestier. Condensed phases of DNA: structures and phase transitions. *Prog. Polym. Sci.*, 21:1115–1164, 1996.

[11] M. Salamonczyk, J. Zhang, G. Portale, C. Zhu, E. Kentzinger, J. T. Gleeson, A. Jakli, C. De Michele, J. K.G. Dhont, S. Sprunt, and E. Stiakakis. Smectic phase in suspensions of gapped DNA duplexes. *Nature Communications*, 7:1–9, 2016.

[12] A. M. Bohle, R. Hołyst, and T. Vilgis. Polydispersity and Ordered Phases in Solutions of Rodlike Macromolecules. *Physical Review Letters*, 76:1396–1399, 1996.

[13] K. Merchant and R. L. Rill. DNA length and concentration dependencies of anisotropic phase transitions of DNA solutions. *Biophysical Journal*, 73:3154–3163, 1997.

[14] E. Pouget, E. Grelet, and M. P. Lettinga. Dynamics in the smectic phase of stiff viral rods. *Physical Review E - Statistical, Nonlinear, and Soft Matter Physics*, 84: 1–6, 2011.

[15] M. Dijkstra and D. Frenkel. Simulation study of the isotropic-to-nematic transitions of semiflexible polymers. 51:5891–5898, 1995.

[16] Z. Y. Chen. Nematic Ordering in Semiflexible Polymer Chains. *Macromolecules*, 26:3419–3423, 1993.

[17] A. R. Khokhlov and A. N. Semenov. Liquid-crystalline ordering in the solution of long persistent chains. *Physica A: Statistical Mechanics and its Applications*, 108: 546–556, 1981.

[18] A. R. Khokhlov and A. N. Semenov. Liquid-crystalline ordering in the soluton of partially flexible macromolecules. *Physica A: Statistical Mechanics and its Applications*, 112A:605–614, 1982.

[19] E. Protozanova, P. Yakovchuk, and M. D. Frank-Kamenetskii. Stacked-unstacked equilibrium at the nick site of DNA. *Journal of Molecular Biology*, 342:775–785, 2004.

[20] P. Yakovchuk, E. Protozanova, and M. D. Frank-Kamenetskii. Base-stacking and base-pairing contributions into thermal stability of the DNA double helix. *Nucleic Acids Research*, 34:564–574, 2006.

[21] K. M. Guckian, B. A. Schweitzer, R. X. F. Ren, C. J. Sheils, D. C. Tahmassebi, and E.T. Kool. Factors contributing to aromatic stacking in water: Evaluation in the context of DNA. *Journal of the American Chemical Society*, 122:2213–2222, 2000.

[22] C. De Michele, T. Bellini, and F. Sciortino. Self-assembly of bifunctional patchy particles with anisotropic shape into polymers chains: Theory, simulations, and experiments. *Macromolecules*, 45:1090–1106, 2012.

Chapter 6

Stimuli-responsive hierarchical self-assemblies of DNA-polymer hybrids

In this chapter, a hybrid DNA self-assembly concept will be presented inspired by the hierarchical self-assembly concept with block copolymers and lyotropic liquid crystals. Exploiting the unique DNA's physicochemical properties, a novel family of DNA-polymer hybrids is constructed, consisting of a charged rod-like DNA block and a neutral temperature-responsive flexible polymeric block that are covalently connected. Due to the combination of distinct blocks in the system, it is possible to reversibly switch between a disordered ensemble and different multidimensional nanostructures of increasing complexity by changing the temperature. SAXS measurements have been carried out in concentrated aqueous solutions of DNA-polymer hybrids and revealed phases with rich morphological diversity, ranging from lamellar to cubic network structures.

6.1 Introduction

Block copolymers are known to exhibit a long-range order in one, two, and three dimensions through the microphase separation [2] of covalently connected blocks with chemical dissimilarity. This is a well-established bottom-up self-assembly method for the formation of complex structures with long-range order at length scales of several tens to hundreds of nanometers. Another self-assembly method, widely used in the field of DNA nanotechnology and based on Watson-Crick base pairing, leads not only to the formation of complex structures but also offers programmability [37, 38, 34]. However, fabrication of complex all-DNA structures requires a large number of DNA strands with a unique sequence. This can be an issue for the establishment of long-range order in final products. Therefore, taking the best of both worlds seems like an optimal way to approach the programmable fabrication of complex structures while minimizing the structural errors of the products. The application of such combined approach results in a new type of DNA-polymer nanostructures which will be presented in this chapter.

Fabrication of DNA-polymer hybrids unites the two distinct self-assembly pathways in order to yield DNA-based soft materials which can overcome the above mentioned limitations. Up to now, this kind of approach was limited to the construction of micelles [25, 6, 18], vesicles [42], nanotubes [4], and ordered nanofibers [3] from DNA-polymer or three-dimensional DNA nanostructures-polymer hybrids

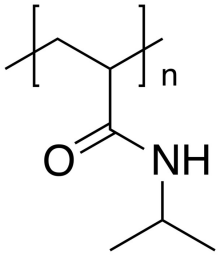

FIGURE 6.1: Chemical structure of N-isopropylacrylamide (PNIPAm).

[23, 31]. However, no multidimensional arrangement of DNA blocks was achieved so far.

In this chapter, fabrication of DNA-polymer particles based on a combination of DNA sequence-specific binding properties (Watson-Crick base pairing) [45] and copper-free click chemistry [1] will be demonstrated. In general, the DNA-polymer hybrids consist of a charged stiff DNA fragment (D-block) and a neutral temperature-responsive polymeric segment (P-block) which are covalently connected. The P-blocks attached to rod-like DNA act as soft patches for which shape and position fluctuations are possible. The DNA-polymer hybrids fabricated in this way are anisotropic in shape and exhibit directionality in interactions with the environment. Such anisotropy in interactions is typical for patchy particles.

Temperature-responsive polymer N-isopropylacrylamide (PNIPAm) is the P-block in DNA-polymer hybrids. PNIPAm is amphiphilic polymer whose chemical structure is shown in figure 6.1. It possesses hydrophilic acrylamide functional group and carbon-rich hydrophobic isopropyl group. The interesting property of this polymer is its lower critical solution temperature (LCST) behavior in water at approximately 32 °C, depending on degree of polymerization, polydispersity, branching, polymer composition, and architecture. Below this temperature, PNIPAm is very well soluble in water, while above LCST it undergoes a reversible collapse transition. In DNA-polymer hybrids, temperature-responsive behavior of PNIPAm allows us to subtly tune the amphiphilicity of the system by changing the temperature. This results with novel reversible DNA self-assembly pathways, as will be demonstrated in this chapter.

Double-stranded DNA can be covalently connected with PNIPAm by employing the concept of click chemistry, according to the protocol described in section 3.3.3. Three different architectures of DNA-polymer hybrids will be presented and discussed in this chapter. It will be shown that the synthetic approach used can be generally applied to any kind of all-DNA architecture desired. First, linear-shaped DNA-polymer (L-DNA) hybrids will be presented, consisting simply of rod-like DNA and PNIPAm attached at the ends of the duplex, as shown in figure 6.2 a). By positioning polymeric patches away from the ends of the duplex, only few bases towards the inside of the DNA, we obtain a DNA-polymeric hybrid that resembles Greek letter Π, Pi-shaped DNA-polymer (Π-DNA) hybrids (figure 6.2 b)). Finally, three-armed DNA (Y-DNA) functionalized with three polymeric patches will also be presented (figure 6.2 c)). The junction structure of Y-DNA allows a certain degree of flexibility in the junction point, while each arm is 13 base pairs (bp) long stiff double-stranded DNA [20, 43].

The success of such synthetic approach applied to different architectures of DNA

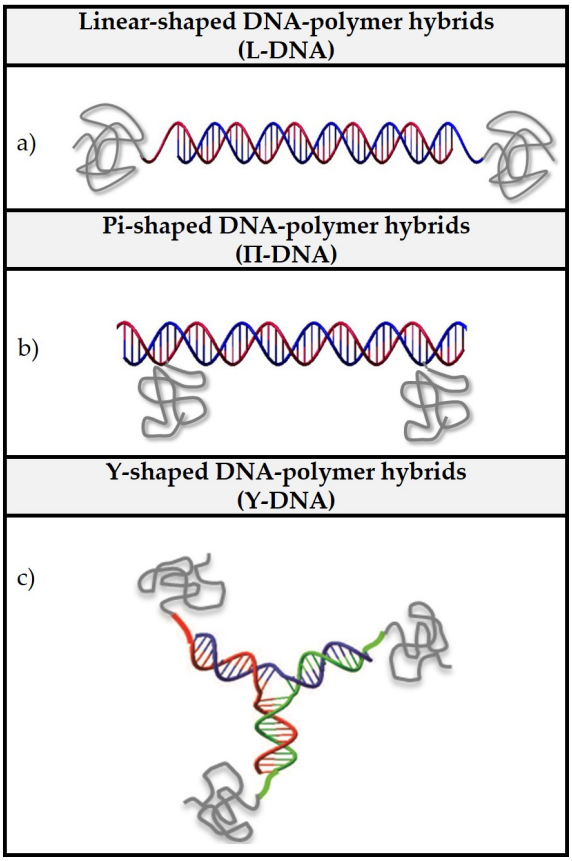

FIGURE 6.2: Schematic representation of DNA-polymer hybrids with different geometries: a) linear-shaped with PINIPAm on both ends, b) Pi-shaped with PNIPAm on both ends, and c) Y-shaped with PNIPAm on all three ends.

structures was evaluated using gel electrophoresis. The basic principles of gel electrophoresis are described in the section 3.1.4. Figure 6.3 shows the images of agarose gel electrophoresis for L-DNA hybrids (6.3 a)) and Π-DNA hybrids (6.3 b)), respectively. Based on the migration patterns, this method can successfully identify unmodified (lane 1), one-end modified (lane 2) and two-ends modified DNA duplex (lane 3). DNA duplexes that carry polymeric patches have higher mass/charge ratio and migrate through the gel matrix more slowly in comparison to unmodified DNA duplex. For the same reason, two-ends modified DNA is delayed in comparison with only one-end modified duplex. Apart from one-end modified DNA duplex, lane 2 in both images contains a small amount of unreacted unmodified DNA. This demonstrates how we can conclusively differentiate between DNA duplex alone and different degrees of modification, as well as identify an incomplete modification of the sample in which unreacted DNA is present.

Similarly, electrophoresis images for the Y-DNA hybrids are displayed in figure 6.4 for two different molecular weights of the P-block. Since Y-shaped constructs have three sites accessible to polymer, four lanes showing different degree of modification can be seen starting from Y-shaped DNA alone (lane 1), through one-arm modified (lane 2) and two-arms modified DNA (lane 3), to three-arms modified DNA (lane 4). All bands corresponding to Y-shaped constructs are clearly separated, and can be distinguished from one another.

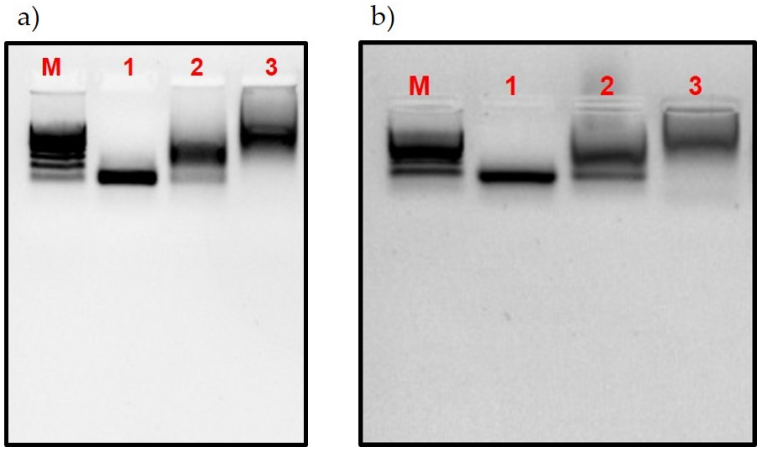

FIGURE 6.3: a) Agarose gel 3% electrophoresis of the linear-shaped DNA-polymer hybrids assembly. Lanes contain following samples: **M)** 50 bp double-stranded DNA ladder; **1)** 48 bp DNA duplex with no polymer attached; **2)** 48 bp DNA duplex with PNIPAm covalently attached on one side; **3)** 48 bp DNA duplex with PNIPAm covalently attached on both sides of the duplex. b) Agarose gel 3% electrophoresis of the Pi-shaped DNA-polymer hybrids assembly. Lanes contain following samples: **M)** 50 bp double-stranded DNA ladder; **1)** 48 bp DNA duplex with no polymer attached; **2)** 48 bp DNA duplex with PNIPAm covalently attached on one side; **3)** 48 bp DNA duplex with PNIPAm covalently attached on both sides of the duplex. Molecular weight of PNIPAm is 19 kDa.

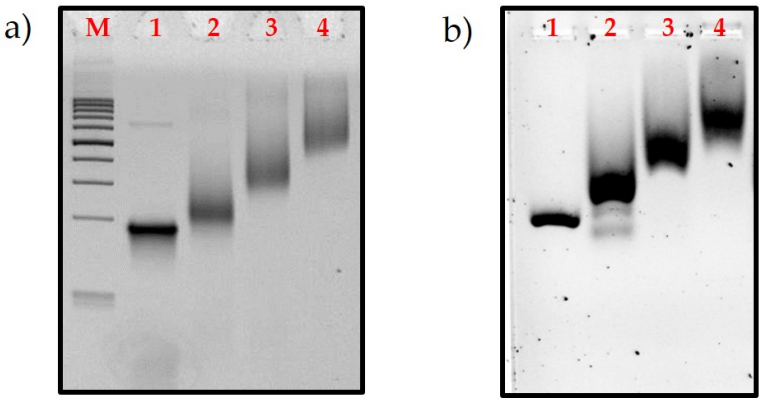

FIGURE 6.4: PAGE 15% of the star-shaped DNA-polymer hybrids assembly. Lanes contain following samples: **M)** 50 bp double-stranded DNA ladder; **1)** unmodified Y-DNA; **2)** Y-DNA with PNIPAm covalently attached to one arm; **3)** Y-DNA with PNIPAm covalently attached to two arms, **4)** Y-DNA with PNIPAm covalently attached to three arms of the structure. Molecular weight of PNIPAm is a) 1.7 kDa and b) 19 kDa.

DNA-polymer hybrids presented in this chapter share many similarities with the conventional block copolymers. Therefore, their self-assembly processes are expected to be driven by the same physical principles. In both systems, there is a compromise between the enthalpic and entropic contribution to the system's free energy. More specific, the compromise is between minimizing the unfavorable contacts of the incompatible blocks and maximizing the configurational entropy of the system. However, the distinctive combination of D-block and P-block introduces additional contributions to the system's free energy. First of all, at sufficiently high concentrations the D-blocks undergo entropy-driven transition from isotropic (I) to liquid crystalline phase [33, 40, 26]. Second, charge disparities are present between negatively charged D-block, and neutral P-block. Therefore, additional contribution related to the entropy of counterions comes into play [39, 47]. Finally, the differences in the chemical nature of the blocks and temperature-responsive nature of the P-block result in the temperature-dependent amphiphilic character of the system. This means that simply by changing the temperature in the system, we can tune the degree of incompatibility between distinct blocks and therefore, tune the enthalpic contribution to the free energy of the system.

6.2 Self-assembly of polymer-functionalized DNA nanorods

The contour length of the D-block used to make L-DNA is 16.5 nm (48 bp with 0.34 nm per bp). Concentration-dependent phase behavior of the D-block with no modification at 4 °C was investigated by SAXS and is shown in figure 6.5 a). The system displays the sequence of liquid crystal (LC) phases already observed in slightly polydisperse dsDNA of lengths below its persistence length[1] [28]. Sharp Bragg reflection (q_{DNA} peak) at DNA concentration way above the transition from I to LC phase (278 mg ml^{-1}) indicates strong positional correlations between neighboring helices and reveals the formation of columnar (Col) phase at DNA concentration of 278.0 mg ml^{-1} [9]. Assuming the local hexagonal packing, the position of the peak at q= 2.3 nm^{-1} corresponds to an interaxial helical distance $d = 4\pi/\sqrt{3}q$= 3.64 nm. The sharp peak shifts to lower q values and broadens out upon lowering the concentration down to DNA concentration of 238.0 mg ml^{-1}. Observation of the sample under crossed polarizers shows the birefringence which indicates the phase transition from I to a LC phase. This LC phase is chiral nematic (N*), as already shown in the chapter 5. The I/N^* two-phase coexistence region persists in the concentration range between approx. 180 and 190 mg ml^{-1}, as can be seen from the visual observation of samples between crossed polarizers (figure 6.5 b)). The phase coexistence region is rather narrow due to monodispersity of the D-block. Finally, the sample becomes fully dark between crossed polarizers at 171.0 mg ml^{-1}, which means that the system undergoes a transition to I phase.

Attaching PNIPAm on both sides of the D-block results in very different phase behavior. Already at concentrations way below critical concentration ($c_{LC} \sim$ 195 mg ml^{-1}) at which unmodified DNA forms LC phases, L-DNA hybrids observed between crossed polarizers show birefringent pattern, i.e. the formation of LC phases. Figure 6.6 a) shows the scattering profiles of L-DNA at 4 °C and DNA concentration of 163.0 mg ml^{-1}. The SAXS profile of D-block represented by the blue dashed line shows only a broad q_{DNA} peak. The sample is in I phase, below the I/N^* transition, as can be seen from the absence of birefringence shown in the figure 6.5 b). However,

[1] The persistence length of dsDNA is around 50 nm.

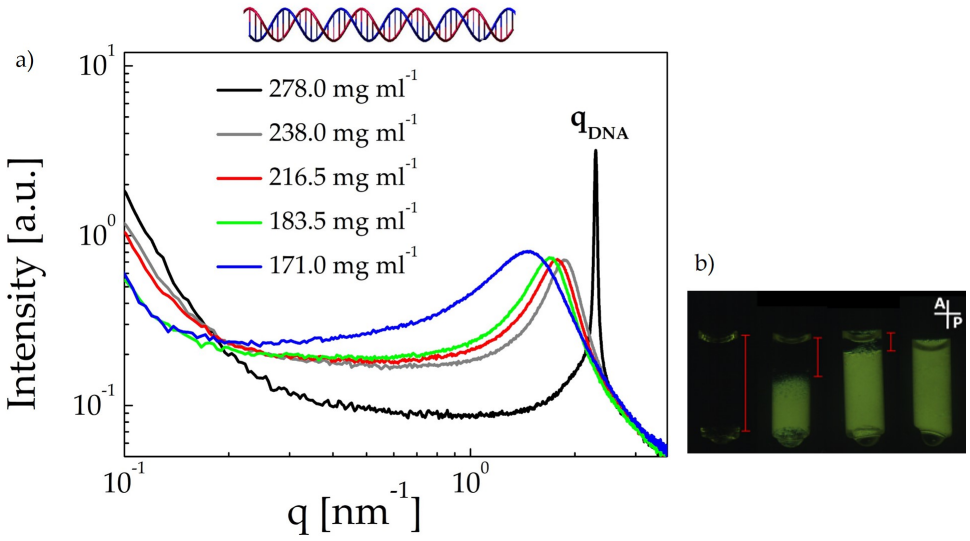

FIGURE 6.5: a) SAXS profiles for different concentrations of dsDNA at 4 °C, and b) dsDNA at different concentrations observed between crossed polarizers, from left to right: c= 171.0, 183.5, 190.0, and 206.0 mg ml^{-1}. The red bars indicate the height of the isotropic region in the sample.

L-DNA shows a sharp principle peak q^* followed by few more weaker peaks at positions of wave vector q in ratios q/q^*= 2, 3, and 4 suggest the formation of lamellar phase. The primary peak position gives us an information about the lamellar spacing $d = 2\pi/q^*$= 28 nm. The sharp q_{DNA} peak that clearly shifts to higher q values in comparison to unmodified DNA duplex at similar concentration indicates strong positional correlations between neighboring D-blocks within the lamellar phase.

More details about the molecular arrangement within the lamellar phase can be obtained by investigating a shear-aligned sample[2]. The 2D scattering pattern of shear-aligned sample is shown in figure 6.6 b). The broad outer arc in the scattering pattern corresponds to the q_{DNA} peak. It is connected with positional correlations between helices (D-blocks). The inner arcs originate from correlations in length between D-blocks and are related to the lamellar morphology. The outer and the inner arcs are in perpendicular position relative to each other. This clearly tells us that the system forms lamellar phase with D-blocks oriented with their long axes parallel to the layer normal, i.e. *Sm-A* LC phase. The sharpness of the q_{DNA} peak suggests a significant degree of order within the lamellar layers. The schematic representation of a packing scenario for this lamellar phase is shown in figure 6.6 c). The DNA-polymer hybrids are in an upright position and are packed in a hexagonal manner within the layers. This kind of phase is commonly referred to as *Sm-B* phase.

1D-SAXS profiles were analyzed in collaboration with Giuseppe Portale (University of Groningen). The peaks at lower values of scattering vector q and q_{DNA} peak were fitted at once. The total X-ray intensity scattered by a phase separated DNA-PNIPAm system as a function of the modulus of the scattering vector $q = (4\pi/\lambda)\sin\theta$ is:

$$I(q)_{tot} = I(q)_{D-P} + I(q)_{DNA} \tag{6.1}$$

[2]Shear was applied by centrifugation of the sample along the walls of the capillaries.

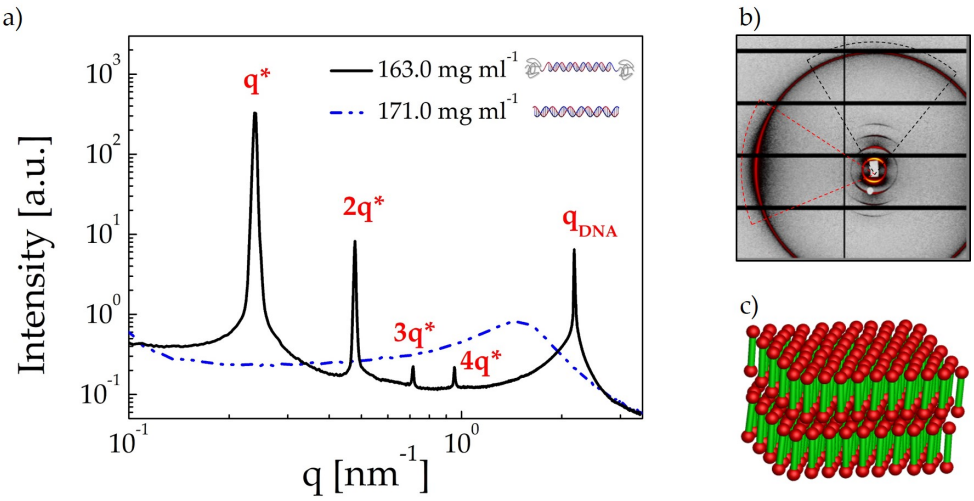

FIGURE 6.6: a) SAXS profile of L-DNA at concentration c= 163.0 mg ml^{-1} (black solid line, molecular weight of PNIPAm is 19 kDa) and SAXS profle of D-block with no modification at concetration c= 171.0 mg ml^{-1} (blue dashed line), b) scattering pattern of shear-aligned sample showing the relative positions of the arcs, and c) schematic representation of Sm-B phase formed. The D-blocks are represented with green sticks, and the P-blocks with red spheres.

where $I(q)_{D\text{-}P}$ is SAXS intensity arising from the DNA-polymers hybrids domain organization and $I(q)_{DNA}$ is SAXS intensity arising from the packing of DNA helices inside of the D-block domains, corresponding to the q_{DNA} peak in 1D-SAXS profiles.

For an isotropic two-phase system, $I(q)_{D\text{-}P}$ is given by [12]:

$$I(q)_{D-P} = C(\rho_D - \rho_P)^2(\langle F(q)\rangle^2 S(q) + \langle F(q)^2\rangle - \langle F(q)\rangle^2) \tag{6.2}$$

where ρ_D and ρ_P are the electron density values for D-block and P-block, respectively, $F(q)$ is the scattering amplitude of the D-block domains, $P(q)$=$\langle F(q)\rangle^2$ is form factor, and $S(q)$ is structure factor describing the lattice formed by the domain assembly. Pre-factor C depends on the volume and numerical density of the domains, and is taken as an arbitrary constant.

For $I(q)$ the following expression was used [10]:

$$I(q)_{DNA} = B\left(\frac{1}{2\pi}\frac{\Gamma}{(q-q_{DNA})^2 + (0.5\Gamma)^2}\right)\left(\frac{J_0(qr_D)}{qr_D}\right)^2 \tag{6.3}$$

where the average distance between D-blocks is $2\pi/q_{DNA}$, the D-block correlation length describes the length scale over which the D-blocks have conserved orientation and positional order, given by $\lambda_d = 1/\Gamma$, and r_D is the radius of the DNA helix. Prefactor B is proportional to the electron density contrast within the domains and the number of D-blocks in the domain.

The experimental data suggests that the DNA domains are not exactly perfectly ordered, but instead, regions with more and less efficient packing exist. Two different intensity contributions overlap in the position of the q_{DNA} peak, a broader one and a sharper one. Therefore, two different equations have been used, accounting

for each case, $I_b(q)_{DNA}$ for the broader peak (full green line in figure 6.7), and $I_s(q)_{DNA}$ for the sharper one (dashed green line in figure 6.7). λ_d was extracted from the fit of the sharp reflection.

For the lamellar structure, $P(q)$ is the form factor of a large disc-shaped objects [22]:

$$P(q) = \frac{2\pi^2 R^2}{q^2}\left(1 - \frac{J_1(2qR)}{qR_D}\right)\left[\frac{sin(qL/2)}{qL/2}\right]^2 \tag{6.4}$$

where R is radius of the disc-like object, and L is its thickness.

The structure factor $S(q)$ is taken from the paracrystalline theory for a stacked lamellar system [11, 24, 48]:

$$S(q) = N + 2\sum_{m=1}^{N-1}(N-m)cos(mqd)\exp\left(-\frac{m^2q^2\sigma_{PC}^2}{2}\right) \tag{6.5}$$

where N is the number of coherently stacked discs d is the distance between two adjacent discs, and σ_{PC} is a measure of the stacking disorder, which accounts for small variations in the discs separation. The size of the coherently stacked disc domains can be therefore evaluated as Nd. Alternatively, the average coherent domain size, D_{Lam}, in the direction perpendicular to the layers formed by D-blocks is related to δ, which is the width of the diffraction peak, as $2\pi/\delta$. The D_{Lam} was found to be close to 1.2 µm, which suggests the formation of the lamella with significant long-range order. The fitting parameters used are thickness of the lamellar layers d_{Lam}= 28 nm, thickness of the D-block layer $d_{D\text{-}block}$= 16.5 nm, and thickness of the P-block layer $d_{P\text{-}block}$= 11.5 nm. The extracted value for λ_d gives us the information that the well-ordered domains with conserved positional and orientational order exist over 314 nm. This means that around 100 helices coherently pack within the lamellar layers.

Due to the LCST behavior of the polymeric block in L-DNA hybrids, their phase behavior is temperature dependent. Scattering profiles of L-DNA hybrids with PNIPAm on both sides at concentration of 119.3 mg ml^{-1} (way below the concentration at which D-block forms LC phases) are shown in figure 6.8. At lower temperatures, similarly to the L-DNA hybrids at higher DNA concentration shown in figure 6.6 a), we can see three lamellar peaks, at the positions q/q^*= 1, 2, and 3. However, the q_{DNA} is considerably broader which indicates a liquid-like positional order of D-blocks within the lamellar layers. By gradually increasing the temperature of the system in the range from 4 to 23°C one can see a minor shift in the position of the lamellar peaks, towards higher q values. The temperature dependence of the lamellar spacing appears due to temperature-responsive nature of PNIPAm. On one hand, as the temperature in the system increases, PNIPAm experiences a slight shrinkage and therefore the lamellar spacing length decreases. On the other hand, the distance between neighboring DNA helices (D-blocks) thereby increases, as can be seen from the temperature dependence of the position of q_{DNA} peak that moves towards lower q values. Upon heating above the temperature of 23°C a drastic change in the scattering pattern can be observed. At 27°C a phase transition to an ordered bicontinuous double gyroid (OBDG) phase, and at 30°C to ordered bicontinuous double diamond (OBDD) phase is observed. Note that this temperature range is still below LCST of PNIPAm. SAXS profiles at temperatures above 23°C are shown in the three upper panels of figure 6.8, together with expected position of peaks for the OBDG and OBDD phase with Ia$\bar{3}$d and Pn$\bar{3}$m space group symmetries, respectively [14, 46, 7, 8]. A great agreement between expected and experimentally obtained

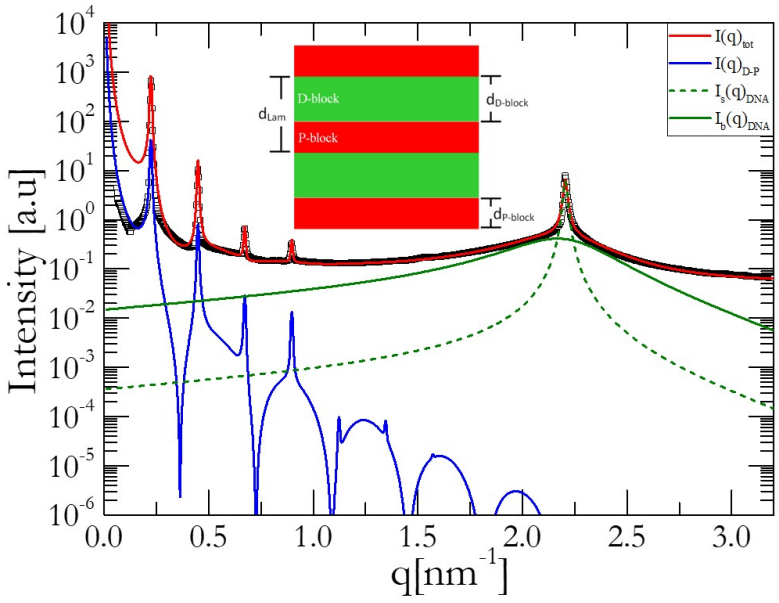

FIGURE 6.7: 1D SAXS profile for L-DNA at concentration of c=163 mg ml^{-1}.The red curve I_{tot} is obtained by fitting the experimental data to a global model, taking into account the scattering intensities arising from ordering of the DNA-polymer hybrids into lamellar structure $I(q)_{D\text{-}P}$ (blue line) and scattering intensities arising from ordering of DNA inside of the domains $I(q)_{DNA}$ (full green line represents $I_b(q)_{DNA}$ accounting for the broader contribution to the q_{DNA} peak, while the dashed green line represents the sharper contribution $I_s(q)_{DNA}$). Fitting parameters are following: d_{Lam}= 28 nm, $d_{D\text{-}block}$= 16.5 nm, and $d_{P\text{-}block}$= 11.5 nm. The proposed packing of L-DNA molecules into lamellar layers is shown in inset, where D-blocks are represented with green color, and P-blocks with red.

peaks is observed which serves as an evidence for the formation of both cubic networks. When observed under crossed polarizers, both phases show no birefringent pattern, also in line with expectations for cubic phases. Finally, at 45°C, which is the temperature above LCST of PNIPAm, characteristic peaks are broadened out and flattened, which indicates a clear transition to a disordered state.

Order to order transitions, appearing in the temperature range between 4 and 30°C, are reversible and stable even if exposed to repetitive and prolonged cooling and heating. All measurements were done on samples after no more than five minutes of equilibration times, which gives away the fact that the kinetics of these phase transitions is rather fast. Therefore, we can say that observed morphologies are in thermodynamical equilibrium and the transition temperatures are well-defined.

The SAXS profiles presented in figure 6.8 manifest the importance of using a polymer with LCST (PNIPAm) to observe the multiple order to order transitions. Above the LCST of PNIPAm the system gets disordered, indicating that utilizing a strictly hydrophobic P-block would not yield such rich self-assembly pathways. Additionally, the LCST of PNIPAm is much lower than the melting temperature of the D-block. Therefore, it is possible to subtly tune the amphiphilicity of the DNA-polymer hybrids without affecting the integrity of the D-block.

Increasing the concentration of L-DNA hybrids above c_{LC}, their temperature dependent phase behavior remarkably changes. To be precise, at 210.3 mg ml^{-1} increasing the temperature from 20 to 25°C the system undergoes a phase transition from lamellar phase to hexagonally packed cylinders (*HPC*) with P6/mm symmetry, as can be seen from the relative peaks positions shown in figure 6.9. At 20°C, the position of primary peak q^* is related to the lamellar spacing length for L-DNA as $d_{Lam}2\pi/q^*$, and is equal to 28.5 nm. At 25°C, the distance between the centers of adjacent cylinders can be calculated as $d_{HPC} = 4\pi/\sqrt{3}q*$ which equals 33.5 nm.

Information about molecular organization within the lamellar phase and *HPC* can be extracted from the 2D scattering pattern of a shear-aligned sample shown in figure 6.10 a) and 6.10 c), respectively. The relative orientation of the arcs related to proposed structures and those corresponding to high q peak is perpendicular. This suggests the transition from *Sm-A* phase (figure 6.10 b)) to *HPC* where D-blocks are packed within cylinders.

More information about the packing of L-DNA within the cylinders in the *HPC* morphology is obtained from the fitting of 1D SAXS profiles at 25°C (shown in figure 6.11. The analysis was performed, as described earlier in this section, according to equations 6.1, 6.2, and 6.3. However, the form factor for the *HPC* morphology is the one for cylindrical structures [13]:

$$P(q) = \int_0^{\pi/2} \frac{2J_1(qR\sin\alpha)}{qR\sin\alpha} \frac{\sin(qL\cos\alpha/2)}{qL\cos\alpha/2} \sin\alpha d\alpha \tag{6.6}$$

with L being length of the cylinder, and R its radius.

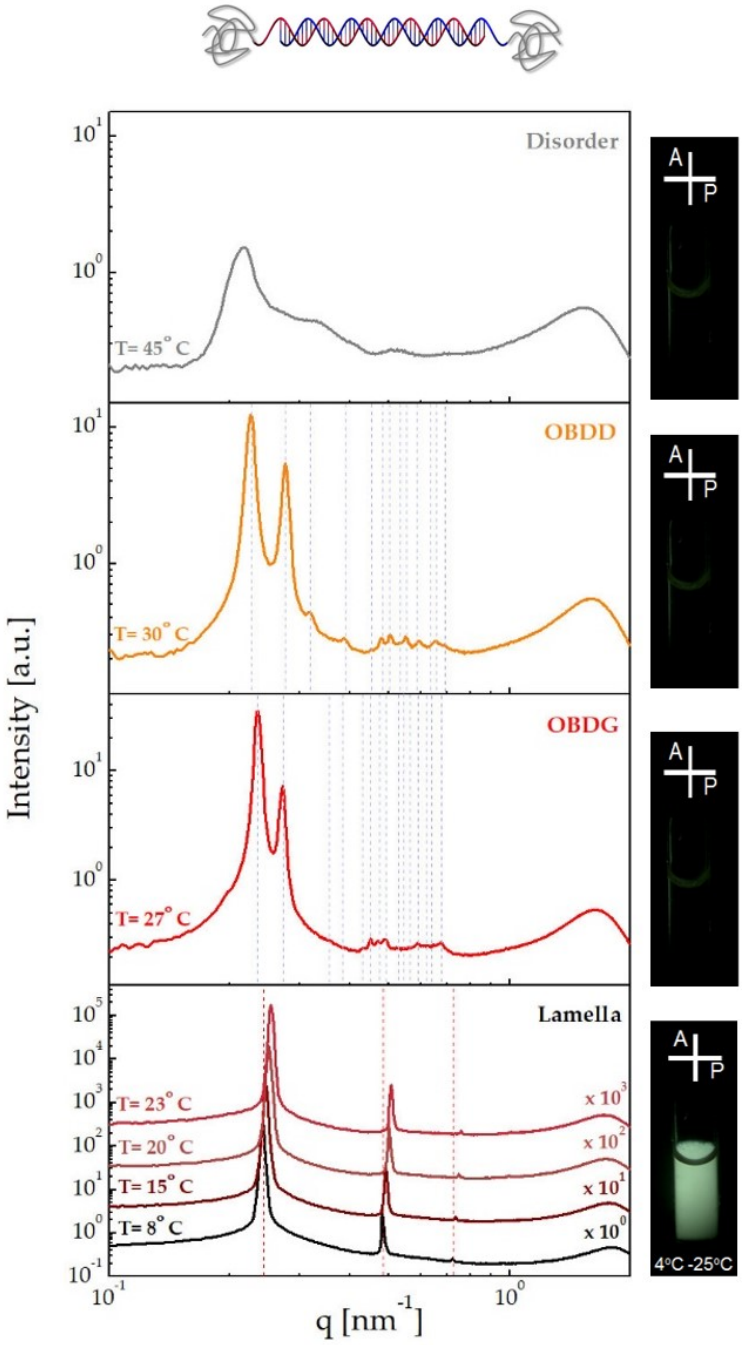

FIGURE 6.8: X-ray scattering profiles of L-DNA at DNA concentration of 119.3 mg ml^{-1} in the temperature range between 8 and 45°C, from bottom to the top. In the lower panel, the scattering profiles are shifted along the intensity axis for clarity. On the right-hand side are shown samples observed under crossed polarizers.

The structure factor for the *HPC* is:

$$\begin{aligned} S(q) &= \frac{c}{qS}\exp(-q^2\sigma_{DW}^2)\sum_{khl}\frac{m_{hkl}}{\sqrt{2\pi}}L_{hkl} \\ &= \frac{c}{qS}\exp(-q^2\sigma^{2_{DW}})\sum_{khl}\frac{m_{hkl}}{\sqrt{2\pi}}\frac{\delta/2\pi}{(q-q_{hkl}^2)-(\delta/2)^2} \end{aligned} \tag{6.7}$$

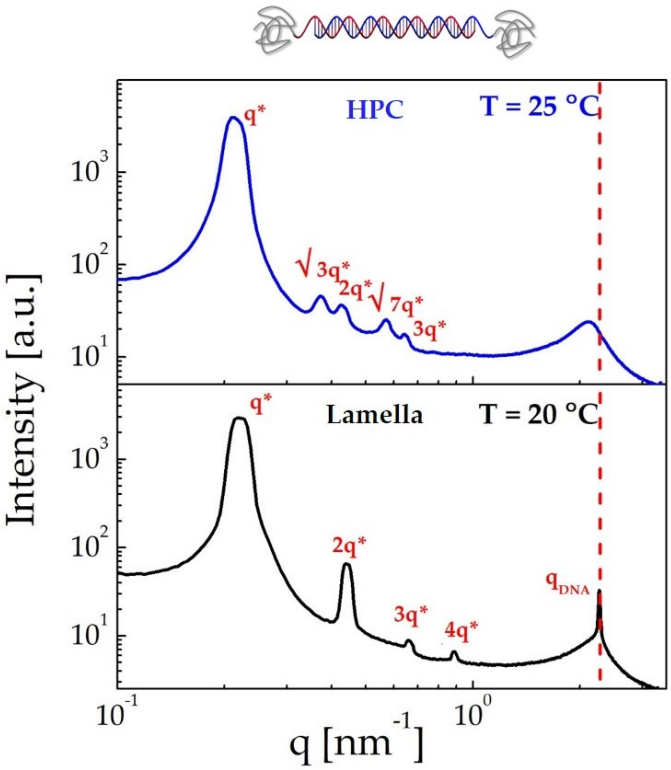

FIGURE 6.9: SAXS profiles of L-DNA at DNA concentration of 210.33 mg ml^{-1} (black curve: T= 20°C, blue curve: T= 25°C).

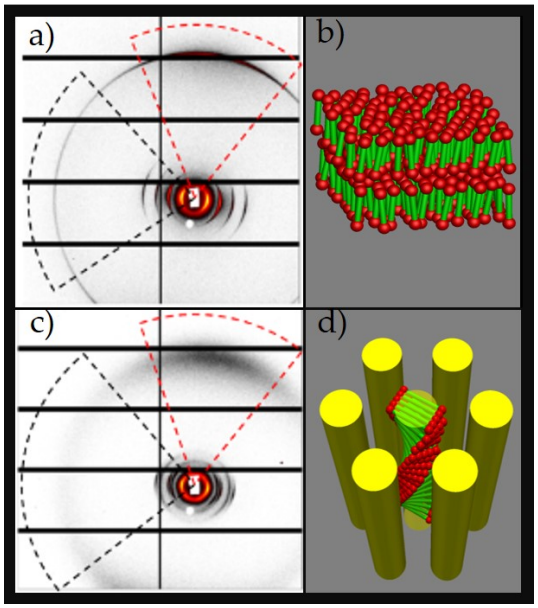

FIGURE 6.10: SAXS patterns of shear-aligned samples at a) T= 20°C, and c) T= 25°C, and schematic representations of b) lamellar (*Sm-A*) phase and d) hexagonally packed cylinders in which the cylinder cross-section contains five L-DNA molecules at most. The D-blocks are represented as green sticks, and P-blocks as red spheres.

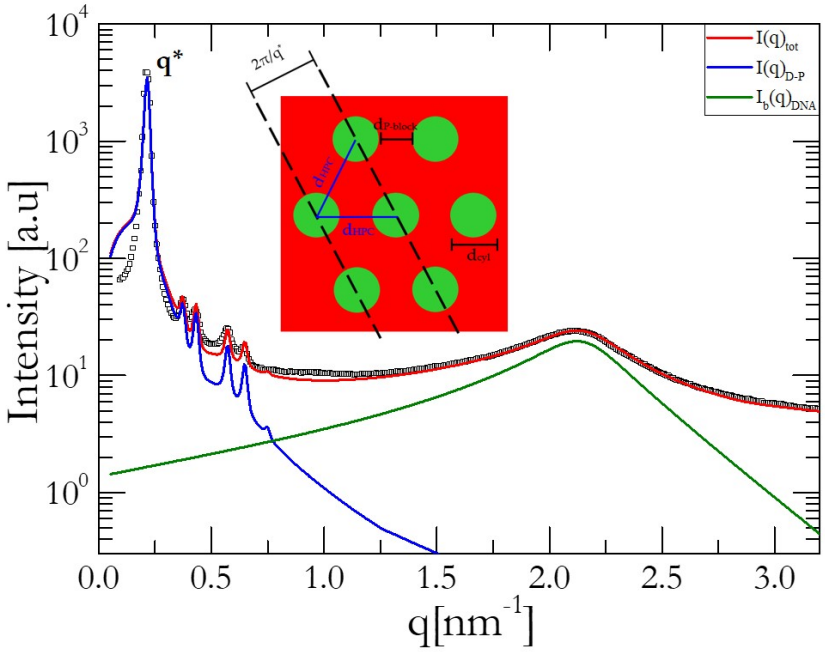

FIGURE 6.11: 1D SAXS profile for L-DNA at concentration of c=210.3 mg ml^{-1} and temperature $T = 25$°C.The red curve I_{tot} is obtained by fitting the experimental data to a global model, taking into account the scattering intensities arising from ordering of the DNA-polymer hybrids into HPC structure $I(q)_{D\text{-}P}$ (blue line) and scattering intensities arising from ordering of DNA inside of the domains $I(q)_{DNA}$ (green line). Fitting parameters are following: d_{HPC}= 33.5 nm, d_{cyl}= 20 nm, and $d_{P\text{-}block}$= 13.5 nm. The proposed packing of L-DNA molecules into HPC is shown in inset, where D-blocks are represented with green color, and P-blocks with red.

S is the surface of the hexagonal unit cell ($S = a^2\sqrt{3}/2$) with lattice constant a, c is a constant, σ_{DW} is the Debye-Waller factor originating from imperfect structural order of the cylindrical domains, m_{hkl} is the peak multiplicity, δ is the peak width of the normalized Lorentzian diffraction peaks L_{hkl}. The Bragg peak position for the cylindrical hexagonal structure (with $l = 0$) is $q_{hkl} = 4\pi\sqrt{h^2 + hk + k^2}/(\sqrt{3}a)$. Finally, the coherent domain size is $D_{HPC} = 2\pi/\delta$.

In order to obtain as good fittings for the cylindrical structure as possible, polydispersity in the cylindrical cross-section was taken into account by considering a Gaussian distribution function for the cylindrical cross-section $D(R)$:

$$F(q, \langle R \rangle) = \int_{R_1}^{R_2} D(R) F(q, R) dR \tag{6.8}$$

The fitting parameters used are distance between centers of two adjacent cylinders in the HPC structure d_{HPC}= 33.5 nm, diameter of cylinders d_{cyl}= 20 nm, and the thickness of the P-blocks $d_{P\text{-}block}$= 13.5 nm (see inset in the figure 6.11).

The extracted d_{cyl} value is slightly larger than molecular length of one D-block ($\sim$ 16.5 nm), which gives a hint about the packing of L-DNA molecules within the

cylinders. Assuming circular cross-section of the cylinders, it is possible that D-blocks induce a twist around a cylinder axis and thereby form chiral nematic cylindrical structure, as shown in figure 6.10 d). A twist of D-blocks within the cylinders could reduce the grafting density of the P-blocks by increasing the distance between neighboring polymeric patches. This way, excluded volume of the system could be additionally reduced, which is related to an increase in conformational polymer entropy. Such packing scenario seems plausible considering the chiral nature of ds-DNA molecules that form N^* phase in concentrated solutions [5]. Additionally, existing Brownian dynamics simulations on model polymer-tethered achiral nanorods have already predicted the formation of such hexagonally ordered chiral cylinders [16]. However, based on the all information available, we still can not exclude the possibility that the cross-section of cylinders in *HPC* structure is not circular but rather rectangular with D-blocks packed in a parallel fashion within a cylinder.

The experimental results were summarized in the form of a phase diagram shown in figure 6.12. The phase diagram shows the temperature-dependent phase sequence of the L-DNA at concentrations below and above the critical concentration c_{LC} at which D-block alone forms LC phases. It is noticeable that changes in the concentration remarkably affect the phase behavior of the L-DNA. At concentrations $c < c_{LC}$ L-DNA exhibits phase transition from lamellar to cubic network morphologies with increasing the temperature. These phase transitions are replaced by the lamellar to HPC phase transition for $c > c_{LC}$.

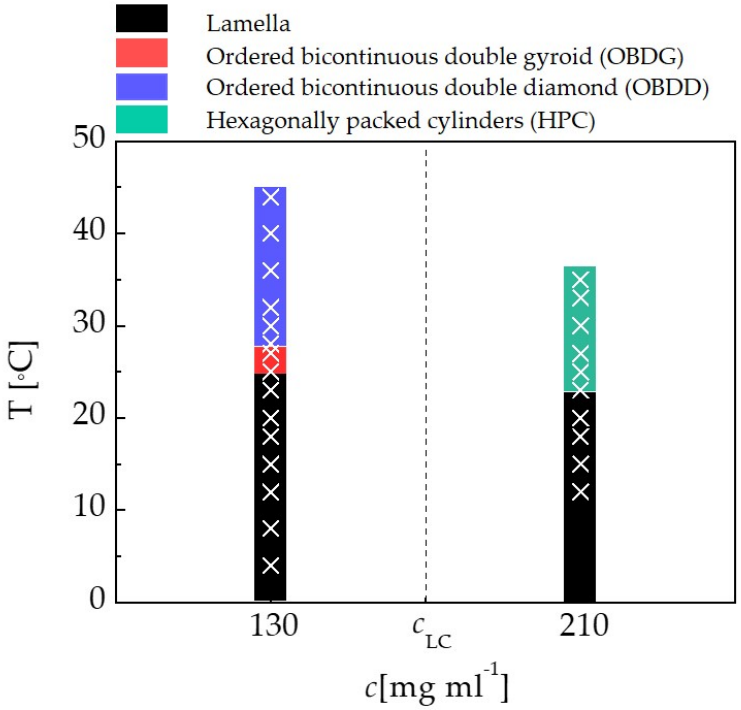

FIGURE 6.12: Indicative phase diagram of L-DNA showing the temperature-dependent phase sequence at DNA concentration below and above the critical concentration for the formation of LC phases in D-block alone ($c_{LC}\sim$ 195 mg ml^{-1}).

6.2.1 Brownian dynamics simulations of L-DNA

In order to gain a deeper insight into packing and molecular arrangement of L-DNA in the cubic networks, we employed Brownian dynamics (BD) simulation. BD simulations were performed in collaboration with Institute of Complex Systems (ICS-2) in Forschungszentrum Jülich.

In simulations, a coarse-grained approach is used to model L-DNA hybrid [19]. D-block is modeled as a chain of N_m beads held together by a harmonic bond potential

$$U_b = \frac{\kappa}{2} \sum_{i=1}^{N_m-1} (\mid r_{i+1} - r_i \mid -l)^2 \tag{6.9}$$

where κ is the spring constant and l is the bond length. The particle rigidity in the chain is controlled by the bending potential

$$U_B = \frac{\kappa_B}{2} \sum_{i=2}^{N_m-1} (r_{i+1} - 2r_i + r_{i-1})^2 \tag{6.10}$$

where κ_B is the bending stiffness. To account for non-bonded interactions, a shifted and truncated Lennard-Jones potential is used

$$U_{LJ} = \begin{cases} 4\epsilon \left[\left(\frac{\sigma}{r}\right)^{12} - \left(\frac{\sigma}{r}\right)^{6} + A \right], & r < r_c \\ 0, & r \geq r_c \end{cases} \tag{6.11}$$

where σ is the diameter of a bead, and ϵ the interaction energy.

Excluded volume interactions between beads are described by $r_c = 2^{1/6}\sigma$, $\epsilon = k_B T$, and $A = 0.25$.

The temperature responsiveness was modeled using attractive potential between the end beads belonging to different DNA-polymer hybrids molecules using equation 6.11, with $A = 2.5^{-6} - 2.5^{-12}$. The end beads modeling polymeric patches are chosen to be larger ($r_c = 2.5\sigma$) then the ones modeling the DNA in order to account for the difference in the range of interaction potential, as can be seen in the scheme shown in inset of the figure 6.13 a). N_m is set to 10, $l = \sigma$, $\kappa = 2000 k_B T/l^2$, and $\kappa_B = 500 k_B T/l^2$. The pair-interaction potentials between the beads are shown in figure 6.13 a). The red line shows the attractive potential between two end-beads, while the blue line represents all other pair-interactions that are purely repulsive and described by hard-core interaction.

Typical simulation run starts with either OBDD or OBDG structure. The unit cell size are values calculated from the primary peak positions of temperature-dependent SAXS profiles in the figure 6.8. The extracted unit cell size for OBDD and OBDG are 39.5 nm and 65.8 nm, respectively. The number density of model L-DNA particles per unit cell is chosen to be compatible with experimental concentrations. Equilibrated structures were analyzed after the potential energy reaches a steady value in time (figure 6.13 b)). According to simulations, if L-DNA hybrids are organized in bundles, the networks are stable at certain concentrations and temperatures.

Initial configurations for BD simulations are two interpenetrating but not intersecting networks formed by mixture of threefold and twofold connectivity of each node in OBDG and fourfold connectivity in OBDD. Nodes are joined together in a series of straight bundles of D-blocks. OBDG structure contains bundles made of

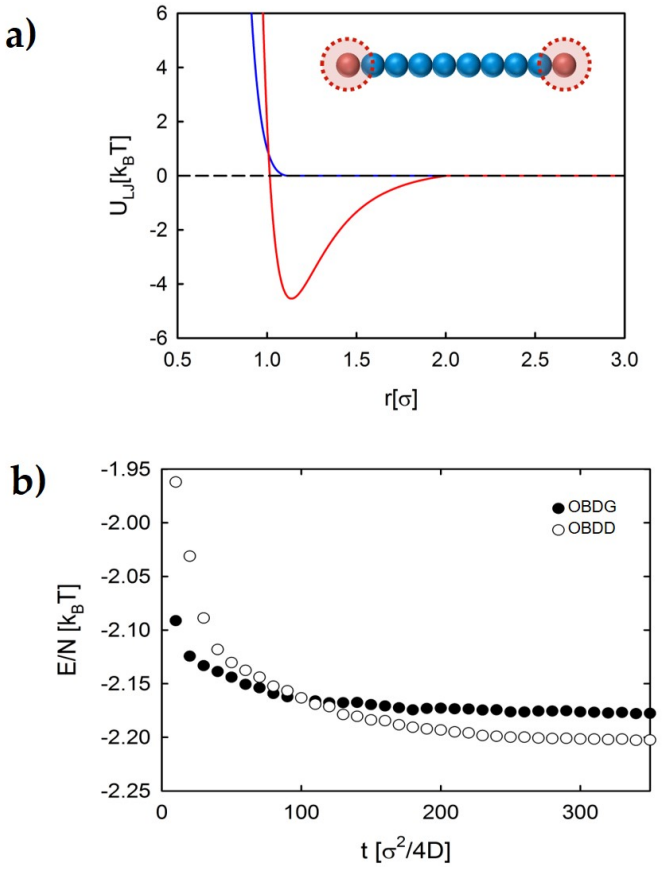

FIGURE 6.13: a) The pair-interaction between non-bonded beads in the model of L-DNA hybrids. Red line represents the attractive potential between red beads located at the ends, while blue line shows all other repulsive interactions. The model of L-DNA hybrids used in the simulations is schematically shown in inset: the hybrids are modelled as a chain of beads in which blue beads represent the D-block while red ones correspond to the P-block. b) Temporal evolution of the potential energy for the OBDG and OBDD structures with ϵ/k_BT=5.

seven D-blocks, while in OBDD there are four. P-blocks are located at the nodes in both cases. Configurations of OBDG and OBDD structures are recorded after the potential energy reaches a steady value and these configurations are presented in figure 6.14. Comparing equilibrium configurations with initial ones indicates that the initial connectivity remains after the equilibrium is achieved.

To assess the stability of the bicontinuous network phases, the temporal evolution of the first eight peaks in the structure factor is examined, which is shown in figure 6.15. The first six peaks for OBDG structure remain visible in equilibrium ($\epsilon/k_BT = 5$), while for OBDD only two first peaks remain. This result suggest that the OBDD structure exhibits more fluctuations and is less stable in comparison with OBDG structure.

Contrary to the simulations, SAXS heating scan experiments reveal that the OBDD network phase is more stable in comparison to the OBDG. As evident from the figure 6.16, the OBDD is present in larger temperature range. Moreover, it appears at higher temperatures as the attraction between polymeric patches are stronger. Due

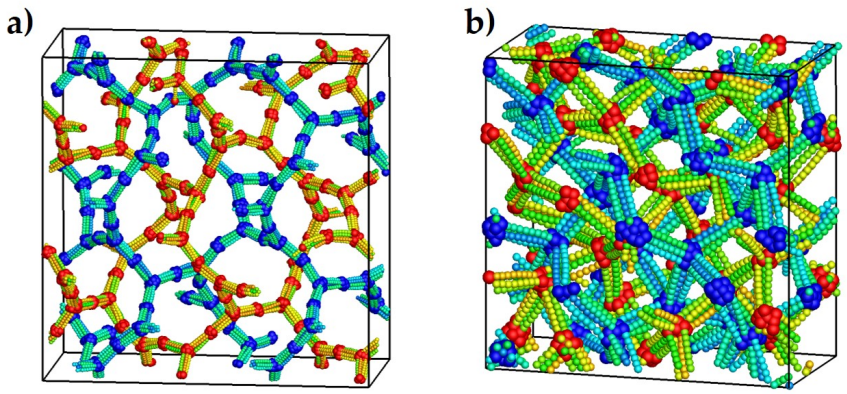

FIGURE 6.14: Snapshots of L-DNA in equilibrium of a) OBDG, and b) OBDD phase, both formed by bundles of DNA-polymer hybrids.

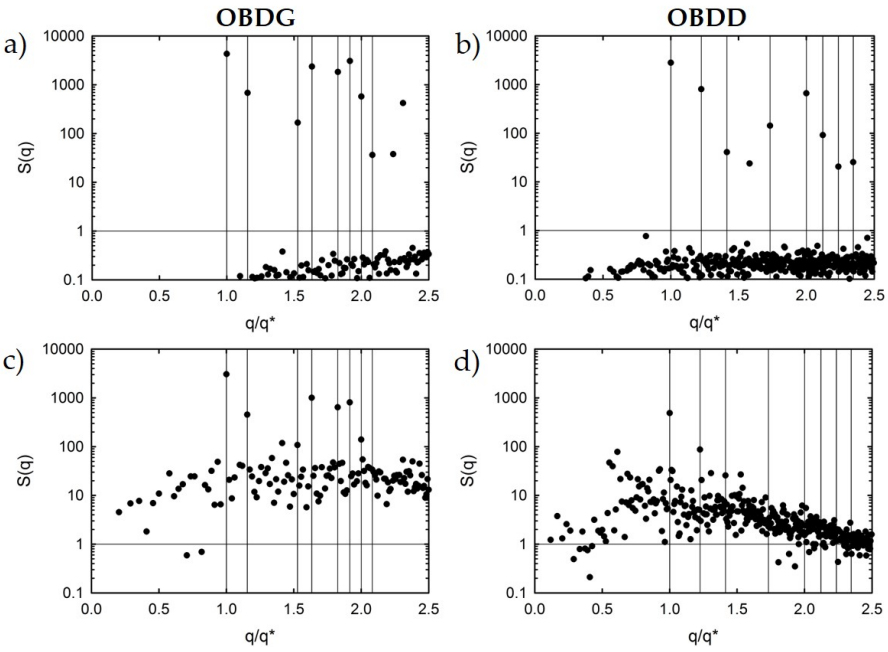

FIGURE 6.15: Simulated structure factors of an initial ordered bicontinuous cubic network with a) OBDG, and b) OBDD morphology. c) Simulated structure factor in equilibrium for OBDG and d) OBDD morphology.

to the simplicity of the simulation model, it is not possible to achieve a quantitative agreement with experiments. BD simulations served entirely as means to probe the molecular arrangement within cubic networks, the formation of which was proven by SAXS experiments.

The stability of structures at different temperatures is checked by modifying the strength of end-attractions. The role of end-to-end attraction strength in L-DNA is shown in figure 6.17. The attraction strength $\epsilon = 6k_BT$ results in well-defined ordered cubic network of OBDG morphology. With lowering the attraction strength the structure gradually disorders.

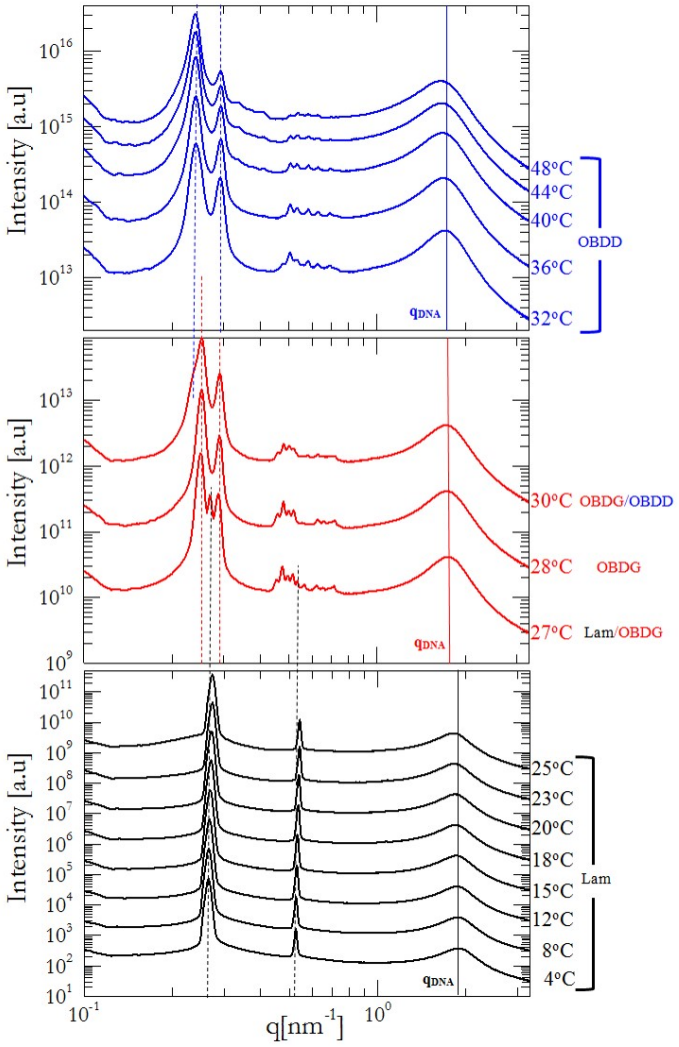

FIGURE 6.16: SAXS heating scan experiment for L-DNA at concentration c= 130 mg ml^{-1}. The experiment is performed in the temperature range between 4 and 48 °C. Different self-assembled morphologies are indicated with different colors. The dashed lines are guide for the temperature dependence of the first two peaks for each phase. The solid line shows the temperature dependence of the q_{DNA} peak.

Alternative molecular arrangements within cubic network phases were considered. It was found that vertically aligned sheets of DNA-polymer hybrids shown in figure 6.18 b) and c) are unstable at concentrations that are comparable to experimental ones. Moreover, they quickly loosen all initial connectivities in the cubic networks, as can be seen in figure 6.18 d) and e). Additionally, OBDG structure with threefold connectivity in each node shown in figure 6.19 a) and c) (initial and equilibrium configuration) was also found to be unstable. This is evident from the simulated structure factors shown in figure 6.19 b) and c) comparing initial and equilibrium morphology. The vertical lines mark the positions of the first eight peaks for OBDG morphology. It can be seen that in the equilibrated configuration, fewer peaks are present. This indicates a partial disordering of the structure.

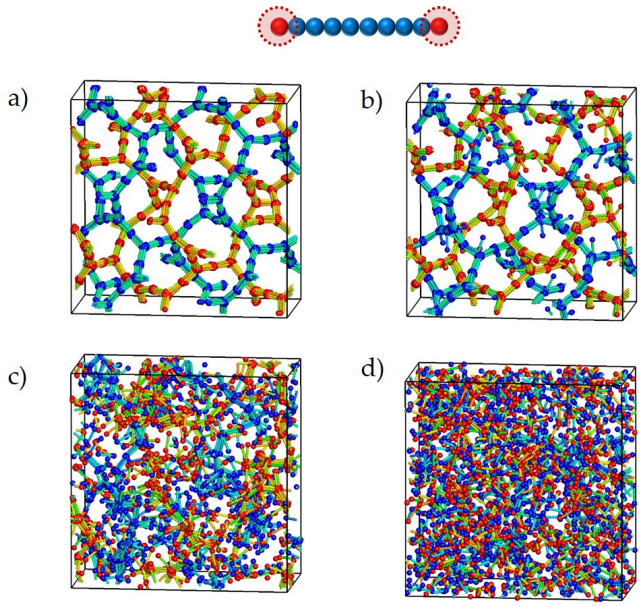

FIGURE 6.17: Snapshots of L-DNA in equilibrium for the OBDG structure with 336 rods per unit cell. The snapshots are shown for different attraction strengths ϵ: a) 6.0 k_BT, b) 4.0 k_BT, c) 3.0 k_BT, and d) 2.0 k_BT.

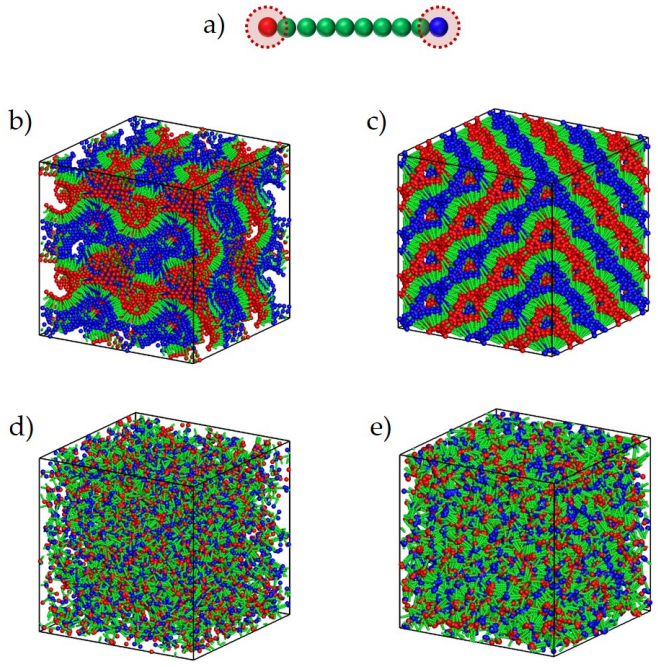

FIGURE 6.18: a) The particle-based model of L-DNA. The beads are shown in different colors to aid distinguishing the individual L-DNA molecules in snapshots. b) Snapshot of the initial L-DNA molecular configurations formed by vertically aligned sheets for an equilibration of an OBDG (811 rods per unit cell) and c) OBDD (1200 rods per unit cell) structure. d) Snapshot of the L-DNA molecular configurations in equilibrium for the OBDG and e) OBDD structure. The end-attraction strength ϵ was set to $3.5k_BT$ for both cubic network phases.

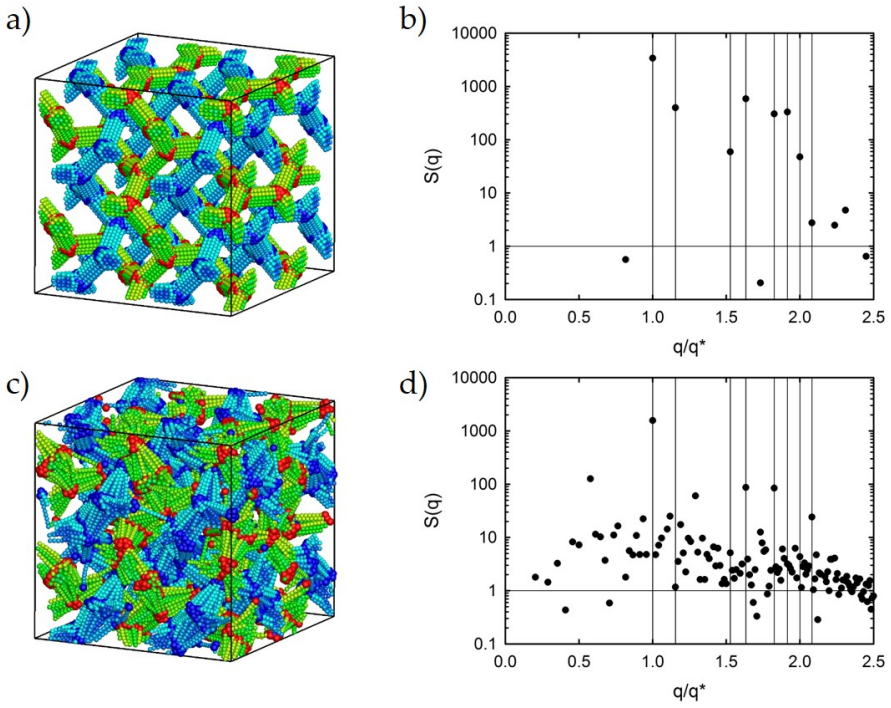

FIGURE 6.19: Brownian dynamics simulation snapshots and simulated structure factors for L-DNA in OBDG structure. OBDG structure is constructed from 456 rods per unit cell and 3-fold connectivity in each node. a) Simulation snapshot for the initial configuration, b) simulated structure factors for the initial configuration, c) simulation snapshot for the equilibrated configuration, and d) simulated structure factors for the equilibrated configuration. The vertical lines in b) and d) mark the first eight peaks positions for OBDG morphology with $Im\bar{3}m$ symmetry.

6.3 Site-specific positioning of P-blocks on the DNA nanorod

Nowadays, automated chemical synthesis of DNA provides easy access to custom-made oligonucleotides with desired sequence. The phosphoramidite synthetic process allows to chemically modify each base of the synthetic DNA. This means that functional groups can be positioned at specific sites on the DNA, with sub-nanometer precision, at a single base level. Therefore, it is possible to site-specifically position the P-block on the DNA nanorods (for more detailed information about the synthesis of DNA-polymer hybrids see section 3.3.3). By placing PNIPAm 10 bp away from the blunt ends of the DNA duplex another type of constructs, Π-DNA hybrids (figure 6.2), were made. These seemingly minor modifications notably affect the phase behavior of the constructs. At approximately the same concentration at which L-DNA exhibits transitions from lamellar phase to cubic network phases with increasing the temperature, Π-DNA hybrids show the transition from lamellar phase to *HPC* (P6/mm symmetry). The SAXS profiles witnessing this transition are shown in figure 6.20. In the temperature range between 6 and 18°C three reflections typical for *HPC* structures are visible, at positions of scattering vector q/q^*= 1, $\sqrt{3}$, and 2. From the position of the principal peak, lattice parameter d_{HPC} can be calculated and it equals to 23.3 nm at 6°C. Upon heating, the lattice shrinks to 21.8 nm at 18°C. At 23°C characteristic peaks broaden out and the system undergoes a phase transition to a disordered state. A weak temperature dependence of the q_{DNA} peak can be observed. The peak moves towards slightly lower q values as the temperature increases.

2D SAXS pattern of shear-aligned sample (figure 6.20 b)) provides more information about the molecular arrangement within the *HPC*. The pattern shows the perfect alignment between arcs originating from *HPC* morphology and those corresponding to the q_{DNA} peak. Therefore, we conclude that long axes of DNA duplexes is parallel to long axis of cylinders into which duplexes are packed as schematically shown in the figure 6.20 c). Note that this molecular arrangement is notably different from the HPC of L-DNA at similar concentration presented earlier in this chapter. In the case of L-DNA, molecules were packed into cylinders with diameter of one molecular length and potentially exhibited a chiral twist at the same time.

The analysis of 1D SAXS profiles provides information about the arrangement of DNA-polymer hybrids within *HPC* (figure 6.21). The cylinder diameter d_{cyl}= 12.4 nm is determined with already described approach, using equations 6.1, 6.2, 6.6, and 6.7. The other fitting parameters are distance between centers of two adjacent cylinders in the HPC structure d_{HPC}= 23.3 nm and the thickness of the P-blocks $d_{P\text{-}block}$= 10.9 nm. Polydispersity in the cylindrical cross-section was also taken into account according to the equation 6.8. The obtained value for d_{cyl} is significantly smaller than the length of one D-block. The thickness of the P-block domain ($d_{P\text{-}block}$= d_{HPC}-d_{cyl}) is found to be similar to the one for *HPC* in figure 6.9 f). Therefore, a packing scenario similar to the one shown in figure 6.9 f) is unrealistic.

Based on information obtained experimentally from 2D SAXS patterns, analysis of 1D SAXS profiles and requirements for maximizing the conformational entropy of the P-blocks, a possible packing scenario of Π-DNA molecules within *HPC* is suggested and shown in figure 6.9 c). Π-DNA molecules are placed within cylinders in a two-dimensional columnar-nematic fashion due to attractive end-to-end stacking interactions acting between blunt ends of D-blocks [30, 21]. Due to these interactions, linear aggregates with long-range orientational and short-range positional order are formed. The LC morphology resulting from such packing scenario resembles hexagonally packed cylindrical polymer brushes.

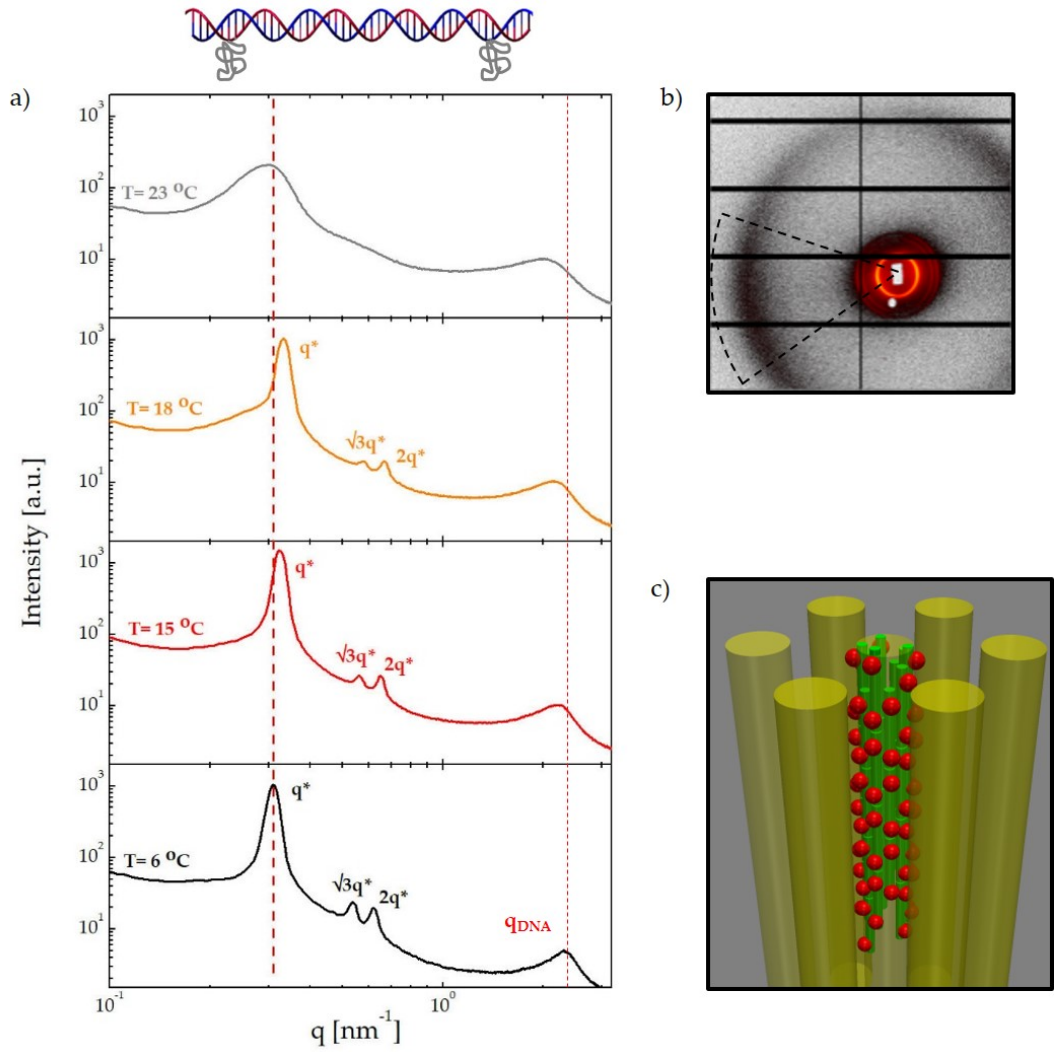

FIGURE 6.20: a) X-ray scattering profiles of Π-DNA hybrid at concentration c = 194.7 mg ml^{-1} and temperatures of T= 6, 15, 18, and 23°C, from bottom to the top. b) 2D SAXS pattern of a shear-aligned sample at T= 4°C. The marked region shows the orientation of arcs corresponding to the typical *HPC* morphology peaks relative to the arc corresponding to q_{DNA} peaks. c) Schematic representation of molecular arrangement within the *HPC* morphology.

Following the same synthetic approach, P-block was attached to another DNA motif. This simple DNA motif is flexible three-arm DNA junction [20] and is commonly used in DNA nanotechnology. Each arm of the junction has length of 13 bp. Attaching P-blocks at the ends of each arm in such structure produces Y-shaped DNA-polymer (Y-DNA) hybrid shown in figure 6.2 c).

Temperature dependent SAXS profiles of these constructs at concentration of 213 mg ml^{-1} are shown in figure 6.22 (with molecular weight of PNIPAm being M_w= 19 kDa). At 4°C the formation of an OBDG phase can be observed, which is witnessed by eight characteristic peaks and the absence of birefringence in the sample [15]. Lattice parameter is calculated to be 56.5 nm. Increasing the temperature, the primary peak shifts slightly to the higher q values. This indicates a slight shrinkage of the unit cell down to approximately 53 nm. Finally, at 23°C the sample disorders.

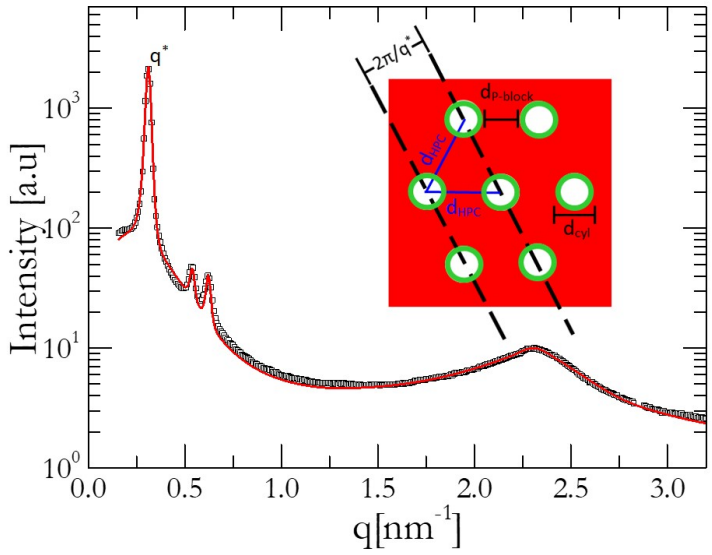

FIGURE 6.21: 1D SAXS profiles for Π-DNA sample at concentration c=194.7 mg ml^{-1} and temperature of 6°C. The red curve is obtained by fitting the experimental data to a polydisperse model. Fitting parameters are following: d_{HPC}= 23.3 nm, d_{cyl}= 12.4 nm, and $d_{P\text{-}block}$= 10.9 nm. The proposed packing of Π-DNA molecules within the cylinders is shown in inset, where D-blocks are represented with green color, P-blocks with red, and solvent with white.

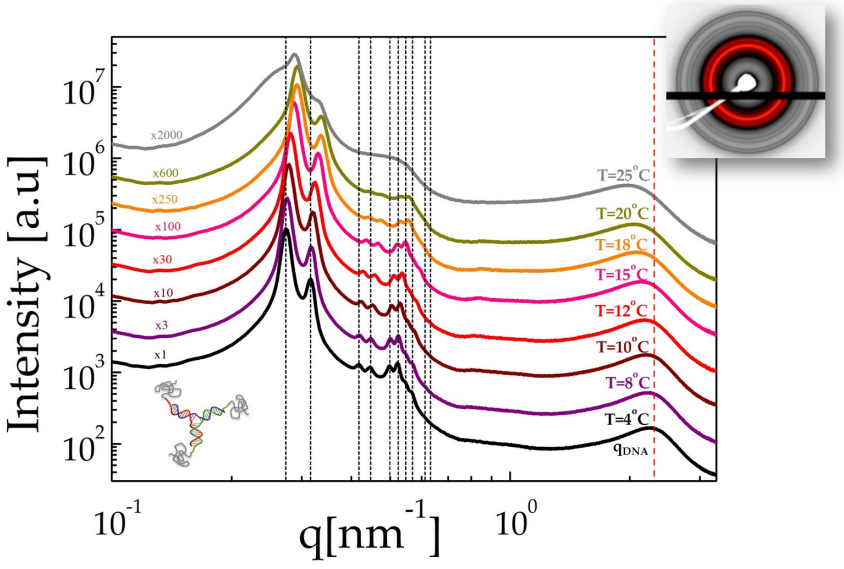

FIGURE 6.22: X-ray scattering profiles of Y-DNA with PNIPAm 19 kDa attached on all three arms at concentration c= 213 mg ml^{-1}, at T= 4, 8, 10, 12, 15, 18, 20, and 25 °C. The expected peaks positions for the OBDG morphology are shown with dashed grey lines. Dashed red line shows the temperature dependence of the q_{DNA} peak. The 2D scattering pattern at 4°C is shown on the top right-hand side.

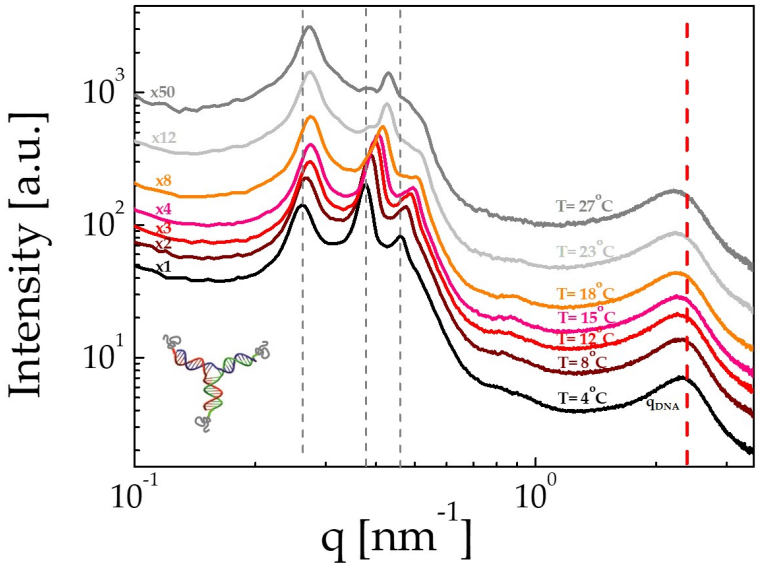

FIGURE 6.23: X-ray scattering profiles of Y-DNA with PNIPAm 1.7 kDa attached on all three arms at concentration c= 288.65 mg ml^{-1}, at T= 4, 8, 12, 15, 18, 23, and 27 °C. The expected peaks positions for the plumber's nightmare morphology are shown with dashed grey lines. Dashed red line shows the temperature dependence of the q_{DNA} peak.

Decreasing the molecular weight of the attached PNIPAm to M_w= 1.7 kDa significantly affects the phase behavior. The SAXS profiles of the sample at concentration of 288 mg ml^{-1} in figure 6.23 in the temperature range between 4 and 12°C show several peaks. Their position relative to the primary peak implies the formation of a cubic network morphology. From the peaks positions and the lack of birefringence in the sample, the cubic lattice with Im$\bar{3}$m symmetry could be assigned to a plumber's nightmare morphology [17, 35], a network with sixfold connectivity. The temperature increase from 4 to 12°C is followed by a slight shift of the peaks positions towards higher q values. This indicates a shrinkage of the unit cell size from 33.6 at 4°C to 32.2 at 12°C. At temperatures above 12°C primary peak remain at the same position. However, higher-order reflections display a gradual decrease in intensity and slight shift towards higher q values. Consequently, the positions of the peak do not fit to the expected peak positions for cubic phase with Im$\bar{3}$m symmetry. This can be attributed to the partial disordering of the sample. It is important to mention that we cannot exclude the possibility that the cubic network morphology could be also another type of cubic lattice, such as body-centered cubic (BCC) or simple cubic lattice. The absence of higher order peaks doesn't allow us to precisely draw conclusions about the type of the cubic phase formed.

6.4 Conclusions

In this chapter we have shown a hierarchical self-assembly concept based on programmable decoration of DNA's backbone with thermo-responsive polymeric patches. There are three key parameters in the proposed self-assembly concept: the stiffness of the D-block, the temperature-responsiveness of the P-block, and the polymeric nature of the latter. These parameters can be easily controlled by changes in the temperature, position of the P-blocks (patches), relative molecular weight of the blocks or geometry of D-block used. The presented approach can be applied to any kind of DNA structure. Even simple DNA architectures decorated with PNIPAm presented in this chapter, yield a variety of complex self-assembled structures. The structures formed range from lamellar to cubic network phases. The ability of DNA-polymer hybrids to form complex self-assembled morphologies is a reminiscent of the surfactant-water and block copolymers systems [36, 29]. However, the field of DNA nanotechnology is able to produce a wide array of complex all-DNA 2D and 3D nanostructures. Therefore, we expect that the programmable decoration of these structures with P-blocks can result in the formation of self-assembled structures with high levels of complexity. The cubic network structures that are easily achieved with the reported approach can potentially open the path to applications in various research fields: photonic crystals [27, 44], plasmonic materials [41], batteries/ion transport [39], and bio-inspired materials with engineered pore structures for synthetic membranes [32].

Bibliography

[1] N. J. Agard, J. A. Prescher, and C. R. Bertozzi. A strain-promoted [3 + 2] azide-alkyne cycloaddition for covalent modification of biomolecules in living systems. *Journal of the American Chemical Society*, 126:15046–15047, 2004.

[2] F. S. Bates and G. H. Fredrickson. Block copolymers-designer soft materials. *Physics Today*, 52:32–38, 1999.

[3] K. M. M. Carneiro, F. A. Aldaye, and H. F. Sleiman. Long-Range Assembly of DNA into Nanofibers and Highly Ordered Networks Using a Block Copolymer Approach. *Journal of the American Chemical Society*, 132:679–685, 2010.

[4] K. M. M. Carneiro, G. D. Hamblin, K. D. Hänni, J. Fakhoury, M. K. Nayak, G. Rizis, C. K. McLaughlin, H. S. Bazzi, and H. F. Sleiman. Stimuli-responsive organization of block copolymers on DNA nanotubes. *Chemical Science*, 3:1980–1986, 2012.

[5] A. G. Cherstvy. DNA cholesteric phases: The role of DNA molecular chirality and DNA-DNA electrostatic interactions. *Journal of Physical Chemistry B*, 112: 12585–12595, 2008.

[6] M. P. Chien, A. M. Rush, M. P. Thompson, and N. C. Gianneschi. Programmable Shape-Shifting Micelles. *Angewandte Chemie - International Edition*, 49:5076–5080, 2010.

[7] C. Y. Chu, W. F. Lin, J. C. Tsai, C. S. Lai, C. S. Lo, H. L. Chen, and H. L. Hashimoto. Order-order transition between equilibrium ordered bicontinuous nanostructures of double diamond and double gyroid in stereoregular block copolymer macromolecules. *Macromolecules*, 45:2471–2477, 2012.

[8] C. Y. Chu, X. Jiang, H. Jinnai, R. Y. Pei, W. F. Lin, J. C. Tsai, and H. L. Chen. Real-space evidence of the equilibrium ordered bicontinuous nanostructures of double diamond and double gyroid in stereoregular block copolymer macromolecules. *Soft Matter*, 11:1871–1876, 2015.

[9] D. Durand, J. Doucet, and F. Livolant. A study of the structure of highly concentrated phases of DNA by X-ray diffraction. *Journal De Physique Ii*, 2:1769–1783, 1992.

[10] S. Förster, A. Timmann, M. Konrad, C. Schellbach, and A. Meyer. Scattering curves of orfdered mesoscopic materials. *Journal of Physical Chemistry B*, 109: 1347–1360, 2005.

[11] A. Guinier. *X-ray diffraction*. W. H. Freeman & Co, San Francisco and London, 1963.

[12] A. Guinier. *X-ray diffraction in crystals, imperfect crystals and amorphous bodies*. Dover, New York, 1994.

[13] A. Guinier and G. Fournet. *Small-angle scattering of x-rays*. John Wiley and sons, New York, 1995.

[14] D. A. Hajduk, P. E. Harper, S. M. Gruner, C. C. Honeker, G. Kim, E. L. Thomas, and L. J. Fetters. The gyroid: A new equilibrium morphology in weakly segregated diblock copolymers. *Macromolecules*, 27:4063–4075, 1994.

[15] D. A. Hajduk, P. E. Harper, S. M. Gruner, C. C. Honeker, E. L. Thomas, and L. J. Fetters. A Reevaluation of Bicontinuous Cubic Phases in Starblock Copolymers. *Macromolecules*, 28:2570–2573, 1995.

[16] M. A. Horsch, Z. Zhang, and S. C. Glotzer. Self-assembly of polymer-tethered nanorods. *Physical Review Letters*, 95(5):1–4, 2005.

[17] D. A. Huse and S. Leibler. Phase behaviour of an ensemble of nonintersecting random fluid films. *Journal de Physique*, 49:605–621, 1988.

[18] J. H. Jeong and T. G. Park. Novel polymer-dna hybrid polymeric micelles composed of hydrophobic poly(d,l-lactic-co-glycolic acid) and hydrophilic oligonucleotides. *Bioconjugate Chemistry*, 12:917–923, 2001.

[19] S. M. Jin, F. Taslimi, R. G. Winkler, and G. Gompper. Self-organized structures of attractive end-functionalized semiflexible polymer suspensions. *Macromolecules*, 47:4118–4125, 2014.

[20] N. R. Kallenbach, R. Ma, and N. C. Seeman. An immobile nucleic acid junction constructed from oligonucleotides. *Nature*, 305:839–831, 1983.

[21] F. Kilchherr, C. Wachauf, B. Pelz, M. Rief, M. Zacharias, and H. Dietz. Single-molecule dissection of stacking forces in DNA. *Science*, 353:1116, 2016.

[22] O. Kratky and G. Porod. Diffuse small-angle scattering of x-rays in colloid systems. *Journal of Colloid Science*, 4:35–70, 1949.

[23] M. Kwak and A. Herrmann. Nucleic acid/organic polymer hybrid materials: Synthesis, superstructures, and applications. *Angewandte Chemie - International Edition*, 49:8574–8587, 2010.

[24] J. Lemmich, K. Mortensen, I. J. Hjort, T. Honger, R. Bauer, and G. O. Mouritsen. Small-angle neutron scattering from multilamellar lipid bilayers: Theory, model, and experiment. *Physical Review E*, 53:5169–5180, 1996.

[25] Z. Li, Y. Zhang, P. Fullhart, and C. A. Mirkin. Reversible and Chemically Programmable Micelle Assembly with DNA Block-Copolymer Amphiphiles. *Nano Letters*, 4:1055–1058, 2004.

[26] F. Livolant and A. Leforestier. Condensed phases of DNA: structures and phase transitions. *Prog. Polym. Sci.*, 21:1115–1164, 1996.

[27] M. Maldovan, A. M. Urbas, N. Yufa, W. C. Carter, and E. L. Thomas. Photonic properties of bicontinuous cubic microphases. *Physical Review B*, 65(April): 165123, 2002.

[28] K. Merchant and R. L. Rill. DNA length and concentration dependencies of anisotropic phase transitions of DNA solutions. *Biophysical Journal*, 73:3154–3163, 1997.

[29] Adam J. Meuler, Marc a. Hillmyer, and Frank S. Bates. Ordered network mesostructures in block polymer materials. *Macromolecules*, 42:7221–7250, 2009.

[30] M. Nakata, G. Zanchetta, B. D. Chapman, C. D. Jones, J. O. Cross, R. Pindak, T Bellini, and N a Clark. End-To-End Stacking and Liquid Crystal Formation of 6- to 20-Base Pair DNA Duplexes. *Science*, 318:1–4, 2007.

[31] P. P. Neelakandan, Z. Pan, M. Hariharan, Y. Zheng, H. Weissman, B. Rybtchinski, and F. D. Lewis. Hydrophobic Self-Assembly of a perylenediimide-linked DNA dumbbell into supramolecular polymers. *Journal of the American Chemical Society*, 132:15808–15813, 2010.

[32] S. P. Nunes. Block copolymer membranes for aqueous solution applications. *Macromolecules*, 49:2905–2916, 2016.

[33] L. Onsager. The effects of shape on the interation of colloidal particles. *Annals New York Academy of Sciences*, 51:627–659, 1949.

[34] P. W. K. Rothemund. Folding DNA to create nanoscale shapes and patterns. *Nature*, 440:297–302, 2006.

[35] U. S. Schwarz and G. Gompper. Systematic approach to bicontinuous cubic phases in ternary amphiphilic systems. *Physical Review E*, 59:5528–5541, 1999.

[36] J. Seddon. Structure of the inverted hexagonal (HII) phase, and non-lamellar phase transitions of lipids. *Biochimica et biophysica acta*, 1031:763–772, 1990.

[37] N. C. Seeman. DNA in a material world. *Nature*, 421:427–431, 2003.

[38] N. C. Seeman. Nanomaterials Based on DNA. *Annual Review of Biochemistry*, 79:65–87, 2010.

[39] C. E. Sing, J. W. Zwanikken, and M. Olvera De La Cruz. Electrostatic control of block copolymer morphology. *Nature Materials*, 13:694–698, 2014.

[40] T. E. Strzelecka and R. L. Rill. Solid-state phosphorus-31 NMR studies of DNA liquid crystalline phases. Isotropic to cholesteric transition. *Journal of the American Chemical Society*, 109:4513–4518, 1987.

[41] S. J. Tan, M. J. Campolongo, D. Luo, and W. Cheng. Building plasmonic nanostructures with DNA. *Nature Nanotechnology*, 6:268–276, 2011.

[42] F. Teixeira, P. Rigler, and C. Vebert-Nardin. Nucleo-copolymers: Oligonucleotide-based amphiphilic diblock copolymers. *Chemical Communications*, 1:1130–1132, 2007.

[43] S. H. Um, J. B. Lee, S. Y. Kwon, Y. Li, and D. Luo. Dendrimer-like DNA-based flourescence nanobarcodes. *Nature Protocols*, 1:995–1000, 2006.

[44] A. M. Urbas, M. Maldovan, P. DeRege, and E. L. Thomas. Bicontinuous cubic block copolymer photonic crystals. *Advanced Materials*, 14:1850–1853, 2002.

[45] J. D. Watson and F. H. Crick. Molecular Structure of Nucleic Acids: A Structure for Deoxyribose Nucleic Acid. *Nature*, 171:737–738, 1953.

[46] K. I. Winey, E. L. Thomas, and L. J. Fetters. The ordered bicontinuous double-diamond morphology in diblock copolymer/homopolymer blends macromolecules. *Macromolecules*, 25:422–428, 1992.

[47] J. Zhang, P. M. Lettinga, J. K.G. Dhont, and E. Stiakakis. Direct visualization of conformation and dense packing of DNA-based soft colloids. *Physical Review Letters*, 113:35–38, 2014. ISSN 10797114. doi: 10.1103/PhysRevLett.113.268303.

[48] R. Zhang, R. M. Suter, and J. F. Nagle. Theory of the structure factor of lipid bilayers. *Physical Review E - Statistical physics, plasmas, fluids, and related interdisciplinary topics*, 50:5047–5060, 1994.

Chapter 7

Conclusions and future directions

The work presented in this thesis is a step forward to a better understanding of DNA self-assembly. In this thesis, the self-assembly of novel all-DNA and DNA-based patchy particles with different architectures was explored. The interdisciplinary character of the conducted research shows the potential to bring together diverse research topics in soft matter: liquid crystals, block copolymers and patchy particles. Overall, the reported results open the path to interesting future research directions.

In chapter 4, blunt-ended gapped DNA duplexes are presented. These all-DNA patchy particles with a chain-stick architecture exhibit the formation of an unconventional smectic A phase. Within the layers, chain-stick DNA duplexes are packed in a folded conformation. This is clearly demonstrated by experiments and simulations. The blunt ends of gapped DNA duplexes act as monovalent attractive patchy sites and are found to be important for the stabilization of the smectic phase. By suppressing the blunt ends attraction, it is shown that the folding is an entropy-driven process. The detailed phase diagram of chain-sticks with different chain lengths is presented. An interesting future direction could be exploring the phase behavior of asymmetric all-DNA chain-sticks. As demonstrated in the thesis, unique physicochemical properties of DNA allow controlling the length and position of the chains and sticks in the gapped DNA duplexes. The asymmetry in the length of the sticks, for example, could reveal interesting packing scenarios.

The self-assembly of all-DNA rod-like patchy particles is investigated in chapter 5. Blunt-ended DNA helices are used as a model system. Selective control over attraction strength between the patches is achieved by engineering of the blunt ends at molecular level. This way, the monolayer and bilayer smectic phase are stabilized. The results offer a direct insight into molecular mechanisms responsible for the formation of smectic phase in linear DNA duplexes. A reasonable step forward could be the re-examination of the liquid crystalline phase diagram of short DNA duplexes of lengths below the persistence length, but with no attractive sites.

Finally, in chapter 6, the self-assembly of DNA-based patchy particles is explored. Temperature-responsive polymer is used as a patchy unit. In contrast to blunt ends, the polymeric patches are not monovalent and their shape and positions are allowed to fluctuate. This powerful hierarchical self-assembly concept, based on programmable decoration of DNA backbone with temperature-responsive polymeric patches, is demonstrated in its minimalistic form. Simple DNA architectures (linear DNA duplexes) decorated with this type of patches yield a variety of complex self-assembled structures, ranging from lamellar to cubic network phases. A major future direction could be using the described self-assembly approach, together with the spatial addressability of DNA in order to guide metallic nanoparticles into specific geometrical arrangements for plasmonic applications.